Interplay between Transport, Magnetism and Structural Properties of Transition Metal Oxides under High Pressure

Inaugural-Dissertation

zur

Erlangung des Doktorgrades
der Mathematisch-Naturwissenschaftlichen Fakultät
der Universität zu Köln

vorgelegt von

Roman G. Lengsdorf

aus Leverkusen-Schlebusch

Köln 2005

Zusammenfassung

Die vorliegende Dissertation beschäftigt sich mit der Untersuchung der elektronischen, magnetischen und strukturellen Eigenschaften von Übergangsmetalloxidverbindungen unter hohen Drücken. Dabei liegt der Schwerpunkt auf dem Einfluß von Ladungsordnung, Spinzustandsübergängen, magnetischer Ordnung und Struktur auf den elektrischen Transport bzw. den Metall-Isolator (MI) Übergang. Anhand ausgewählter Modellsysteme (Selten Erd (R) Nickelate, $RNiO_3$ und Kobaltate $(La,Sr)CoO_3$) sollten die Hochdruckuntersuchungen zu einem tieferen Verständnis der Verknüpfung zwischen den Ordnungsphänomenen und dem Mechanismus des MI Übergangs beitragen.

Als Meßmethoden wurde an allen Verbindungen druckabhängige Messungen des elektrischen Widerstands im Druckbereich bis 25 GPa und bis zu tiefen Temperaturen ($T \leq 4.2$ K) durchgeführt. Ergänzend dazu wurden für einige Verbindungen verschiedene weitere Hochdruckexperimente durchgeführt: Röntgendiffraktometrie, ^{151}Eu nukleare kernresonante Streuung von Synchrotronstrahlung ($EuNiO_3$), Magnetisierungsmessungen ($LuNiO_3$ und $La_{0.82}Sr_{0.18}CoO_3$), Neutronenstreuung ($LuNiO_3$) und K β Röntgen-Emissionsspektroskopie ($La_{0.82}Sr_{0.18}CoO_3$).

Die Besonderheit von $RNiO_3$-Verbindungen mit Perowskit-Struktur ist, daß sie im Gegensatz zu den Manganaten eine sehr kleine Energielücke (≤ 0.1 eV) besitzen, so daß der MI Übergang allein durch Änderung der Temperatur induziert werden kann. Dabei spielt die Größe des R^{3+}-Ions eine entscheidende Rolle für die MI Übergangstemperatur (T_{MI}), welche mit abnehmender Größe der Ionenradius zunimmt ($T_{MI} = 138$ bis 599 K für R = Pr bis Lu), wobei für R = La das System bis zu tiefen Temperaturen metallisch und unmagnetisch ist. Es wurde beobachtet, daß der MI Übergang in $RNiO_3$ (R = Nd bis Lu) mit einem strukturellen Phasenübergang (orthorhombisch–monoklin) bzw. einer Verzerrung verbunden ist, bei der Ladungsordnung auftritt ($2Ni^{3+} \rightarrow Ni^{3+\delta} + Ni^{3-\delta}$). Darüberhinaus zeigen alle Verbindungen bei tiefen Temperaturen ($T = T_N$) eine komplexe antiferromagnetische Ordnung, wobei T_N nicht für alle Verbindungen mit T_{MI} zusammenfällt ($T_N \approx T_{MI}$ für R = Pr, Nd und $T_N \ll T_{MI}$ für R = Sm bis Lu). Die genauen Ursachen für die Verknüpfungen zwischen Struktur, Ladungsordnung und magnetische Ordnung sind bislang noch völlig unverstanden. Vor allem die Frage, inwieweit die Ladungsordnung und die magnetische Ordnung den Mechanismus des MI Übergangs beeinflussen, ist ungeklärt.

Die in der vorliegenden Arbeit durchgeführten temperaturabhängigen elektrischen Widerstandsmessungen $R(p,T)$ unter hohem Druck zeigen, daß in allen untersuchten

RNiO$_3$ (R = Sm, Eu, Y und Lu) Verbindungen ein druckinduzierter Isolator-Metall (IM) Übergang in einem Druckbereich zwischen 5 und 7 GPa auftritt. Daß dieser IM Übergang nicht mit einem strukturellen Phasenübergang (monoklin–orthorhombisch) verbunden ist, belegen Hochdruck-Röntgendiffraktometrieuntersuchungen. Jedoch zeigen neueste druckabhängige Messungen der Gitterparameter in SmNiO$_3$ bei etwa 3 GPa und 300 K eine geringfügige aber abrupte Abnahme des b-Gitterparameters (~ 0.08 %) und gleichzeitige Zunahme des Ni-O-Ni Bindungswinkels, die als Ursache für die beobachtete Abnahme von T_{MI} mit zunehmenden Druck in SmNiO$_3$ angesehen werden kann. In YNiO$_3$ und LuNiO$_3$ findet man keine Anzeichen für eine Gitteranomalie unter Druck. Dadurch stellt sich die Frage: wie tritt der metallische Zustand in der monoklinen Phase auf, in der Ladungsordnung von Ni-Ionen vorherrscht? Die Antwort auf diese Frage liefert eine genaue Untersuchung der druckinduzierten Änderung der Ni1O$_6$ und Ni2O$_6$ Oktaeder in LuNiO$_3$ mittels hochauflösender Neutronen-Diffraktometrie. Hierbei stellt man fest, daß bei einem Druck von 6 GPa die Ni1-O1 Bindungslänge entlang der c-Achse um etwa 2 % abnimmt, während diejenige von Ni2-O1 unverändert bleibt. Die Analyse zeigt, daß sich diese Bindungslängen bei 6 GPa etwa angleichen, wohingegen die Bindungslängen in a, b-Richtung (Ni1-O2, Ni1-O3, Ni2-O2 und Ni2-O3) gleich stark abnehmen. Dies führt zu einem partiellen Schmelzen der Ladungsordnung entlang der c-Richtung, die den IM Übergang unter Druck bewirkt. Dieser Mechanismus könnte auch in den größeren RNiO$_3$ (R = Y $\rightarrow$ Nd), für die ebenfalls Ladungsordnung nachgewiesen wurde, den druckinduzierten IM Übergang verursachen.

Die Druckabhängigkeit der Ordnungstemperatur (T_N) in EuNiO$_3$ wurde durch ^{151}Eu nukleare kernresonante Streuung von Synchrotronstrahlung und in LuNiO$_3$ durch Widerstands- und Magnetisierungsmessungen untersucht. Es zeigt sich dabei, daß in EuNiO$_3$ bei etwa 9 GPa, d.h. im metallischen Zustand, magnetische Ordnung existiert ($T_N \approx 120$ K) und bei etwa 14 GPa verschwindet. Weiterhin findet man bei der Analyse von $R(p, T)$ in dem Druckbereich um 14 GPa ($11.5 < p < 15.9$ GPa) ein Nicht-Fermiflüssigkeitsverhalten ($\Delta R \propto T^{1.6}$) und für $p > 15.9$ GPa ein Fermiflüssigkeitsverhalten ($\Delta R \propto T^2$). In LuNiO$_3$ wurde eine Zunahme von T_N durch Magnetisierungsmessungen bei $p = 1.5$ GPa festgestellt. Ein qualitativer Verlauf von T_N bei hohen Drücken wurde durch das Maximum in $R(p, T)$-Kurven (T_{max}) ermittelt. Demnach sollte ebenfalls der metallische Zustand magnetisch geordnet sein. Schließlich werden (p, T)-Phasendiagramme für EuNiO$_3$ und LuNiO$_3$ vorgeschlagen.

Einen neuen Aspekt bezüglich des Mechanismus des MI Übergangs bietet die Reihe der verzerrten perowskitartigen Verbindungen La$_{1-x}$Sr$_x$CoO$_3$, die sich durch einen zusätzlichen Freiheitsgrad (Co^{3+}-Spinzustand) von den RNiO$_3$-Verbindungen unterscheidet. Im Gegensatz zu herkömmlichen Mott-Isolatoren ist das undotierte isolierende System (LaCoO$_3$, Co^{3+}) im Grundzustand unmagnetisch und im Low-Spin (LS) Zustand ($t_{2g}^6 e_g^0$, $S = 0$). Bei Erhöhung der Temperatur findet man jedoch

bei etwa 100 K einen Übergang zu einem Intermediate-Spin (IS) Zustand ($t_{2g}^5 e_g^1$, S = 1). Mit zunehmender Sr^{2+}-Dotierung ($Co^{3+} \rightarrow Co^{4+}$, Löcherdotierung) geht das System, ausgehend von einer Spinglas-Phase ($0 < x < 0.18$), in einen ferromagnetisch ordnenden Zustand ($x \geq 0.18$) über. Gleichzeitig nimmt die elektrische Leitfähigkeit mit der Dotierung zu und für $x \geq 0.2$ zeigt das System metallische Leitfähigkeit. Es wird angenommen, daß die ferromagnetische Ordnung im metallischen Zustand durch den Doppelaustausch zwischen Co^{4+} (LS) Zustand und Co^{3+} (IS) hervorgerufen wird. Noch ungeklärt ist die Frage nach der Verknüpfung zwischen Spin- und Ladungszuständen in der Nähe des MI-Übergangs, d.h. inwieweit diese Spinzustände den MI-Übergang beeinflussen.

Die Hochdruckuntersuchungen wurden an einer einkristallinen ferromagnetischen Probe $La_{1-x}Sr_xCoO_3$ ($x = 0.18$) in der Nähe des MI-Übergangs durchgeführt. Die temperaturabhängigen Messungen des elektrischen Widerstands unter hohen Drücken zeigen eine dramatische Erhöhung des spezifischen Widerstands um etwa 4 Größenordnungen, was auf eine starke Unterdrückung des Elektronen-Hoppings hinweist. Ferner stellt man mit zunehmendem Druck bei $p = 1.9$ GPa eine Verschiebung von T_{max} (T_C) um etwa 8 K zu tieferen Temperaturen fest. Diese unerwarteten Ergebnisse stehen im Gegensatz zu jenen in anderen Übergangsmetalloxiden, wie z.B. $La_{1-x}Sr_xMnO_3$ oder $La_{1-x}Sr_xFeO_3$. Dort findet man, daß mit steigendem Druck das Elektronen-Hopping zunimmt, was den ferromagnetischen metallischen Zustand stabilisiert und zu einer Zunahme von T_C führt. Die Druckabhängigkeit der Gitterparameter (und des Volumens) zeigen innerhalb der Meßgenauigkeit keinen Hinweis auf einen strukturellen Phasenübergang. Andererseits zeigen strukturelle Untersuchungen an $LaCoO_3$ eine Zunahme des Co-O-Co Bindungswinkels mit zunehmenden Druck, was zu einer deutlichen Erhöhung des Elektronen-Hopping führen würde. Eine strukturelle Änderung kann daher als Ursache für den druckinduzierten isolierenden Zustand in $La_{0.82}Sr_{0.18}CoO_3$ ausgeschlossen werden.

Aufgrund folgender Tatsachen wird ein druckinduzierter Spinübergang von einem magnetischen IS Co^{3+}-Zustand in einen unmagnetischen LS Co^{3+}-Zustand als Ursache für dieses Verhalten angenommen: (a) der Ionenradius von LS Co^{3+} (0.545 Å) ist kleiner als der von HS/IS Co^{3+} (0.61 Å) und (b) die Energie der Kristallfeldaufspaltung Δ_{CF} in $LaCoO_3$ nimmt mit zunehmendem Druck deutlich zu. Eine Vergrößerung von Δ_{CF} führt zu einer Entvölkerung des IS Co^{3+} Zustands und gleichzeitigen Besetzung des LS Co^{3+} Zustands. Daraus folgt, daß das starke e_g Elektronen-Hopping zwischen Co^{3+} und Co^{4+} blockiert wird. Die Konsequenz daraus ist eine Abnahme des Co^{3+} magnetischen Moments (μ_{Co}), was in der Tat auch die Magnetisierungsmessung unter Druck bestätigt. Man findet eine Abnahme von μ_{Co} (bei $T = 5$ K und $B = 2$ T) von etwa 5.4 % bei 1 GPa, was einem Wert von mehr als 30 % bei 5.7 GPa entspricht.

Den mikroskopischen Beweis für einen druckinduzierten Spinübergang liefert die druckabhängige Untersuchung (bis 14 GPa) an $La_{0.82}Sr_{0.18}CoO_3$ mittels inelastischer resonanter Röntgenemission-Spektroskopie an der Co K-Kante: Die Intensität des Satelliten-Peaks, der die Stärke der $3p$-$3d$ Austauschwechselwirkung und somit des

$3d$ magnetischen Momentes widerspiegelt, nimmt mit zunehmendem Druck stetig ab, d.h. es findet ein gradueller druckinduzierter Spinübergang von IS (oder HS) zu einem LS Zustand statt. Das ist ein klarer Beweis dafür, daß der druckinduzierte IM Übergang in $La_{0.82}Sr_{0.18}CoO_3$ von einem Spinübergang getrieben wird.

Contents

Chapter 1

Introduction

One of the long-standing issues associated with strongly correlated $3d$ transition metal oxides (e.g. RMO_3[1]) is the microscopic origin of the metal insulator (MI) transition and the nature of the ground state. This is related to the fact, that in this class of materials the MI transition is driven by strong correlation effects associated with the electron-electron interaction and the interplay between charge, orbital and spin degrees of freedom. The MI transition can be induced by varying the carrier concentration, temperature, magnetic field and internal or external pressure [1]. Thus, studying such an interplay is a fundamental issue for a better understanding of the nature of the MI transition.

In this view, external pressure provides a unique tool to tune electronic and magnetic properties of these systems, by modifying the effective bandwidth (W) of the transition metal by changing the M–O bond length (d_{M-O}) and/or the M–O–M bond angle (θ). In manganese perovskites $R_{1-x}A_x MnO_3$ (A = Ca, Sr, Ba), for example, it has been shown that increasing pressure decreases d_{Mn-O} and increases θ. Both variations lead to an increase of W and thereby stabilize the ferromagnetic metallic state [2, 3, 4].

Another example, which demonstrates the effect of pressure on the charge degree of freedom, is the recent observation in $Sr_{2/3}La_{1/3}FeO_3$ of a pressure-induced transition from the charge ordered antiferromagnetic insulating state to a charge-uniform ferromagnetic metallic state [5].

The aim of this thesis is to investigate the effect of pressure on the transport, magnetic and structural properties of $RNiO_3$ and $(La,Sr)CoO_3$ perovskites, that recently attracted considerable interest due to their unique electronic and magnetic properties.

Unlike manganites, $RNiO_3$ oxides are placed at the boundary separating low-Δ metals (Δ is the charge transfer energy) and the charge transfer insulators. An

---

[1]R = rare earth ion, M = transition metal ion

exciting consequence of this is that the occurrence of the metal insulator transition in $RNiO_3$ series requires neither electron nor hole doping. The MI transition can be induced as a function of temperature and the transition temperature (T_{MI}) increases with decreasing size of the R^{3+} ions (T_{MI} = 130 K (Pr),..., 600 K (Lu)). For R = La the system remains metallic down to lowest temperatures, whereas for R $\neq$ La electron localization occurs. The temperature-induced MI transition in $RNiO_3$ series has been ascribed to the opening of a small charge transfer gap at $T < T_{MI}$ [6, 7] which is intimately connected with a structural phase transition (distortion) from orthorhombic $Pbnm$ to monoclinic $P2_1/n$ [8]. The transition to a monoclinic symmetry upon crossing T_{MI} to the insulating state implies the formation of two different Ni-sites and the presence of a charge ordering ($2Ni^{3+} \rightarrow Ni^{3+\delta} + Ni^{3-\delta}$) [8, 9].

Another interesting aspect of $RNiO_3$ is that for larger R^{3+} ions (R = Pr, Nd) the MI transition is accompanied by an antiferromagnetic (AF) ordering of the Ni sublattice (i.e. $T_N \approx T_{MI}$), whereas for smaller R^{3+} (R = Sm $\rightarrow$ Lu) T_N is much smaller than T_{MI} (e.g. for $EuNiO_3$, T_N = 220 K and T_{MI} = 463 K). According to the magnetic phase diagram $RNiO_3$ exhibit a crossover from antiferromagnetic insulator (R $\neq$ La) to nonmagnetic metal (R = La) through a quantum critical point (QCP) [10]. As external pressure is expected to close the small charge transfer gap in $RNiO_3$, it should result in a pressure-induced insulator to metal (IM) transition. High pressure studies should therefore provide valuable information on the driving mechanism of the MI transition. In particular, the interplay between charge ordering and local structure as well as the crossover from the antiferromagnetic insulating state to the metallic nonmagnetic state.

High pressure experiments have been performed on $RNiO_3$ with R = Sm, Eu, Y and Lu using different experimental techniques (electrical resistivity, x-ray diffraction and complementary magnetization, ^{151}Eu nuclear forward scattering using synchrotron radiation and high resolution neutron diffraction). The results of these measurements are presented and discussed in chapter 4.

The new aspect that distinguishes $(La,Sr)CoO_3$ from $RNiO_3$ and other RMO_3 oxides is that the Co^{3+} ions possess in addition to the usual degrees of freedom an extra degree of freedom, namely the possibility to change the spin-state of Co^{3+}-ions. This can occur if the crystal-field energy Δ_{CF} and the intraatomic exchange energy J_{ex} (Hund's rule coupling) are comparable. Such a delicate balance leads to spin-state transitions which can be induced by changing the temperature or composition [11, 12, 13]. The rhombohedral perovskite $La_{1-x}Sr_xCoO_3$ ($0 \leq x \leq 0.5$) represents an exemplary series in which, contrary to conventional Mott insulators, the ground state of the undoped insulating system ($LaCoO_3$) is nonmagnetic with a low spin (LS, $S = 0$) state which can be thermally excited to either high spin (HS, S = 2) or an intermediate spin (IS, $S = 1$) state at $T \approx 100$ K [14, 15, 16]. At higher

temperatures around 500 K the system undergoes a MI transition. However, by doping with Sr^{3+}, the ground state becomes ferromagnetic for $x \geq 0.18$ (through a spin-glass-like region between $0 < x < 0.18$; at the same time the electrical conductivity increases with increasing x and for $x \simeq 0.2$ the system undergoes a transition to a metallic state [17, 18, 19, 20, 21]. It is generally accepted, that replacing La^{3+} by Sr^{2+} creates formally Co^{4+} ions and the double exchange between Co^{4+} and the remaining Co^{3+} leads to a ferromagnetic coupling [19, 22]. Little is known, however, about the correlation between the spin and charge degree of freedom near the MI transition, i.e. whether and to what extent these spin-state transitions affect the MI transition. To provide an answer to the above given questions, high pressure experiments using different experimental techniques have been performed on single crystal of conducting, ferromagnetic $La_{0.82}Sr_{0.18}CoO_3$ located near the boundary of the MI transition. Electrical resistivity, x-ray diffraction, magnetization and inelastic x-ray emission spectroscopy measurements have been used. The results are presented and discussed in chapter 5. Conclusions of the thesis and an outlook for future work are given in chapter 6.

Chapter 2

Theoretical background

2.1 Electronic states of transition metal ions in crystals

The degeneracy of d levels of a single transition metal (TM) ion ($l = 2$) is fivefold ($2l + 1$). In a crystal, the spherical symmetry of the ion will be reduced due to the strong anisotropic crystal field (CF) and the fivefold orbital degeneracy is lifted. This leads to a splitting of the energy levels and is called the *crystal field splitting* (Δ_{CF}).

Figure 2.1 clarifies why the five d-levels in a crystal with octahedral symmetry become non-degenerate. The crystal field here particularly is determined by the Coulomb repulsion of the oxygen octahedra which surround the TM ions. In the schematic illustration the positions of the oxygen ions (which are called *ligands*) are located on the coordinate axes (x, y, z).

If the orbital of a TM d-electron is adjusted directly towards the oxygen p-orbital (Figure 2.1(a)), it experiences a higher energy due to the Coulomb repulsion than an electron in an orbital which is aligned between the ligand orbitals (Figure 2.1(b)). Thus, the $d_{x^2-y^2}$ and d_{z^2} orbitals which are considered as the e_g-*orbitals* and point directly to the oxygen are higher in energy than electrons of the d_{xy}, d_{yz} and d_{xz} orbitals with lobes between the orbitals of the ligand. They have a small probability density in the p-orbitals and thus are lower in energy. They are considered as the t_{2g}-*orbitals* and as well as the e_g-orbitals degenerated in an octahedral symmetry (Figure 2.1(c)).

This crystal field splitting between the t_{2g} and the e_g levels is often defined as $10Dq$. Typical values for the magnitude of the crystal field splitting are $\Delta_{CF} \sim 1$ - 2 eV.

According to the above discussed Coulomb repulsion of localized electrons, one obtains an additional contribution to the crystal field splitting in the case of hybridiza-
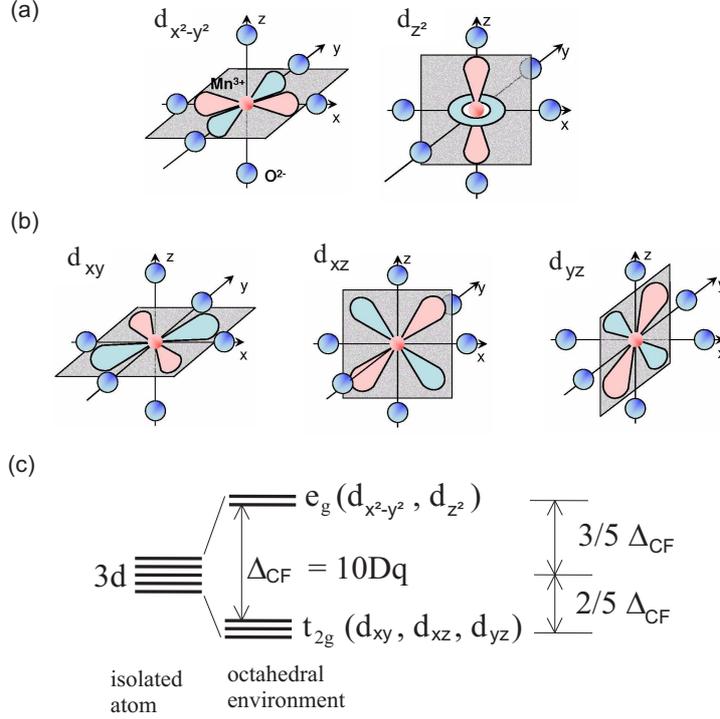
Figure 2.1: (a) The orbitals of the two e_g levels ($d_{x^2-y^2}$ and d_{z^2}) are directed towards the p-orbitals of the ligand, whereas the t_{2g}-orbitals (d_{xy}, d_{yz} and d_{xz}) are directed between the p-orbitals (b). Sign of the wave function: $+$ = red; $-$ = blue. (c) Crystal-field splitting of a fivefold orbitally degenerate $3d$ level of an isolated ion in an octahedral crystal field.

tion between p and d-electrons of the oxygen and the TM ion. Since e_g orbitals have a large overlap with oxygen orbitals, a strong hybridization results which leads to the so-called σ-bonds (Figure 2.2 (a,b)). As a result, such hybridization shifts the e_g levels to higher energy by a contribution of

$$\delta E_{e_g} \sim \frac{t_{pd}^2}{\Delta}, \tag{2.1}$$

where t_{pd} is the hopping matrix element between e_g and p orbitals and Δ is the primarily energy difference between the p- and d-levels. This result can be estimated by second order perturbation theory, assuming the pd-hybridization - which can be described by the hopping matrix element t_{pd} between the e_g- and p-orbital - is small in comparison to the energy difference Δ of the p- and d-states. It should also be mentioned, that the crystal field splitting induced by hybridization (Δ'_{CF}) is always much larger than that induced by the Coulomb repulsion of two adjacent ions ($\Delta'_{CF} > \Delta_{CF}$).
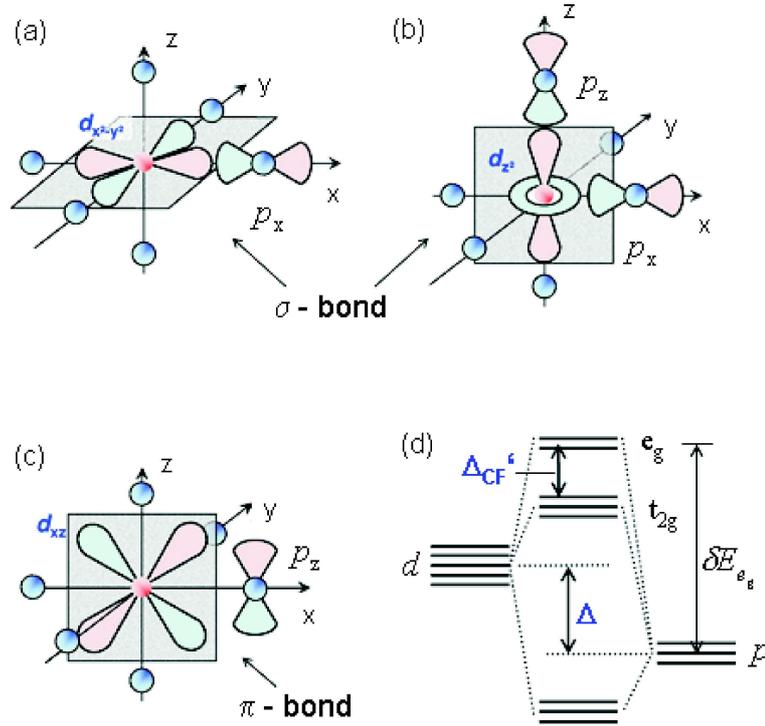
Figure 2.2: The hybridization of d-levels of a TM ion with the p-orbital of a ligand leads to a splitting of the e_g- and t_{2g}-levels. (a,b) strong overlap and hybridization of the $d_{x^2-y^2}$- and d_{z^2}-orbitals with the corresponding p_x- and p_z-orbitals of the oxygen (σ-orbital of the ligand). (c) Overlap and hybridization of the d_{xz}-orbital (one of the t_{2g}-orbitals) with corresponding p_z-orbital of the oxygen (π-hybridization). (d) Scheme of energy levels modified by the hybridization. Note, that $\Delta'_{CF} > \Delta_{CF}$. Sign of wave functions: $+ =$ red; $- =$ blue.

Furthermore, t_{pd} also depends on the TM-O-TM bond angle, which can be described in a first approximation by

$$t_{dd} = \frac{(t_{pd\sigma})^2}{\Delta} \cos \theta, \tag{2.2}$$

where t_{dd} is the electron hopping between two bend d-states in a pervoskite structure across a σ-bonded p-orbital.

It is possible to make these considerations for the t_{2g}-orbitals as well. As shown in Figure 2.1, the t_{2g}-orbitals are orthogonal to the p-orbitals and therefore, the lobes of d-orbitals are orientated to the adjacent TM ion and not to the oxygen. For further discussion, it is important to note the signs of the d wave functions, which are illustrated in different colors in Figure 2.1 and 2.2. These are irrelevant for the Coulomb interaction with the ligands, giving a point-charge contribution to

the CF, but play an important role further on. Because of symmetry reasons, the overlap between the p_σ- and t_{2g}-orbitals disappears - this is clear since the overlap with opposite sign is equal. The remaining overlap is shown in Figure 2.2(c) and known as the π-*hybridization*. Generally, this overlap is allowed by symmetry but it is much weaker than the overlap of e_g-orbitals with oxygen p_σ. Therefore, the energy shift of the t_{2g}-states, due to the $(t_{2g} - p)$-hybridization, is significantly less. In Figure 2.2(d) the modified energy scheme is presented. Clearly to see, that due to the pd-hybridization the t_{2g} set together with the e_g set are shifted to much higher energy and the degenerated p-levels are decreased in energy.

2.2   Ordering phenomena in transition metal oxides

2.2.1   Spin state transition

If we now consider the ground state of a TM ion and distribute all its d-electrons according to Hund's rule, we can put as many electrons with the same spin configuration in the CF-split levels as possible. For d^2 - d^9 systems we furthermore have to take care of the electron-electron interactions; but to simplify matters they should be neglected here exceptionally. In d^1 - d^3 systems, Hund's rule predicts that the electrons will not pair and occupy the whole t_{2g} levels. In comparison to that, in d^4 electron systems for example exist two possibilities: Three electrons can occupy the t_{2g} levels and one the e_g level, so that the electrons do not pair. This situation is called the *high spin* (HS) state. Or all electrons occupy the t_{2g} levels and therefore are partially paired. This is the so-called *low spin* (LS) state. Both cases are illustrated in Figure 2.3.
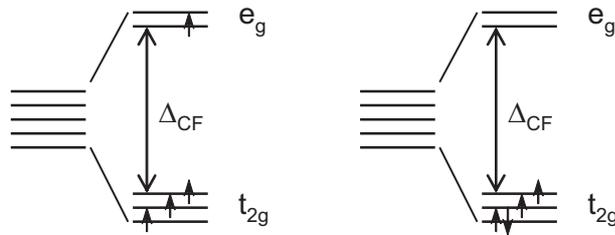
Figure 2.3: Spin states of a d^4 transition metal ion: (a) high-spin (HS) state; (b) low-spin (LS) state

The question of which state will be realized, either HS or LS, is determined by the ratio of Δ_{CF} and the Hund's coupling energy J_H. For both HS and LS states, it is possible to compute the CF coupling energy as a function of number of electrons and strength of the CF.

If for instance $\Delta_{CF} > 3J_H$ (which is shown in Figure 2.3(b)), then a LS state will be favored and the spins will occupy the lowest CF levels at the expense of Hund's rule exchange. In the opposite case the HS state will be favored. In other words, Δ_{CF}/J_H in LS states is larger than Δ_{CF}/J_H in HS states.

Another important fact due to the realization of either HS or LS is, that the ionic radius of TM ions in HS is different than the ionic radius in LS. For example the HS ionic radius of Co^{3+} is 0.61 Å in contrast to 0.545 Å in the LS state [23]. A related situation occurs in Fe^{3+} systems where the HS ionic radius of Fe^{3+} is 0.645 Å in comparison to 0.55 Å in the LS state [23]. This may lead to serious consequences if a system, e.g. $CaFe^{4+}O_3$, which is presented in HS state and external pressure will

be applied. Then pressure leads to a reduction of the volume and the ionic radius, respectively which results in a HS → LS phase transition. This has been observed for pressures $p \geq 30$ GPa [24]. A more extensive discussion about the influence of pressure on the properties of TM ions will be given in chapter 5 and 6.

In the huge field of TM oxides most of them such as e.g. Mn^{3+} (d^4 in $LaMnO_3$) occupy HS state as ground state, comparable to the situation in Figure 2.3(a). Here the large splitting has a crucial consequence: whereas the three electrons in the t_{2g} levels are *localized* to the ion, the single e_g electron can move free through the crystal. It is *itinerant* and provides the metallic conductivity. Furthermore, it carries its spin through the whole crystal and adjusts the spins of the t_{2g} electrons. This also influences the magnetism in $LaMnO_3$.

However, there are notable exceptions in which not HS as ground state is realized. For instance, the ionic states of Co^{3+} (d^6), Ni^{3+} (d^7) and Ru^{4+} (d^4) are often LS states. Also by changing the parameters such as temperature, pressure and composition of the material, different spin states may appear, even real phase transitions as the material crosses over from one state to another may occur. This may be the situation in $LaCoO_3$ [25] for which even a more complicated situation may exist, with the stabilization of an *intermedidate spin* (IS) state [14], see Figure 2.4(b).
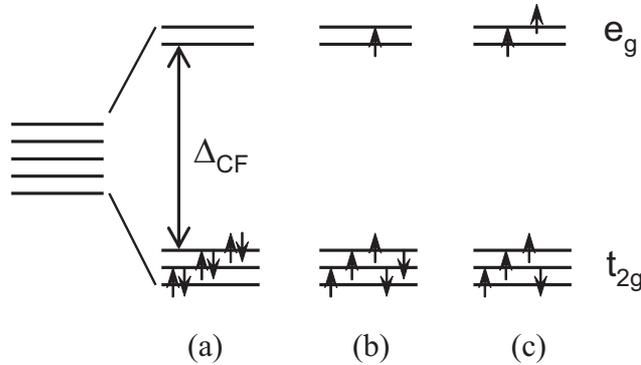
Figure 2.4: Possible electronic configurations of Co^{3+} and Fe^{2+} both with (d^6 configuration): (a) low-spin (LS) state; (b) intermediate spin (IS) state and (c) high-spin (HS) state.

The existence of an IS state is also discussed in doped $LaCoO_3$. The series $La_{1-x}Sr_xCoO_3$ suppresses rapidly the non-magnetic ground state and leads to a ferromagnetic order with increasing Sr-doping, whereas the resistivity decreases and leads to a metallic conductivity [21].

2.2.2 Jahn-Teller effect and orbital ordering

The Jahn-Teller theorem [26, 27] states that a system of interacting electrons and nuclei in a degenerated electronic state is unstable, because the system can always reduce its energy by distorting in such a way as to remove the degeneracy [28]. The linear reduction in energy due to the removal of degeneracy will ultimately be balanced by the initial quadratic increase in elastic energy [29] and a new position of equilibrium will be reached with a permanent distortion of the system. This means that e.g. a regular octahedra may be deformed into a tetragonal distortion to lift the cubic symmetry, see Figure 2.5(a). The energy gain as a function of a distortion α can then be described by perturbation theory as

$$E(\alpha) = -A\alpha + \frac{B\alpha^2}{2} \tag{2.3}$$

Here the first term denotes the splitting of the degenerate levels due to a perturbation whereas the second term denotes an elastic deformation energy. A can be considered as the electron-phonon coupling, B describes the bulk modulus. As a result, one obtains a minimum in energy at some finite α, see Figure 2.5(b).

For the cubic Mn^{3+}-ion in $LaMnO_3$ for instance, a possible distortion consists of an elongation of the oxygen octahedron by the value of 2α in z-direction and a common compression of α in x- and y-direction. The splitting of the energy levels caused by the Jahn-Teller effect (see Figure 2.5(c)) can be understood in a similar way like the crystal field. Elongation in z-direction reduces the Coulomb repulsion between the ligands and the electrons in the d_{z^2}-orbital. This leads to an energy reduction of the d_{z^2}-orbital. In contrast to this, a compression of the octahedron in xy-plane yields to a stronger Coulomb repulsion for an electron in the $d_{x^2-y^2}$-orbital, and results in an increase of energy. This means, that the d_{z^2}-orbital will be energetically lower than the $d_{x^2-y^2}$.

The neighbors of TM ions in perovskites experience the deformation forces and interact with a corresponding deformation since they have common oxygen ligands. This leads to a reduction of the crystal symmetry, i.e. a structural phase transition. This effect is called the *cooperative Jahn-Teller effect* or *orbital ordering*. Orbital ordering means a fixed pattern of orbital occupations at every atomic site in the crystal.

If all the O_6-octahedra are elongated in one direction, one speaks of a ferrodistortion or *ferroorbital ordering*, like in Mn_3O_4 or in Mn ferrites. Even in some cases (e.g. $LaMnO_3$, see Figure 2.6) these orbitals are aligned perpendicular to each other due to the distortion and this leads to a configuration which is known as the *antiferro-orbital ordering*.
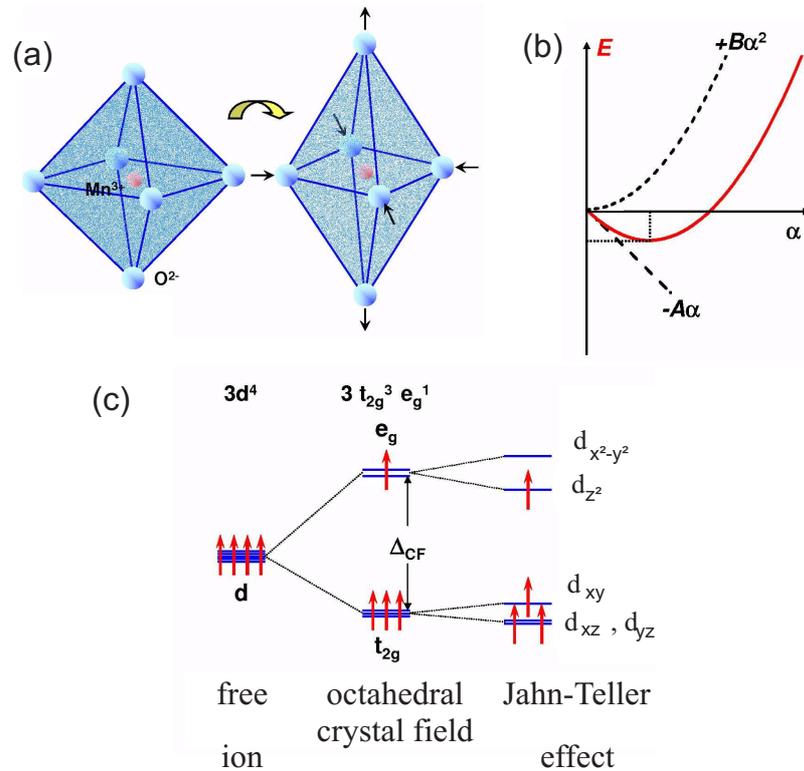
Figure 2.5: Tetragonal deformation of O_6-octahedra stabilizing one particular orbital: (a) Elongation: stabilizing d_{z^2}-orbital (and vice versa a compression: stabilizing $d_{x^2-y^2}$-orbital). (b) A perturbation α reducing the symmetry: a linear term which represents the splitting of the degenerated levels (energy gain) and a quadratic term representing the energy loss. (c) Splitting of the energy levels of the d-orbitals of a Mn^{3+}-ion due to the crystal field and the Jahn-Teller effect. Taken from [30].

Orbital ordering due to the cooperative Jahn-Teller effect occurs in many compounds containing typical Jahn-Teller active ions like Mn^{3+} (d^4), Cr^{2+} (d^4), LS Ni^{3+} (d^7), or Cu^{2+} (d^9). Since the strong hybridization of TM ion and p-orbital of the ligand, the splitting of the e_g-level together with an energetical shift from the adjacent oxygen is rather strong, which gives rise to a strong Jahn-Teller coupling.
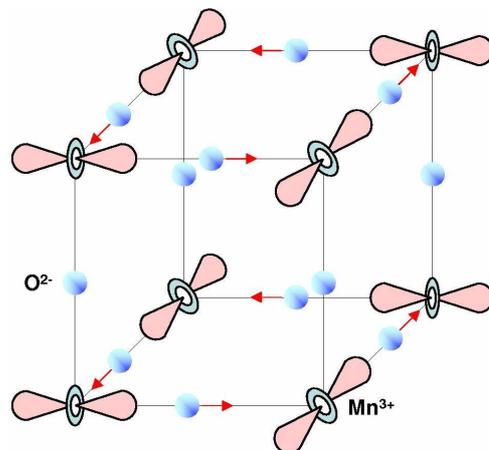
Figure 2.6: Orbital structure and shifts of oxygen ions in LaMnO$_3$: Antiferroorbital ordering with locally elongated octahedra packed so that the long axes alternate in the basal plane. The distortion helps to minimize the total strain of the crystal.

2.2.3   Charge ordering

The phenomenon of *charge ordering* in transition metal oxides is very important with respect to the electric and structural properties of the system. Ions of a particular class of compounds can suddenly change from a homogeneous intermediate valence state to charge disproportionated valence state in which the charge orders in a periodic way. This often leads to a metal-to-insulator transition. The origin of charge ordering is the Coulomb repulsion U between the carriers. If U exceeds a certain value, the charge carriers arrange themselves in a way that they have the largest possible distance from each other. Nevertheless, the electron-lattice interactions can often play a crucial role too, since the charge carriers in an ionic crystal are often accompanied by a distortion of the surrounding ligands. For example, the system $La_{1-x}Sr_xFeO_3$ with $x \approx 2/3$ shows below 210 K a disproportionation of the Fe^{4+} valence into $2Fe^{4+} \rightarrow Fe^{3+} + Fe^{5+}$ and an antiferromagnetic spin or-
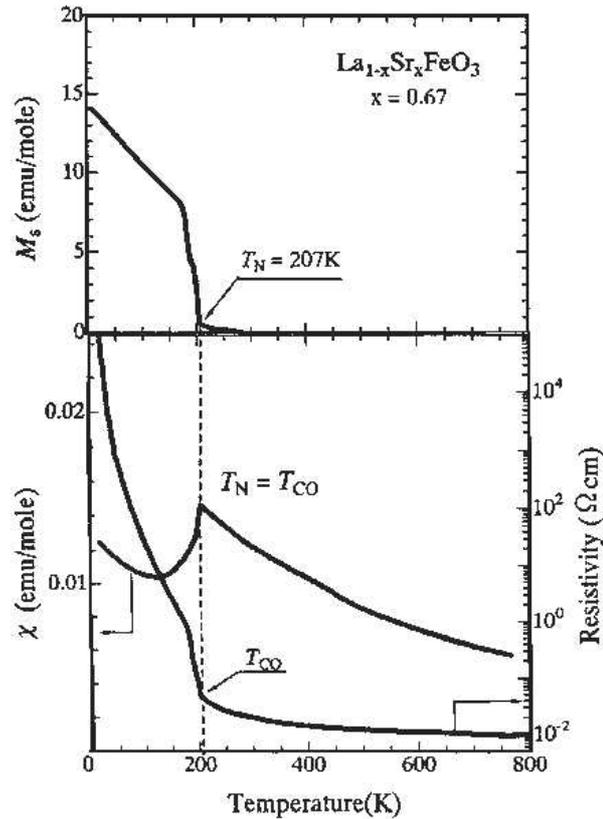
Figure 2.7: Spontaneous magnetization (M_S), electric resistivity (ρ) and magnetic susceptibility (χ) for $La_{0.33}Sr_{0.67}FeO_3$ as a function of temperature [34].

dering [31, 32, 33]. Whereas $LaFeO_3$ is an antiferromagnetic insulator ($3d^5$, S = 5/2, T_N = 738 K), on the other end $SrFeO_3$ is an antiferromagnetic metal with T_N = 134 K [34]. Figure 2.7 shows that below T_N the electric resistivity ρ of $La_{1-x}Sr_xFeO_3$ increases dramatically about more than 6 orders in magnitude, indicating the appearance of a first-order phase transition. This is the charge-ordering (CO) phase transition with simultaneous antiferromagnetic spin ordering and was first observed in this compound by Mössbauer spectroscopy [31] and confirmed by neutron-scattering measurements [33]. This electronic phase transition proved to be the simultaneous charge and spin ordering in a superlattice structure is presented in Figure 2.8. Here, the disproportionated charges are condensed within the (1 1 1) plane in the cubic perovskite structure.
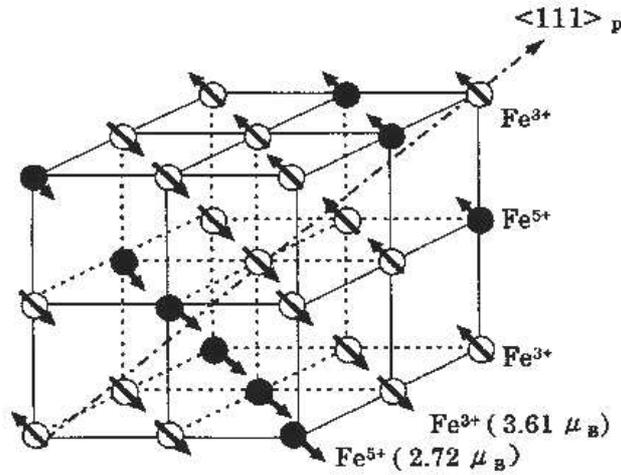
Figure 2.8: Schematic structure of the charge- and spin-ordered state with charge disproportionation in $La_{1-x}Sr_xFeO_3$ with $x \approx 0.67$

2.3   Exchange interactions in magnetic oxides

Up to now we mainly have considered the electronic properties of isolated TM ions in crystals (charge, spin, orbital ordering and Jahn-Teller effect) with their properties arising from an interaction between the ions. The magnetic interactions in such systems are of special interest, since they cause long-range magnetic ordering as well as the possibility of electron transfer from one site to another [35]. The easiest model describing the interplay between localization and band formation in a solid is the one-band Hubbard model [36].

2.3.1   The Hubbard model

According to the discussion of electronic structure of doped manganites in the previous section, we have neglected the spin interactions. But these interactions are of fundamental importance since they are responsible for magnetic ordering states which are observed in experiments. Now we will also include these relevant magnetic interactions in doped manganites into discussion. These considerations can also be used for the most other TM oxides. The magnetic dipole-dipole interaction between spins of adjacent Mn-ions generally is rather weak and plays no role. In contrast to this, exchange processes are of fundamental importance due to the realization of a long-range ordered magnetic ground-state. In such processes electrons (and with them their spins) have a certain probability to hop to their next neighbor's site and reduce the energy of the system hereby. This hopping of electrons is important for the magnetic interactions as well as for the electric transport.

Finally, we are looking for a highly oversimplified model for electrons in a solid which interact with each other through extremely short-ranged repulsive (Coulomb) interaction [37, 38]. Origin of the discussion should be a lattice, where a single electron with spin $S = 1/2$ (either with $\uparrow$ or $\downarrow$) sits on each lattice site and has exactly one level of disposal. That electron could be for example the e_g-electron of LaMnO$_3$. This scenario can be well described by the Hubbard model:

$$H = H_t + H_U \tag{2.4}$$

The first term of the Hamiltonian expresses the quantum mechanical hopping of electrons in a conduction band of width W, thus the kinetic energy.

$$H_t = -t \sum_{\langle ij \rangle, \sigma} (c_{i\sigma}^\dagger c_{j\sigma} + c_{j\sigma}^\dagger c_{i\sigma}). \tag{2.5}$$

The operators $c_{i\sigma}^\dagger$ and $c_{j\sigma}$ are standard fermionic creation and annihilation operators for an electron with spin σ (σ either $\uparrow$ or $\downarrow$) at site i and j, respectively. The matrix element t_{ij} determines the nature of this hopping. In most cases only hopping between adjacent neighbors $\langle i, j \rangle$ with a hopping amplitude $-t$ is considered. The amplitude of the hopping is negative in order to emphasize the gain in kinetic energy

of the system due to the hopping. The second term considers the local Coulomb interaction U between the electrons.

$$H_U = U \sum_i n_{i\uparrow} n_{i\downarrow} \tag{2.6}$$

The operator $n_{i\sigma}$ counts the electrons with spin σ at site i. For $U \ll t$ the Hamiltonian describes a metallic state

$$H_t = \sum \varepsilon_k c_{i\sigma}^\dagger c_{j\sigma} \text{ with } \varepsilon_k = -2t(\cos k_x + \cos k_y + \cos k_z). \tag{2.7}$$

Hereby we assume the simplest tight-binding approximation for the band dispersion with hopping only between next neighbors in a simple cubic lattice.

In the case of $U \gg t$, the contribution of H_U governs in the Hubbard model. An electron which hops to its neighbor site of course gains some energy t, but it has to overbear the much larger energy U. Thus, the energetically most favorable state is that without manifold occupation, i.e. single occupied. This is a localized state and describes the Mott-Hubbard insulator which will be discussed later.
Since H_U alone contains no linkages of different lattice sites, the energy of that with H_U linked state does not depend on the orientation of the surrounding other spins. As a result, a magnetically ordered state can not be realized with H_U alone. But this will change soon, if hopping between the sites is allowed. The electrons can now gain kinetic energy ($\langle H_t \rangle < 0$), but have to bring up the potential energy ($\langle H_U \rangle$). These excited states can now be added to the ground state, so that a reduction of the energy may occur. (This formally conforms a covalent bonding.) The energy gain can be determined in second order perturbation theory ($t/U \ll 1$) and is of order t^2/U [39].

Additionally a tendency of antiferromagnetic spin ordering occurs, which can be easily understood by the following consideration: If two electrons on adjacent lattice sites have the same spin, hopping is forbidden due to Pauli's exclusion principle. Do they have opposite spins, hopping is allowed. This is schematically demonstrated in Figure 2.9 with two d_{z^2}-orbitals. One electron hops to its neighbor and back with matrix element t. According to second order perturbation theory this results in an energy gain of $\Delta E = -2t^2/U$. The contribution H_t in equation (2.4) comes twice, from where the t^2 in the counter results from. In the denominator the energy of the virtual intermediate state is written and the factor of 2 comes from the fact that the left spin can hop to the right and the right to the left. As a result a configuration with antiparallel spins is preferred relative to the one with the parallel spins and thus an antiferromagnetic ground state. This can be described as an effective exchange interaction:

$$H_{ex} = J_{ex} \sum (S_i S_j) \qquad \text{with} \quad J_{ex} = \frac{4t^2}{U}. \tag{2.8}$$
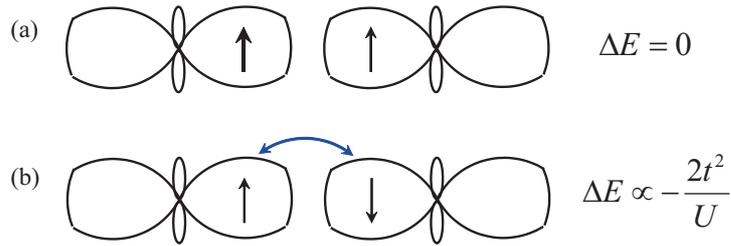
Figure 2.9: Two neighboring d_{z^2} orbital with (a) parallel and (b) antiparallel spin. The energy gain due to the virtual hopping of an electron to a neighboring site is shown.

In other words, the virtual hopping of electrons leads to an *antiferromagnetic Heisenberg exchange interaction* which is usually known as the *kinetic exchange* or *superexchange*[1] (see section 2.6). Thus, Pauli's principle obviously has a significant fraction of the antiferromagnetic correlations of the electrons in the lattice, since two electrons may not occupy the same level.

---

[1]Strictly speaking, this expression stands for an analog interaction of magnetic ions via a diamagnetic ion.

2.4 Charge-transfer and Mott-Hubbard insulators

In our discussion up to now, we have assumed that the electron hopping from one site to another is straightforward. But this is not the case in real TM oxides like $LaMnO_3$. The hopping between the Mn-sites occurs via the intermediate oxygen ion. But in many cases this detail is not very important. Thus, we can say that neighboring ions (e.g. Mn^{3+}) still interact, if one electron in an orbital at a particular lattice position has a certain probability density in the orbital of its neighbor - whatever hopping is directly from orbital to orbital or via intermediate orbitals. This is the main essence of the above introduced hopping between lattice points with the transfer integral J_{ex} in (2.8). If the orbitals do not overlap, t is equal zero. Therefore, the hopping t finally is an indicator for the degree of hybridization between two adjacent orbitals. Obviously, it is sufficient to consider only the outer ionic orbitals, i.e. the $3d$ orbital of the TM ion and the $2p$ orbital of the oxygen ligand, since the overlap to energetically lower orbitals is clearly less.

However, if we take the d-electrons of the TM ion as well as the p-electrons of the oxygen into account, the Hamiltonian can be described in the following form:

$$H = \sum \varepsilon_d d_{i\sigma}^\dagger d_{i\sigma} + \varepsilon_p p_{j\sigma}^\dagger p_{j\sigma} + t_{pd}(d_{i\sigma}^\dagger p_{j\sigma} + \text{h.c.}) + U n_{di\uparrow} n_{di\downarrow}. \qquad (2.9)$$

Here the operators $d_i^\dagger$ and d_i as well as $p_i^\dagger$ and p_i are the creation and annihilation operators for an electron at the TM ion site and the oxygen site, respectively. ε_p and ε_d are the energies of the $2p$- and $3d$-states, whereas t_{pd} describes the hopping between the p- and d-orbitals. Responsible for the hopping between $3d$-orbitals via the oxygen $2p$-orbitals is the energy difference between the $2p$-orbitals to the $3d$'s. This energy gap $\Delta := \varepsilon_d - \varepsilon_p$ is known as the *charge-transfer energy*.

Now it is possible to distinguish two cases, depending on the charge-transfer excitation energy Δ and the Coulomb repulsion U. This situation is schematically shown in Figure 2.10.

(i) $\Delta/U \gg 1$, the Mott-Hubbard insulator:

If the oxygen $2p$-orbitals are low in energy (Figure 2.10 (a)), Δ will be much larger than U, then the lowest charged excited states are those which correspond to the transfer of a d-electron from one TM site to another: $d^n + d^n \rightarrow d^{n-1} + d^{n+1}$. This process costs the energy U. As we have seen above, we obtain an insulating ground state for $U \gg W$ (W denotes the bandwidth), which is known as a *Mott-Hubbard insulator*. Certainly, this hopping does not happen directly from one TM ion to the next, but via the oxygen p-states. With some support of perturbation calculations it is possible to introduce an effective $d - d$ hopping matrix element

$$t \equiv t_{dd} = \frac{t_{pd}^2}{\Delta}, \qquad (2.10)$$

(a) Mott-Hubbard insulator: (b) Charge-transfer insulator:
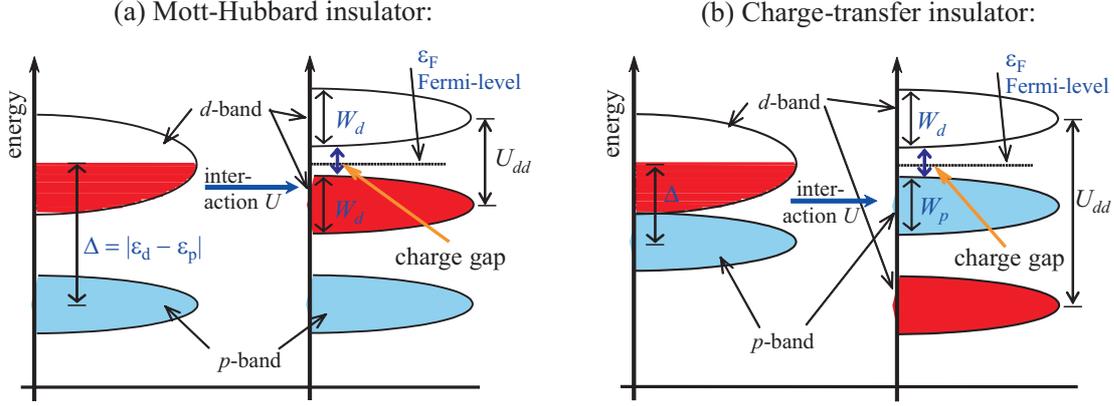
Figure 2.10: Schematic view of a Mott-Hubbard insulator and charge-transfer insulator, reproduced from [1]. In the case of ignored hybridization between p- and d-bands and multiple effects, the magnitude of the energy gap E_g in Mott-Hubbard insulators can be written as $E_g = U_{dd} - W_d = U - 2zt = U - \Delta$ and for charge-transfer insulators as $E_g = \Delta - \frac{W_p + W_d}{2}$, where W_p and W_d is the bandwidth of the p- and d-band, respectively and z denotes the coordination number of the ligand.

which can be taken into account of the simple Hamiltionian (2.5).

(ii) $\Delta/U \ll 1$, the charge-transfer insulator:

If on the other hand the $2p$-orbitals are close to the $3d$-levels (Figure 2.10(b)), Δ becomes much smaller than U and the lowest charged excited states are those where an electron of a $2p$-level will be transferred into a $3d$-level of an adjacent TM ion. Therefore results in a *hole* at the oxygen site. For one electron per TM ion and $\Delta/t \gg 1$, we obtain again an insulating ground state, which is defined as *charge-transfer insulator*. In the simplest case, such a state will be antiferromagnetic, with the only difference being in the exchange integral J_{ex} (2.8) which will be expressed now as

$$J_{ex} = \frac{2(t_{pd}^2/\Delta)^2}{2\Delta + U_{pp}} = \frac{2t^2}{2\Delta + U_{pp}}. \tag{2.11}$$

Here, it is necessary to take the effective hopping matrix element t from eq. (2.10) and the energy $(2\Delta + U_{pp})$ of the virtual intermediate state, whereas U_{pp} describes the Coulomb repulsion of two holes at the oxygen lattice site.

Thus, from the point of view of magnetic properties, there is no significant difference between charge-transfer insulators and Mott-Hubbard insulators. However, differences appear in their excitation spectra as well as in their transport properties. Further effects are discussed in detail in [40, 41] and used for the description of some

real materials, e.g. CrO_2 in [42].

According to this two limiting cases, *Zaanen, Sawatzky and Allen* [43] suggested the following phase diagram:
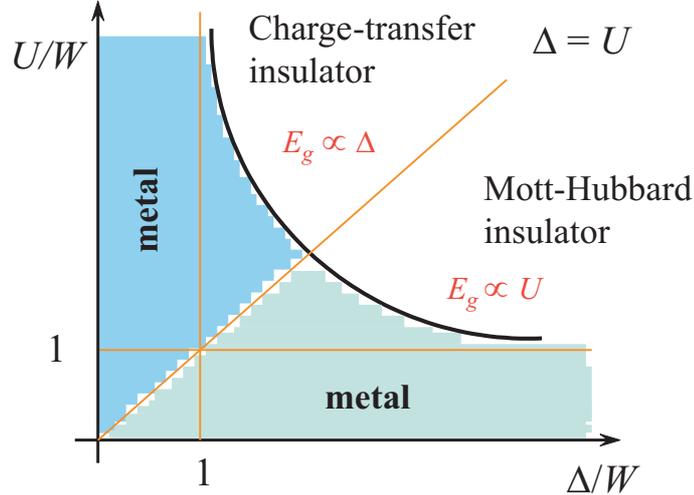
Figure 2.11: General Zaanen-Sawatzky-Allen phase diagram which separates Mott-Hubbard insulators from charge-transfer insulators.

For $U/W > \Delta/W$ the band gap is of $p-d$ type and the anion or ligand p-band is located between the lower and upper Hubbard bands. This gap is a charge-transfer gap and the corresponding compounds (NiO, FeO, $LaMnO_3$, etc.) are charge-transfer insulators. In this case, the band gap is proportional to Δ.

If $U/W < \Delta/W$, the band gap is of $d-d$ type and thus a Mott-Hubbard insulator. They have a band gap of the magnitude U. The straight line $U = \Delta$ separates the Mott-Hubbard and the charge-transfer regimes. The diagram also contains a metallic region near the Δ/W-axis (d-metals as TiO, $YTiO_3$) or near the U/W-axis (p-metal as V_2O_3). This classification scheme is very useful for oxide materials science. More examples can be found in a review article of Imada [1].

2.5   Goodenough-Kanamori-Anderson rules

In the discussion of the magnetic exchange interaction in sections 2.3 & 2.4 we have examined only the simplest case of an electron in a non-degenerate or twofold degenerate d-orbital. In fact, this consideration for real materials often is too simple and has to be extended by the structure of the orbitals. Since the details of orbital structure determine e.g. the overlap with the oxygen $2p$-states and possible orbital degeneracy. Thus, the consideration of magnetic interactions can be very complex. Goodenough, Kanamori and Anderson [25, 44] formulated easy rules in order to predict in the most cases the right magnetic exchange interactions. In the following the *Goodenough-Kanamori-Anderson* (GKA) rules will be discussed on $LaMnO_3$.

As we have seen above, the $d-d$ overlap occurs via bridging of the oxygen p-electrons. Because of this, one has to regard the geometry of the relevant orbitals which are schematically illustrated in Figure 2.12. Here, the oxygen p-orbital is occupied by two electrons and directed towards or overlap with the Mn-ion. The electrons of the Mn $(3d^4)$ ion will be distributed in a difficult way: three electrons will occupy the t_{2g}-levels and generate a so-called *core spin* of $S = 3/2$, i.e. these electrons will stay at the Mn-atomic site and create a local spin. The fourth electron instead will occupy the energetically most favorable e_g-level, due to the benefit of the Jahn-Teller effect. In octahedral elongated systems it favors the d_{z^2}-orbital and can hop. The three arrows in Figure 2.12 denotes the core spin of the three t_{2g} electrons. Here in this example, the d_{z^2}-orbitals are directed towards the oxygen ions. As a result, one obtains three different options how to occupy these orbitals which finally lead to the three GKA-rules.

The *first GKA-rule* says, that *the 180°-exchange between filled or empty orbitals is relatively strong and antiferromagnetic*. The conclusion of this is illustrated in Figure 2.12(a,b). Both Mn ions have one (or none) electron in opponent adjusted d_{z^2}-orbitals, so that sometimes one speaks of the 180°-exchange between half-filled orbitals, having in mind that there is one electron at each orbital, and not two!
If the electrons in both Mn-O bonds hop like in a single level lattice, the itinerant spins of the adjacent Mn ions in the d_{z^2}-orbitals will align antiparallel. Since of the strong intraatomic Hund's coupling, the core spins have to be parallel to the according itinerant spins: i.e. the interaction between the magnetic moments of the Mn-sites finally is antiferromagnetically.

The *second GKA-rule* says, that *when the 180°-exchange is due to an overlap between an occupied and an empty orbital, the resulting exchange is ferromagnetic and relatively weak*. This rule is illustrated in Figure 2.12(c). The difference to (a) is that the bond of the oxygen and the Mn ion on the left and right hand side is different. On the left hand side the bond is analog to (a), but on the right side the d_{z^2}-orbital of the Mn ion is unoccupied and the corresponding orthogonal $d_{x^2-y^2}$-orbital is oc-
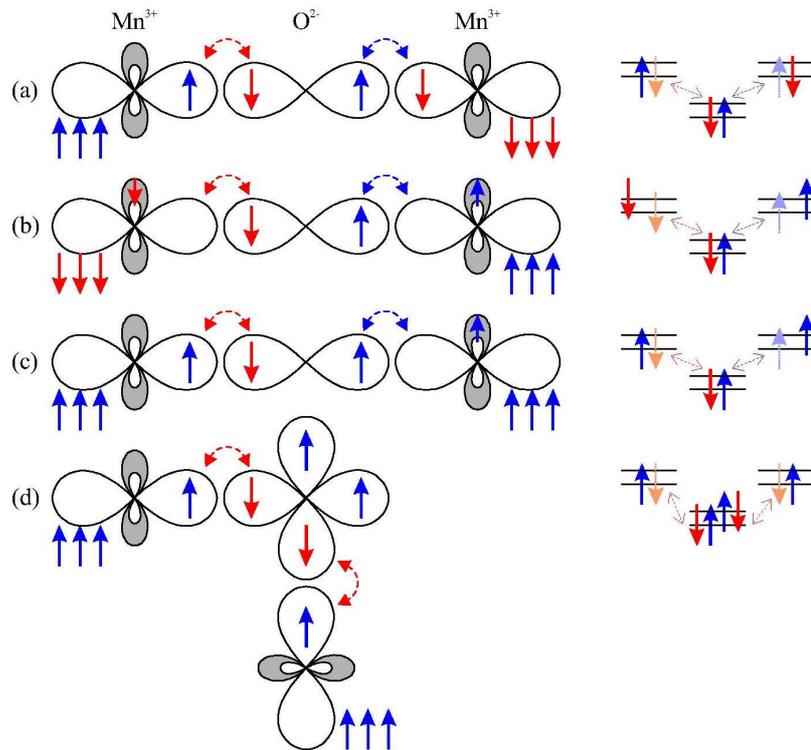
Figure 2.12: To clarify the Goodenough-Kanamori-Anderson rules, the $d_{x^2-y^2}$- (shadowed), and the d_{z^2}-orbitals (to the left and right) as well as the p_z-orbitals in the center of a Mn-O-Mn bonding are schematically illustrated. The small arrows in the orbitals describe the itinerant electrons, the three arrows outside the orbital denote the total core spin $S = 3/2$ of the three not shown t_{2g} orbitals. According to the realized occupation, either an antiferromagnetic (AF) (a,b) or a ferromagnetic (FM) (c,d) coupling will be established. [30].

cupied. Thus, the p-electron of the oxygen can hop into the empty d_{z^2}-orbital. The energetically most favorable configuration is reached when the electron will be build in with parallel spin, according to Hund's first rule. Instead of this, the p-electron on the left hand side prefers an antiferromagnetic ordering. As a result, the Mn spins order ferromagnetically.

The *third GKA-rule* says, *the 90°-exchange between (half-) filled orbitals is ferromagnetic and relatively weak.* Figure 2.12(d) shows the 90°-exchange between filled orbitals. Here, the hopping happens between a p_z-orbital and the left Mn ion and between a p_y-orbital and the right Mn ion. This means, that two holes remain in the oxygen in the virtual intermediate state. Due to the orientation of the Mn spins, the

two remaining electrons on the oxygen site have either a parallel or an antiparallel spin orientation.

Since the energy of the intermediate state is commonly written in the denominator of the corresponding energy, the state with the lowest energy will be favored. According to Hund's first rule, this is the state with parallel spin configuration of the electrons (or holes) at the oxygen site. Thus, the spins of the two Mn-ions are parallel, too. Then the energy difference between the parallel and antiparallel configuration is given by:

$$J \simeq -\frac{2t_{pd}^4}{\Delta^2} \left(\frac{1}{2\Delta + U_p - J_H} - \frac{1}{2\Delta + U_p} \right) \simeq -\frac{t_{pd}^4}{\Delta^2 (2\Delta + U_p)} \frac{J_H}{(2\Delta + U_p)} \qquad (2.12)$$

where J_H means the Hund's coupling energy and U_p the Coulomb repulsion between the two p-orbitals.

Together with these considerations it is now possible to explain the magnetic ordering of $LaMnO_3$, if we assume orbital odering in that way which is already shown in Figure 2.6. For more clearness the oxygen and unoccupied $d_{x^2-y^2}$ orbitals are not drawn. As we can see easily, in the horizontal plane an half-filled orbital is directed towards an unoccupied orbital, which means that the layers order ferromagnetically. Between the planes always empty orbitals overlap and this leads to an antiferromagnetically ordering.

2.6   Superexchange and double exchange interactions

In the following section we want to describe two important effects on which the previous introduced GKA-rules are based. Since magnetic dipole-dipole interactions between spins of adjacent Mn-ions generally are rather weak, exchange processes to establish a long range magnetic ordered ground states will be ascribed an important role. In such processes electrons and their related spins are able to hop from site to site and hereby reduce the energy of the system.

Exchange interaction between degenerated levels:

Considering a situation where one electron is taken at each lattice site. The new aspect now is that two energetically degenerated levels are free to be occupied. This is of high relevance for real crystals since at the lattice sites are ions with multiple degenerated levels, e.g. the e_g levels of LaMnO$_3$ without Jahn-Teller distortion. If one electron occupies one of these levels, another electron a different level, we, thus, declare in this model, that electrons occupy different single particle states. In this case, two electrons at the same lattice site may have the same spin without violating Pauli's exclusion principle. Figure 2.13 presents the four possible configurations of two adjacent sites 'left' and 'right' with the two degenerated levels d_{z^2} and $d_{x^2-y^2}$. The arrows represent the spins of the electrons in their corresponding orbitals. In the following it is necessary to replace t by t_{ij} in H_t of equation (2.5). To simplify matter we assume that $t_{ij} = t$ for $i = j$ and $t_{ij} = 0$ if $i \neq j$. This is a good approximation if the two considered orbitals are orthogonal to each other, so that the overlap and therefore the hopping between the orthogonal orbitals vanishes[2].

In Figure 2.13(a) Pauli's principle forbits a transfer of the electron, which leads to no change in energy ($\Delta E = 0$). In case (b) and (c) the gain in energy is similar to the above in section 2.3.1 discussed and is $\propto \frac{2t^2}{U}$.
If in the case of Figure 2.13(d) the electron hops from left to right, it has to bring up the Coulomb energy U, but wins the Hund's coupling energy J_H (in manganite compounds ≈ 1.5 eV). Because of Hund's coupling energy, configuration (d) is the energetically most favorable state. From the orientation of the spins in (d) one can immediately conclude, that ferromagnetic correlations of the spins of adjacent Mn-ions exist, in contrast to the one-level lattice in the previous section 2.3.1.
Simultaneously the occurrence of an orbital ordering will be favored. To transfer this result on LaMnO$_3$ two small difficulties appear. Firstable, a Mn-ion has more than only one electron in its $3d$-shell and second, between the Mn-ions are O^{2-}-ions, so that primary these Mn-spins can not interact directly. Instead of this, an interaction *via the diamagnetic ion* will be realized.

---

[2]This means, that the electrons can not hop into the shadowed orbital (see Figure 2.13).
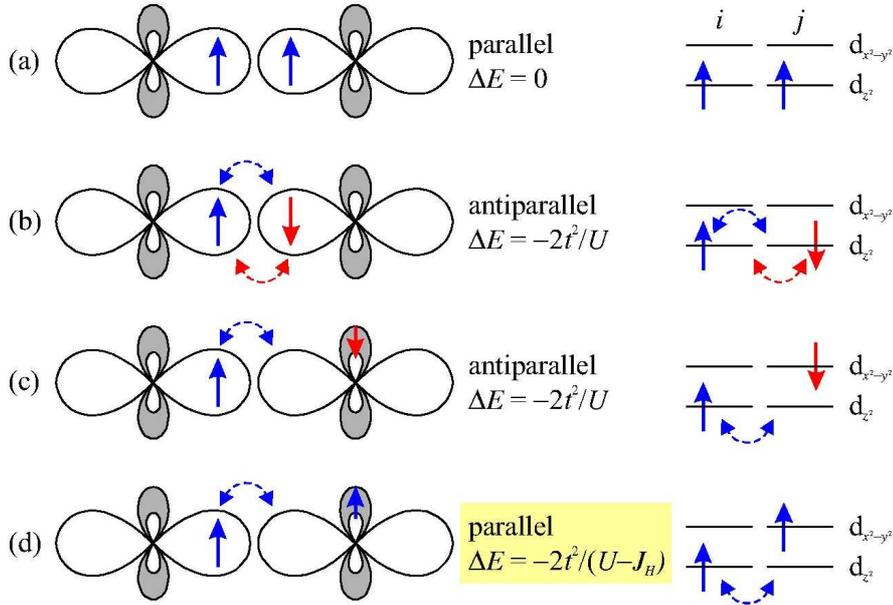
Figure 2.13: Schematic illustration of the superexchange in case of two-fold degenera-
tion with respect of Hund's coupling for opposite directed d_{z^2}- and related
$d_{x^2-y^2}$-orbitals (shadowed). The most favorable configuration leads to fer-
romagnetic correlations [40].

As a result, an energy difference between antiparallel (b,c) and parallel (d) spin
configuration can be evaluated, according to equation (2.8) an effective exchange
constant J_{ex} which is

$$J_{ex} \simeq \frac{2t^2}{U} - \frac{2t^2}{U - J_H} = \frac{2t^2 J_H}{U^2 - J_H \cdot U} \simeq \frac{2t^2}{U} \frac{J_H}{U}. \tag{2.13}$$

Here we have taken into account, that commonly $U \gg J_H$. As one can see, one gets
a ferromagnetic exchange which is rather weak due to $J_H/U \ll 1$.

The double exchange interactions

In 1951 Zener [45] offered an explanation for the behavior of the indirect magnetic
exchange between $3d$ atoms. He considered that the intraatomic Hund rule exchange
was strong and that the carriers do not change their spin orientation when hopping
from one ion to the next, so they can only hop if the spins of the two ions are
parallel. On minimizing the total free energy of the system, Zener found that ferro-
magnetic interactions are favored when the magnetic atoms are fairly well separated

and conduction electrons are present. The theory was applied to the manganese per-
ovskites [45] with the aim of explaining the strong correlation between conductivity
and ferromagnetism, and the value of the zero-temperature saturation magnetiza-
tion which corresponds to the sum of all the unpaired electron spins. Starting from
the insulating antiferromagnetic $LaMnO_3$ end member where electrons are localized
on the atomic orbitals, Zener showed how the system should gradually become more
ferromagnetic upon hole doping (introduction of Mn^{4+}). He considered the problem
of the exchange between Mn^{3+} and Mn^{4+} ions via an oxygen ion and introduced the
concept of simultaneous transfer of an electron from the Mn^{3+} to the oxygen and
from the oxygen to the neighboring Mn^{4+}, which is schematically shown in Figure
2.14. Such a transfer is called *double exchange*.
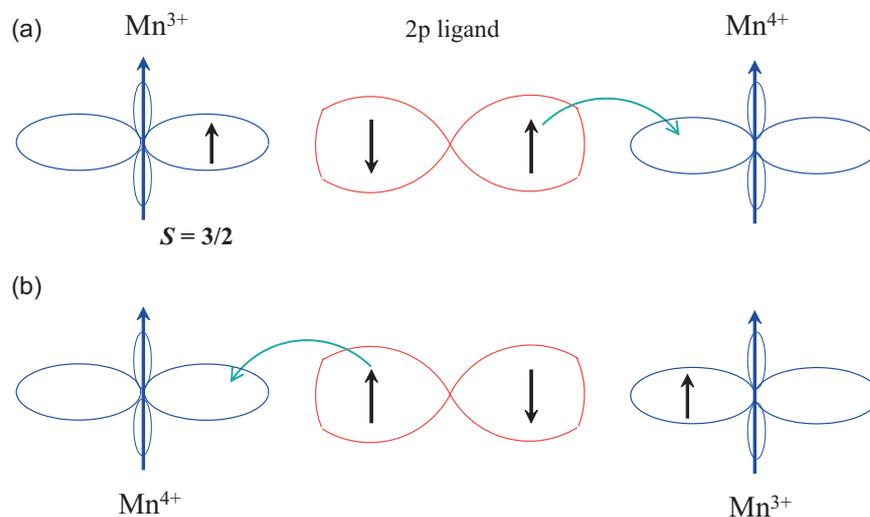
Figure 2.14: Illustration of the double exchange mechanism.

In the case of magnetic atoms, the configurations Mn^{3+}-O^{2-}-Mn^{4+} and Mn^{4+}-O^{2-}-
Mn^{3+} are degenerate if the spins of the two d shells are parallel, and the lowest
energy of the system at low temperature corresponds to parallel alignment of the
spins of the two adjacent cations. Double exchange is always ferromagnetic, unlike
superexchange which involves virtual electron transfer and is frequently antiferro-
magnetic. If the manganese spins are not parallel or if the Mn-O-Mn bond is bent,
the electron transfer becomes more complicate and thus the mobility decreases. It
follows that there is a direct connection between conductivity and ferromagnetism.

Chapter 3

Experimental details

3.1 Techniques for high pressure

3.1.1 The diamond anvil cell

The beginning of the 20th century signifies the beginning of the high pressure era. In the *Bridgman era* (1910 - 1950) the basics of high pressure cells were set with pressures up to 10 GPa[1]. These cells were used for conductivity as well as for compressibility measurements [46]. For his big efforts in that matter, P.W. Bridgman was honored with the Nobel price in 1946.

The basic principle of high pressure cells are two opposite anvils which will be pressed together. One of the most powerful high pressure cells nowadays is the *diamond anvil cell* (DAC) which is schematically illustrated in Figure 3.1 [47, 48, 49, 50, 51]. The DAC's used in this thesis are modified high pressure cells following the example of Merrill-Bassett [52]. They work on basis of the Bridgman-principle [46]. The reason why taking diamonds as anvils is simple: Diamonds are the hardest material on earth which make them fit perfectly for the use under high pressure conditions.

The DAC in general consists of two opposite diamond anvils which press on a piece of sample by applying external force. In order to prevent a lateral flow out of the sample by applying pressure, both anvils are supported by a metallic ring, which is called the *gasket* and generally consists of a very hard alloy[2]. In the center of this gasket a small drilled hole ($\oslash$ 150 - 350μm) defines the sample chamber and contains the sample, a pressure media and a pressure marker. The pressure media is necessary in order to achieve hydrostatic or quasi-hydrostatic conditions and can be either liquid nitrogen, liquid helium, oil or epoxy. The pressure marker is to

---

[1]1 GPa = 10 kbar.

[2]For all high pressure experiments with the DAC, we used Inconel 750 (Fe-Co alloy) as gasket material, except for the measurement of the Co spin-state in section 3.9 where we used an alloy of $Ta_{90}W_{10}$.
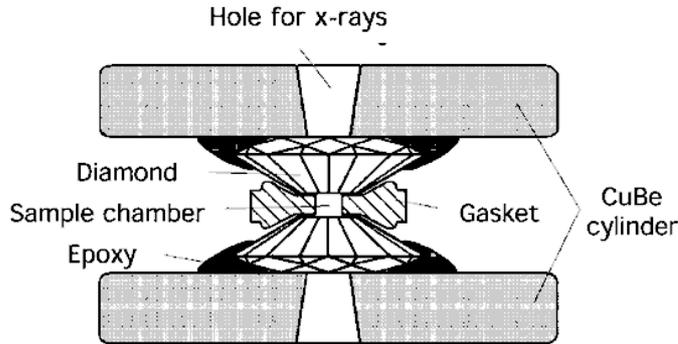
Figure 3.1: Simple schematic sketch of a Diamond Anvil Cell (DAC) used for the high
pressure experiments. Due to their small sizes (22 mm in diameter and $\approx$
14 mm in height) the DAC is suitable for most measuring apparatus.

determine the internal pressure and consists of small ruby[3] chips.

Typical diameter of the diamond anvil surface, which is called the *culet*, differs in
our research group between 0.2 and 1.3 mm. Pressures up to approximately 100
GPa can be achieved according to the pressure range required with a culet of $\leq$ 0.2
mm.

As shown in Figure 3.1, this design is suitable for spectroscopic measurements like
x-ray diffraction or Mössbauer spectroscopy under high pressure. A detailed descrip-
tion about the preparation of the DAC for spectroscopic as well as for resistivity
measurements is given elsewhere [53]. In order to perform electric resistivity mea-
surements under high pressures, the preparation of the cell has to be modified.
Electrical conductors - at least 12 μm tiny gold wires - have to be inserted into
the sample chamber and contact the sample. Before, the metallic gasket has to be
insulated in order to protect the sample against short-circuit. For this purpose, the
imprint of the diamonds in the gasket will be covered by a small piece of capton[4]
foil. The glue for this consists of a mixture of epoxy (Uhu Endfest 300) and Al_2O_3
and serves as pressure medium to provide quasi-hydrostatic conditions. Afterwards,
a small hole ($\oslash \approx$ 100 - 250 μm) will be drilled in the center of the capton which
defines the sample chamber. Then, five flattened gold wires will be taped on the
facet side of the lower diamond. Their sharpened end will be kinked on the culet,
so that their top reach in the center of the sample chamber. Finally, the other end
of these wires will be soldered to five 100 μm Cu wires, which conduct the signals to
the measuring apparatus. The last step is to fill the powder sample into the sample

---

[3]Ruby = Corundum = Al_2O_3 doped with Cr^{3+}.

[4]Capton is a very special kind of insulating foil made of Polyimid and used in space technology
e.g. for satellites for more than 30 years. It is electrical, chemical and mechanical stable also under
extreme conditions.
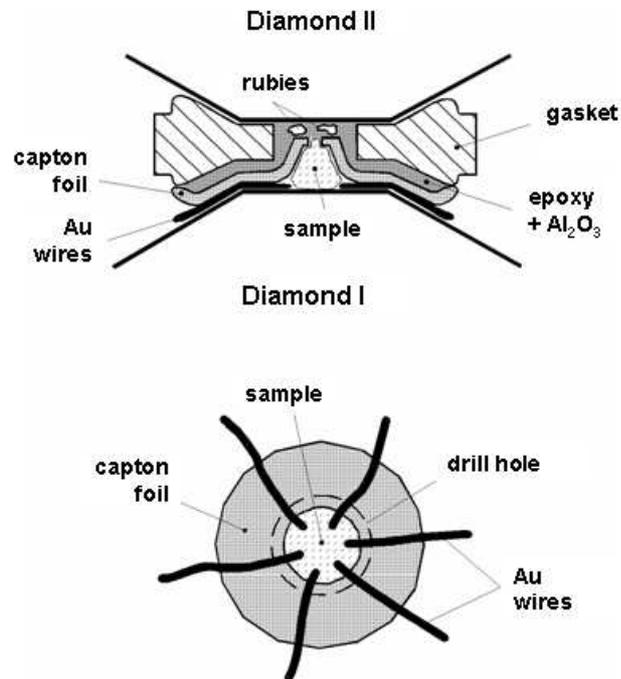
Figure 3.2: Schematic view of the preparation of the DAC for high pressure electrical resistance measurements.

chamber, together with some ruby chips for the pressure determination (see below). Then the cell can be closed and looks like in Figure 3.2.

One final comment for the reason why taking five wires instead of four, since we are doing a four-point measurement: Due to the mechanical strain on the delicate wires, during closing the cell and applying pressure, it unfortunately belongs to the business that sometimes gold wires remove from their initial position and contact other wires which leads to a short-circuit. Also very unpleasant after closing the cell are breakages of the wires at the sharp edge of the culet. Thus, we use the fifth wire just for safety reasons.

Pressure determination of the DAC:

An elegant way to determine the pressure inside a DAC possesses the ruby fluorescence method. Through the transparent diamonds, a laser beam excites the ruby chips to emit fluorescence light. In principle, this fluorescence spectrum consists of two lines (R_1 and R_2) which have a wave length of 692.70 nm and 694.25 nm at

ambient pressure, respectively. By increasing pressure, these lines shift to higher wavelengths. According to their higher intensity, the R_2-line is taken as reference line to determine the pressure by following equation:

$$p(\text{GPa}) = 380.8 \left\{ \left(\frac{\Delta\lambda(nm)}{694.25nm} + 1 \right)^5 - 1 \right\} \text{GPa}, \qquad (3.1)$$

whereas $\Delta\lambda = \lambda - \lambda_0$ with $\lambda_0 = \lambda(\text{p} = 0 \text{ GPa}) = 694.25$ nm. This conforms the drawn through line in Figure 3.3(a) which is the result of x-ray diffraction measurements on Ag, Cu, Mo and Pd [54]. For pressures below 30 GPa one can use the more simple equation, assuming the following linear apporoximation [49, 50]:

$$p(\text{GPa}) = 2.746 \times \Delta\lambda(\text{nm})\text{GPa} \qquad (3.2)$$

Here it should be mentioned, that one big disadvantage of this method is that the pressure can not be measured in-situ. Pressure can only can be determined at room-temperature and outside the measuring apparatus. However, due to different thermal expansion coefficients of various parts of the cell, pressure can increase at low temperatures. Thus, the pressure was determined before and after each measurement. According to references [55] and [56], temperature increases the pressure by less than 10 % between 25 and 300 K.
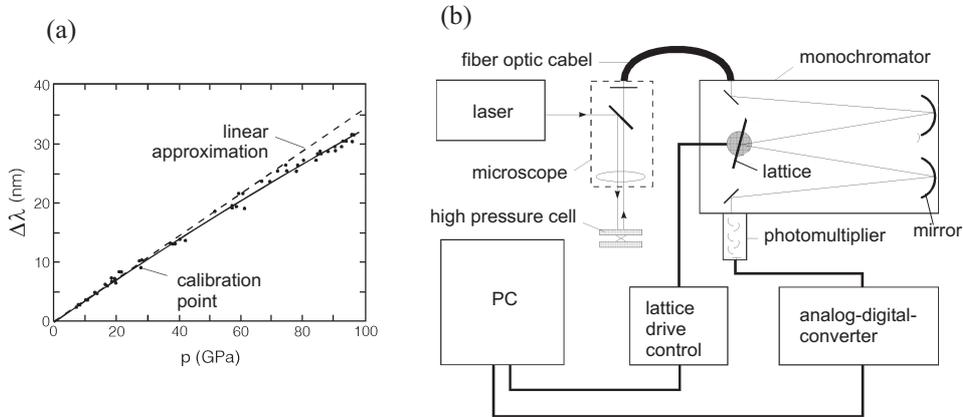
Figure 3.3: (a) Relative change of wavelength of the R_2-ruby fluorescence line under pressure. The drawn through line conforms eq. (3.1), the dashed line conforms the linear approximation eq. (3.2) [54]. (b) Technical setup for the pressure determination [57].

The experimental equipment to determine the pressure is schematically illustrated in Figure 3.3(b). A powerful blue laser inducts its light into the optical path of a microscope and excites the ruby chips to emit fluorescence light. This light will be

collected by several lenses and transmitted via a fiber optics wire to the monochromator, which reads out the interesting wavelengths supported by a rotating lattice. A photomultiplier behind the monochromator absorbs all the light and amplifies the signal. This signal will be sent to an analog-digital converter which prepares the signal for the PC, where the spectrum will be presented and the pressure calculated.

3.1.2   Large volume cell

The *large volume high pressure cell* was used for measurements of the electric resistivity on $La_{0.82}Sr_{0.18}CoO_3$. This type of high pressure cell is made of Titanium alloy[5] which is extremely hard and possess a very small thermal expansion coefficient $\alpha = 9.3 \cdot 10^{-6}$ to guarantee stable pressures at low temperatures. The cell is specially made for direction dependent measurements of the conductivity of single crystals as well as for sintered sample pieces. With this type of cell, pressures up to $p \approx 30$ GPa can be achieved.

The anvils consist of sintered diamond powder induced into a Co matrix. This is called a *black diamond* and their hardness is comparable to that of natural diamond. The used anvils, with a culet of 4 mm, are covered by Tungsten-Carbide (WC) and pressed into a Cu-Be support ring which hold the anvils and enables a safe and vertical guidance inside the cell body in order to protect the anvils against misalignment and destroying (see Figure 3.4).
In order to prepare the high pressure cell for resistivity measurements, a pyrophyllit ring with the diameter of the culet and ~ 300 μm in height was glued on top of the lower anvil. This ring prevents a lateral flow-out of the sample. The inner part of this ring ($\oslash$ 2 mm) defines the sample chamber. In order to protect the sample against short-circuit from the anvils, a piece of capton foil was fixed on the lower anvil. Above the capton a ~ 100 μm thick piece of steatite[6] was placed which is considered as pressure medium and provides quasi-hydrostatic conditions. On top of the steatite, the sample[7] ($100 \times 25 \times 300$ μm in size) and a small piece of lead[8] (to determine the pressure) were contacted, each with four 12 μm Au wires for a 4-point resistivity measurement, as shown on the right hand side of Figure 3.4. By measuring the temperature dependence of $R(T)$ of Pb, one can follow the transition temperature T_C of the pressure dependent superconducting state with increasing pressure [59].
In the following the Au wires were contacted to larger and bigger Cu wires which led the signals out of the high pressure cell. On top of the sample another piece of steatite and capton foil was taken to cover the upper anvil against short-circuit and

---

[5]4 % Vanadium, 6 % Aluminium and 90 %Titanium
[6]very soft mineral
[7]lower piece in the sample chamber shown on the photo on the right of Figure 3.4
[8]upper piece in the sample chamber shown on the photo on the right of Figure 3.4

to provide quasi-hydrostatic conditions. Under pressure, the Au wires were pressed on the surface of the sample and guaranteed hereby a good electric contact. This is called the *press contact method*. A more detailed description of preparing this large volume high pressure cell can be found elsewhere [58].
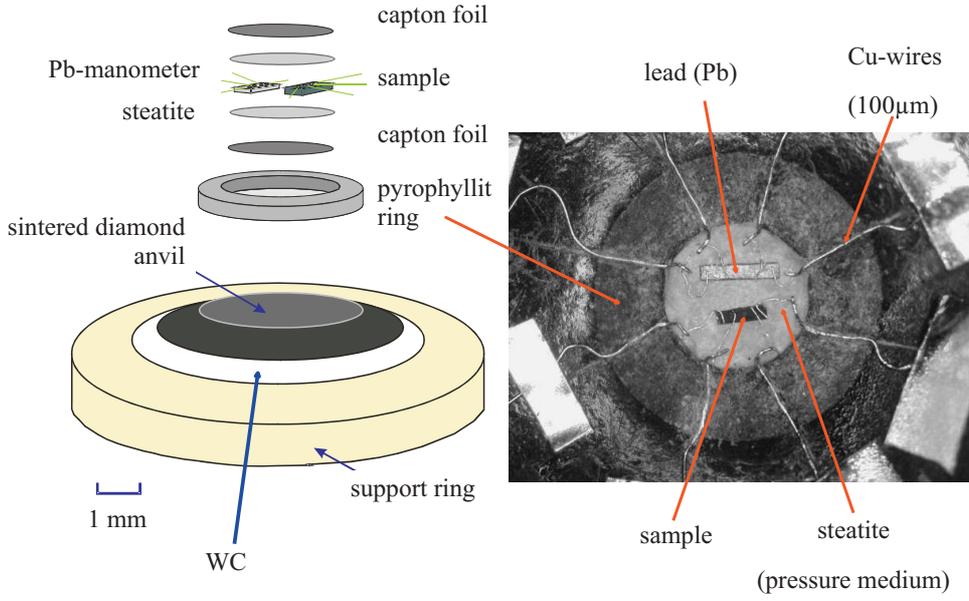
Figure 3.4: Schematic order of preparation (left) and photo of the prepared high pressure clamp for resistivity measurements just before pressurization. One can see the single crystal sample and a piece of lead to determine the pressure.

3.2 High pressure experimental methods

3.2.1 Electrical resistivity

All temperature dependent electric resistivity measurements have been performed in a standard ^{4}He-bath cryostat. In this cryostat it is possible to measure temperatures between 1.5 and 600 K. For the temperature dependent measurements of the electric resistivity $R(T)$ a high pressure cell was mounted into the massive Cu pot at the bottom of an *insert* (see Figure 3.5). This insert has been inserted into the Helium chamber of the cryostat. Since we have performed measurements at low as well as high temperatures, we have used two different but in their construction similar inserts: one for temperatures from 1.5 to 300 K (Figure 3.5) and the second for
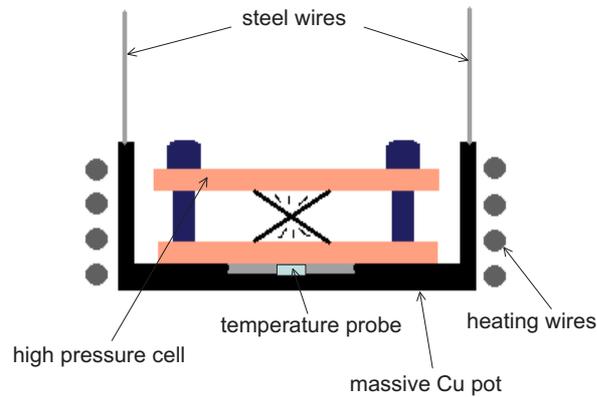
Figure 3.5: Schematic sketch of the low temperature insert for the ^{4}He cryostat.

temperatures between ~ 200 and 600 K (Figure 3.6). In principal both inserts consists of a massive Cu pot with a groove in their centre where the cell and a temperature probe fit in perfectly. Outside the Cu pot of the *low temperature insert*, wires are winded which work as a heater to warm up the system. At the bottom of the *high temperature insert* a strong ceramic heating element (Mica) (see Figure 3.6) has been mounted which heats up the whole Cu pot up to at least 600 K.
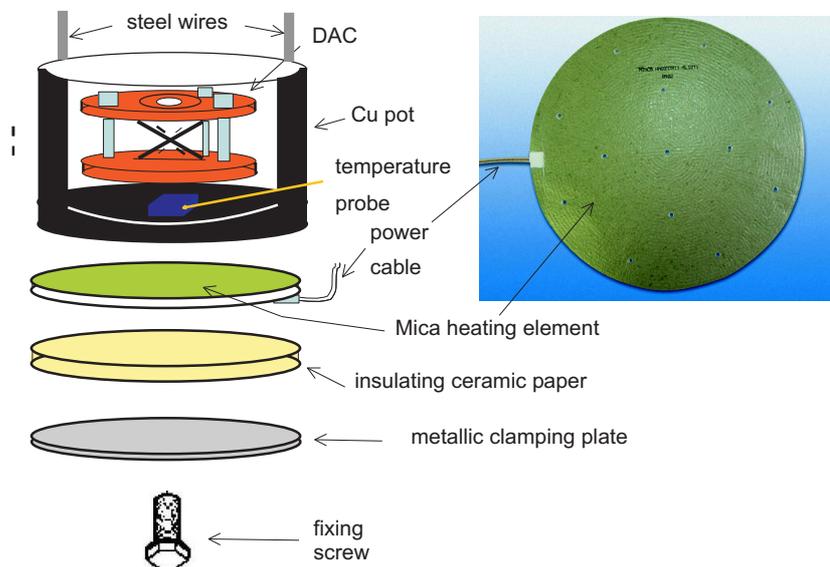
Figure 3.6: Schematic view of the high temperature insert with the Mica heating element mounted below the Cu pot.

Both Cu pots hang on steel wires which are connected with the top of the cryostat. To provide the cell, thermometer probe and heating with current, a couple of small wires lead along the catenary wires from the pot upwards to a Helium-sealed connector in the flange. On the outer side of this flange another cable conducts all the signals to an interface and then to the PC.

3.2.2 Magnetization

In collaboration with Dr. S.S. Saxena from the high pressure group of the Cavendish Laboratory at University of Cambridge, we performed measurements of the pressure dependence of the magnetization in a pressure cell [60], up to 1.0 GPa and down to 2 K by means of a superconducting quantum interferometer device (SQUID) magnetometer.

The high pressure cell is a cylindrical hydrostatic pressure cell based on a single walled-design. The materials composing the cell are specially selected to give the lowest magnetic background possible and maintaining high mechanical strength in order to withstand thermal and pressure cycles. The overall dimensions of the pressure cell have been optimised to give the maximum of sample space whilst still fitting in the sample space of the SQUID.

The overall length of the pressure cell is ~ 60 mm with an outer diameter of 8.5 mm. The available sample space is typically 1.9 mm diameter and 10 mm maximum long. The total weight of the pressure cell assembled and ready to be mounted is 17 g. The recommended maximum sample size is of $1.5 \times 1.5 \times 5$ mm, which is within the acceptable limit to give a reasonable dipole response on the SQUID for most magnetic measurements.

With this cell, measurements of samples with magnetic moments as low as $5 \cdot 10^{-6}$ to $10^{-5} \mu_B$ are possible. Figure 3.7 presents a view of used the high pressure cell.

In order to apply pressure, a hydraulic pressure ram has been used which was capable of generating at least 1.5 ton of force. Indeed, due to the relative small size of the cell it was essential to ensure the vertical alignment of all components during the pressurisation process. Otherwise, irreversible damages could be caused to the pressure cell.

For pressure determination, the shift of diamagnetic signal from the superconducting transition temperature of a standard Sn [59] sample has used.
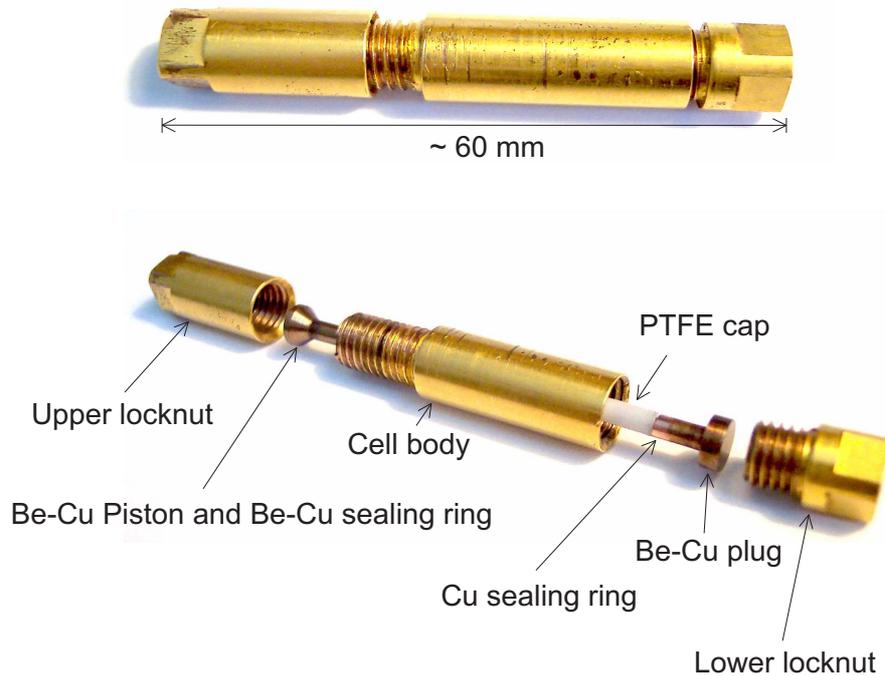
Figure 3.7: Schematic view of the Cambridge SQUID cell.

3.2.3 Energy dispersive x-ray diffraction

x-ray diffraction is an established tool to determine the adjustment of atoms in a crystal. This provides informations about the lattice parameters of the examining sample. The principle of this method is based on Bragg's law of reflection:

$$n \cdot \lambda = 2d \cdot \sin \theta, \tag{3.3}$$

whereas n is the order of diffraction, λ the wave length, d the distance between successive grating elements, called the grating spacing and θ the half diffraction angle. Constructive interference occurs only then, when the incident x-ray beam strikes the grating elements under the above mentioned diffraction angle θ.

There are different kind of methods to perform x-ray diffraction measurements under high pressure. Commonly the *Debye-Scherrer method* will be used, since it is sufficient to analyze powder samples. Other methods require single crystals which are not easy to produce and often will be destroyed by applying pressure. So, for examining crystal structures under pressure, two different possibilities are available:

The first one is the *angle dispersive x-ray* diffraction. Here a monochromatic x-ray beam strikes the powder sample which consists of many statistically distributed crystallites. For some parts of these crystallites, Bragg's law is satisfied and constructive

interference occurs. Hereby every grating plane produces, due to the statistic distribution of the crystallites, an own diffraction cone (Debye-Scherrer ring) with an aperture angle which is typical for each grating plane. Today such a Debye-Scherrer ring will be detected either with a rotating detector or an image plate. The resolution of this method is quite better than that of the method described hereafter. Furthermore, the angle dispersive diffraction shows no fluorescence lines and can reduce texture effects to a minimum.

A second method to investigate the crystal structure is the *energy dispersive* x-ray diffraction using synchrotron radiation, which was used to examine the lattice parameters of the samples under pressure. Behind the sample an energy dispersive detector is mounted in a fixed angle to collect all diffraction lines from many grating planes of the sample which strike the detector under the diffraction angle θ. These different angles correspond to different energies and can be evaluated in the PC. In comparision to the angle dispersive method, the resolution of this method is a bit lower. Frequently the texture leads to troubles in spectra since only a part of the whole Debye-Scherrer ring is measured. Additionally fluorescence peaks can appear which can overlap with some diffraction peaks. On the other hand, this method has also some advantages: All diffraction patterns can be measured at the same time and visualized immediately on the monitor. This makes changes in the spectra apparent quite fast. Moreover, the time to measure a spectrum is much less than for the angle dispersive x-ray diffraction.

The diffraction lines appear at specific energies, E, which are related to the corresponding interplanar spacings, d, by the Bragg-equation (3.3):

$$Ed = \frac{h \cdot c}{2 \cdot \sin \theta} = \frac{6.1993 \text{keV Å}}{\sin \theta}. \tag{3.4}$$

with h = Planck constant, c = speed of light. This equation shows the relationship between the incident energy E and the d values.

Equation of state

The energy dispersive x-ray diffraction measurements were performed in order to determine the lattice parameters, the elastic bulk modulus B as well as to study possible structural phase transitions under high pressures. The bulk modulus in units of pressure is an important parameter relating the change of volume with pressure. B is defined as

$$B = -V \frac{\partial p}{\partial V}\bigg|_{T}, \tag{3.5}$$

whereas V stands for the volume of the unit cell and p the applied pressure at constant temperature. Generally, B increases when the crystal is compressed. The actual state for solids under strong compression can be described by several *equations of state* (EOS) [61]. For samples examined in this thesis, it is sufficient to assume a linear pressure dependence of B[9] due to a small change of the volume, according to the propose of Murnaghan [62, 63]. Then B reduces to:

$$B = B_0 + B_0' \cdot p. \tag{3.6}$$

Then the EOS can be obtained by integration as following:

$$\int_{V0}^{V} -\frac{dV}{V} = \int_0^p \frac{dp}{B} = \int_0^p \frac{dp}{B_0 + B_0' \cdot p}. \tag{3.7}$$

$$\ln\left(\frac{V_0}{V}\right) = \frac{1}{B_0'} \ln\left(\frac{B_0 + B_0' \cdot p}{B_0}\right) = \ln\left(\frac{B_0 + B_0' \cdot p}{B_0}\right)^{\frac{1}{B_0'}}. \tag{3.8}$$

$$\left(\frac{V_0}{V}\right) = \left(1 + \frac{B_0'}{B_0} \cdot p\right)^{\frac{1}{B_0'}} \Rightarrow V(p) = V_0 \left(1 + \frac{B_0'}{B_0} \cdot p\right)^{-\frac{1}{B_0'}} \tag{3.9}$$

whereas V_0 is the value of the unit cell at $p = 0$ GPa. The Murnaghan EOS is valid for changes in the volume up to $V/V_0 > 0.85$. For larger volume changes one has to introduce additional parameters as shown in [64], which lead e.g. to the *Birch-Murnaghan* equation of state [65].

---

[9]which generally can be developed in a power series: $B = B_0 + B_0' \cdot p + B_0'' \cdot p^2 + \ldots$

Beamline F3 at Hasylab

All measurements determining the lattice parameters under high pressure were per-
formed at room temperature with energy dispersive x-ray diffraction spectroscopy
using synchrotron radiation (SR) at beamline F3 of Hasylab in Hamburg (Figure
3.8).
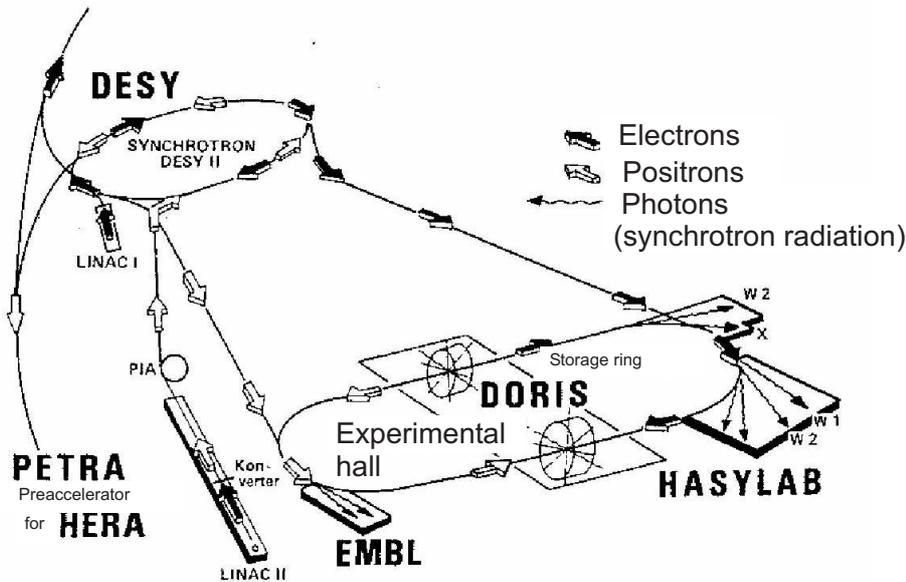
Figure 3.8: Schematic sketch of the different accelerators at DESY (Deutsches Elektro-
nen Synchrotron) in Hamburg. The linear accelerator (LINAC) and the
synchrotron (DESY) accelerate electrons and positrons, respectively before
they are pipelined into the storage ring (DORIS). The abbreviations EMBL
and Hasylab are different experimental halls.

This beamline receives the "white"[10] SR beam from a bending magnet of the storage
ring DORIS and is optimized for energy-dispersive powder diffraction. It is espe-
cially geared for work with high pressure diamond anvil cells. Because of the small
sample sizes involved in this work, the equipment has been optimized for background
suppression and generation of small and well-defined beam sizes down to $20 \times 20 \, \mu$m.

For energy-dispersive x-ray diffraction, there is a Ge detector (with a resolution of
about 1%) for scattered radiation in the horizontal plane at angles up to $2\theta = 30°$.
An adjustable double-slit system serves to reduce the Compton scattering from the

---

[10]"white" means that the beam contains continuous (multichromatic) light.

diamonds and improves the resolution. This system rotates with the detector and allows rapid changes in the diffraction angle. A Huber diffractometer serves for sample translation, rotation and tilting, and for detector alignment (angle changes) in the energy-dispersive mode. The precision of the translations is below 1μm, that of the rotations and tilts 0.5 millidegrees.

A PC coupled to the multi-channel analyzer is used for data collection and storage in the energy-dispersive experiments [66, 67, 68].

Further instrumentation specifications:
- Source: 4.5 GeV by bending magnet, $E_c = 16$ keV
- Beam characteristics: white beam
- Beam size: < 200 μm adjustable; vertical electron beam divergence 0.11 mrad FWHM
- Detector: Ge semiconductor (solid state)
- Angular range: $0 < 2\theta < 30°$ (horizontal only)
- Energy resolution: $\Delta d/d = 10 \times 10^{-3}$ above 26 keV

3.2.4 K β x-ray emission spectroscopy

At the inelastic[11] x-ray scattering beamline ID16 at ESRF, x-ray emission spectra
of radiative decays can be measured to get information about the spin-state in TM
ions. For this purpose, a method discovered in the early 20th century is used. This
method is the Kβ x-ray emission spectroscopy (XES) [69, 70].

The main ambition to measure the Kβ x-ray emission is to use the Kβ decay ($3p \rightarrow$
$1s$) as an internally referenced spin detector, which allows to investigate spin-resolved
x-ray absorption experiments [71]. It is also found out that the Kβ emission spec-
troscopy is very sensitive to the spin-state in TM ions since the $3p$-$3d$ exchange
interaction is very strong (about 15 eV [72]) which makes it very attractive to verify
theoretical calculations as well as to deduce results from other experimental meth-
ods. In the following we briefly want to introduce into this technique.

The main principle of XES is that one excites an atom and observes the radiative
decay of its excited state. In our case, we excited the Co atoms of $La_{1-x}Sr_xCoO_3$ (x
= 0.18) with an energy of $\approx$ 13 keV, which is far from resonance and larger than the
emission energy of around 7.65 keV. As a result, this 13 keV incident beam kicks off
the $1s$ electron of the K-shell and induces a hole which will be refilled by an electron
from the higher $3p$ shell as schematically shown in Figure 3.9. Due to the decay of
the $3p$ electron a characteristic radiation will be emitted which is directly connected
to the exchange interaction between the $3p$ core hole and electrons of the partially
filled $3d$ shell, since these two states are very close to each other.
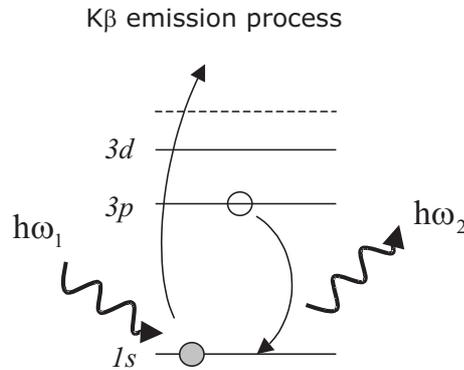
Figure 3.9: Schematic picture of the Kβ inelastic x-ray emission spectroscopy (XES).
The incident beam kicks off the 1s-electron of the K-shell. As a result, an
electron of the $3p$ shell of the TM ion decays into the K-shell and generates
the characteristic Kβ spectra which provides informations about the spin-
state of the system.

---

[11]To consider the process *inelastic* is due to the fact, that one pumps more energy inside than
one gets out.

In particular, the exchange interaction between the core hole and the local moment leads to a splitting of the K β spectrum mainly into HS (satellite peak, K β', $3p \uparrow 3d \uparrow$) and LS (main peak, K $\beta_{1,3}$, $3p \downarrow 3d \uparrow$) final states (see Figure 3.10).
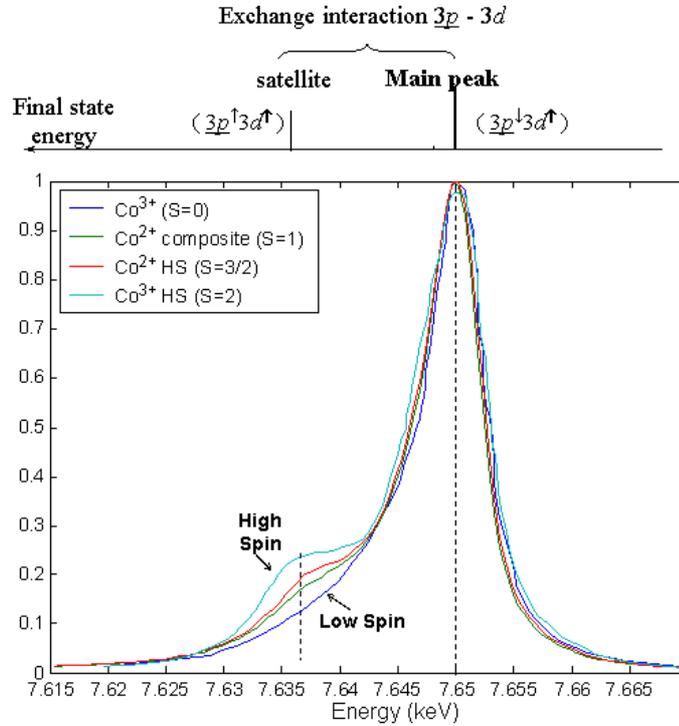
Figure 3.10: Typical Kβ emission spectra of Co based compounds with $S = 0$ (LS), $S = 1$, $S = 3/2$ and $S = 2$ (HS). The $3p$-$3d$-interaction is responsible for the grow of a satellite peak on the low energy side of the emission line. Its intensity and separation from the main peak mainly correlates with the net spin S [73]. Spectra of Co^{3+} ($S = 0$), Co^{2+} ($S = 1$), Co^{2+} ($S = 3/2$) and Co^{3+} ($S = 2$) [74].

The energy separation between these two peaks can be described by $\Delta E = J(2S + 1)$, where J denotes the exchange integral and S the total spin of the $3d$ shell, while their intensity ratio can be calculated as $S/(S + 1)$ [75]. When configuration interactions are taken into account, both the energy splitting as well as the intensity ratio will be modified [76]. These calculations show that the $3p \downarrow 3d \uparrow$ final state is characterized by a single peak that constitutes most of the intensity of the main emission line (K $\beta_{1,3}$), whereas the $3p \uparrow 3d \uparrow$ final state appears as a very small satellite component at lower energy. However, the simplified picture does not point out the qualitative changes expected for the $3d$ electrons going from HS to LS states, namely, smaller energy splitting between the main peak and the satellite as well as a reduction in the satellite to main peak intensity ratio.

In the following we briefly describe the experimental setup of beamline ID16 where the high pressure measurements on $La_{0.82}Sr_{0.18}CoO_3$ have been carried out (see Figure 3.11). The operating status of the storage ring during the measurements was the $2 \times 1/3$ filling mode, i.e. 2 times one third of the storage ring is filled. The 2 one thirds are separated by an empty gap of 1/6th of the ring. The maximum intensity was 200 mA. After the bending magnet the SR beam passes three undulators (type U35) which enhanced the beam's energy. Behind the undulators the energy is rather widespread but still has some structure in its spectrum (s. bottom of Figure 3.11) due to the interference effects as the beam passes through (undulates). The undulated beam then passes a lead enclosed vacuum tube (white-beam transfer line) to the high-heat load silicon (1 1 1) monochromator. The monochromator
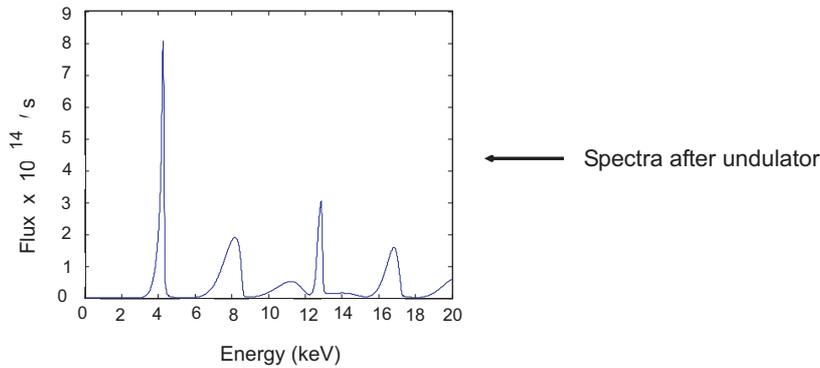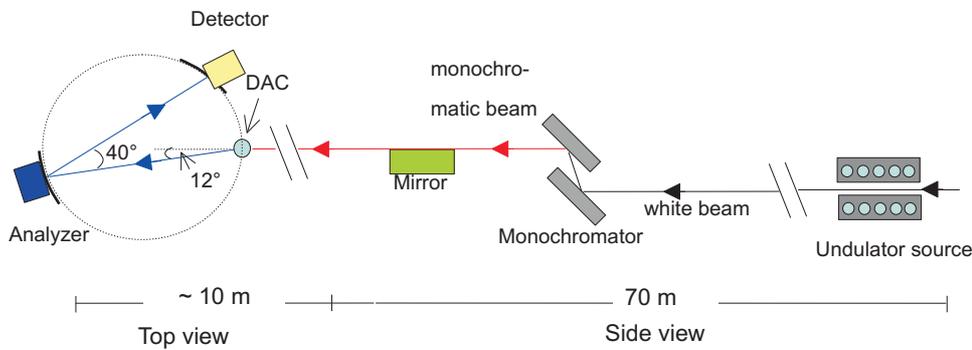
Figure 3.11: Schematic overview of the experimental setup of beamline ID16 at ESRF. The SR light comes from the storage ring and passes the undulators (spectrum after undulators see below). Then, the beam will be monochromized and guided through a mirror which focus the beam. Finally the beam goes through the sample and enters the XES spectrometer (analyzer and detector).

slice a thin energy band in the undulator spectrum of ~ 1.7 eV bandwidth centered at 13 keV for instance. The monochromatic x-ray beam was then transferred via the monochromatic-beam transfer line to the focusing mirror where the beam was focused to a size of 100×200 μm.

For the high pressure experiments with the DAC, we used the transmission geometry to measure the Kβ emission spectra. The typical count rate at the K β main line in the pressure cell was ~ 500 counts/s. The analyzer was placed in a small angle of $2\,\theta = 12°$ directly behind the cell. The setup of the XES spectrometer which was of Rowland circle geometry type with a 1 m diameter consists of a spherically bent Si analyzer (wafer) which works in Bragg reflection and a Peltier-cooled Si diode as detector. The Rowland circle geometry imposes the analyzer bending radius corresponding to the spectrometer diameter. The x-ray emission spectra were recorded by scanning the analyzer Bragg angle while, at the same time, the detector was translated perpendicularly to the analyzer direction, following the displacement of the x-ray spot. All the motors and electronics could be controlled in the control cabin outside of the experimental hutch where also the PC's for the data analysis were placed.

(a)   (b)
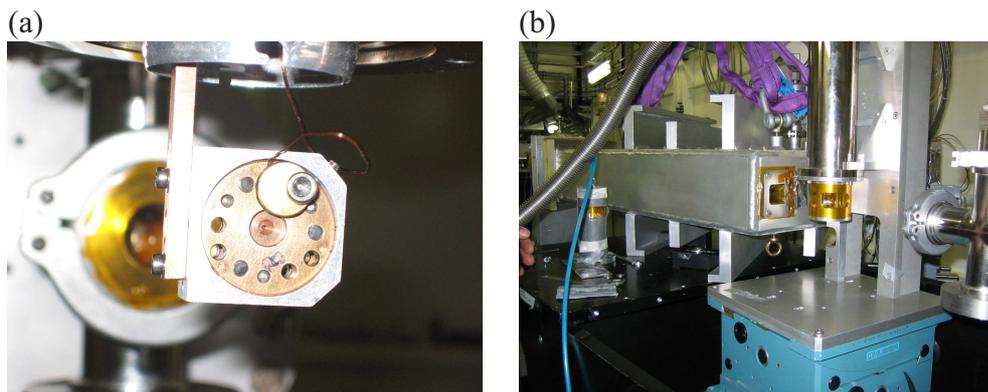
Figure 3.12: Photos made at the beamline. (a) High pressure cell mounted on the cold finger of the cryostat. SR comes from the right, the spectrometer is situated behind the pressure cell. The button on the pressure cell is the temperature probe; (b) Transmission geometry of measurement: the beam comes from the right hand side. The high pressure cell now covered by a vacuum sealed Aluminium pot with slits for the beam which are coated with capton foil. The spectrometer is on the left hand side.

3.2.5   Nuclear forward scattering of synchrotron radiation

Nuclear Forward Scattering (NFS) of synchrotron radiation is a technique related to the Mössbauer effect; thus, similar microscopic information to that inferred from conventional Mössbauer spectroscopy can be obtained. One can measure the shifts and splittings of the energy levels which are caused by the hyperfine interaction of the nuclear moments with electric charge distributions and magnetic moments of the investigated sample. In this way, both electronic and magnetic properties of a given system can be investigated. The NFS technique is very efficient for high pressure experiments performed on very small diameter (200 μm) in a DAC due to the very high intensity and excellent collimation of SR.

In a NFS experiment the time dependence of the nuclear de-excitation following the excitation by an x-ray is studied. The half life $T_{1/2}$ of the first excited state of nuclei is typically of the order of some ns to some μs (for example $T_{1/2} = 10$ ns for ^{151}Eu). Consequently, the time interval between synchrotron pulses should be longer or comparable to $T_{1/2}$. For this purpose, the ESRF provides a special "16-bunch mode", with 16 equally spaced bunches per revolution period. Then the SR pulses are emitted in intervals of 176 ns. Thanks to this pulsed time structure of the synchrotron radiation, the time-resolved detection of the γ quanta of the nuclear de-excitation is possible by discriminating this "delayed" radiation from the "prompt" electronic scattering, which occurs almost instantaneously within the SR pulses of 100 ps (see Figure 3.13).
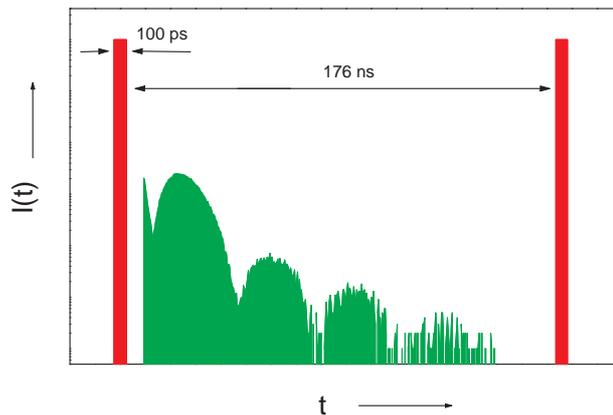
Figure 3.13: Time structure of the 16-bunch mode at ESRF. Between two SR pulses (vertical lines) is a time window of about 176 ns which can be used for the detection of the delayed photons of nuclear scattering processes.

After the ^{151}Eu nuclei in the sample are excited resonantly by a SR pulse, they decay back to the ground state. The radiation in the forward direction is emitted coherently by the nuclei, and the detector measures the decay curve I(t) and stores the data in a multichannel analyzer as a function I of time from the excitation by the SR pulse. From the shape of the I(t) curve the hyperfine interaction parameters can be determined.

(a)

excited state

ground state ω_0

no hyperfine interactions

I(t)

$$I \sim e^{-\alpha t}$$

α: decay constant

t

radiative decay

(b)

excited state ω_2

ω_1

ground state

hyperfine interactions

I(t)

$$I \sim e^{-\alpha t} \cos^2(\Delta\omega t)$$

$\Delta\omega = \omega_2 - \omega_1$

t
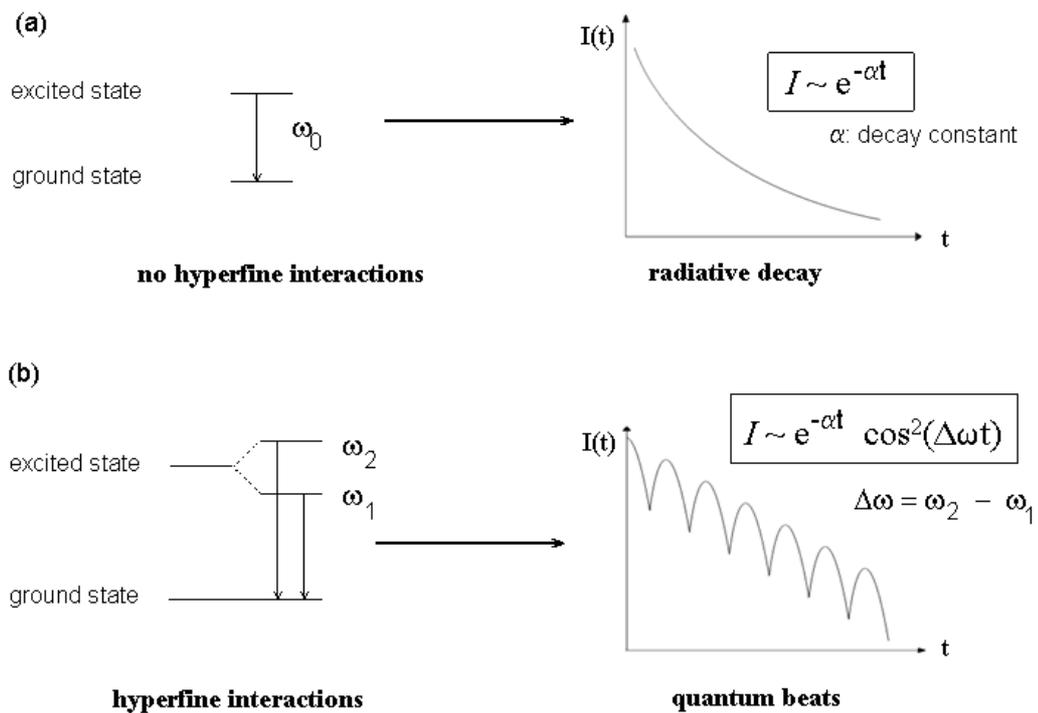
quantum beats

Figure 3.14: Schematic presentation of the NFS spectra in the absence (a) and presence (b) of hyperfine interactions. Quantum beats appear as oscillations in the time dependent spectrum.

As shown in Figure 3.14, the I(t) curve exhibits in the presence of hyperfine interactions periodical oscillations which are called *quantum beats*. The period of these beats is inversely proportional to the strength of the hyperfine interactions at the ^{151}Eu nuclei, and it therefore allows one to follow their evolution with temperature and/or pressure.

The setup for the ^{151}Eu studies is shown in Figure 3.15. The beam delivered by the undulator is first premonochromatized by a high heat-load monochromator using a

double Si(1 1 1) reflection, which provides an energy bandwidth of about 2.8 eV at 21.542 keV [77]. The resulting radiation is further monochromatized in a second step by a high-resolution monochromator to a bandwidth of about 1.3 meV. The beam is successively focused to a size of about 150×150 μm^2, passes the sample in the DAC and arrives at the detector system, where the photons of the prompt electronic scattering and of the delayed nuclear scattering from the sample will be recorded by a fast avalanche photodiode. For the temperature dependence we used a cryostat with a superconducting solenoid which delivered simultaneously low temperatures.
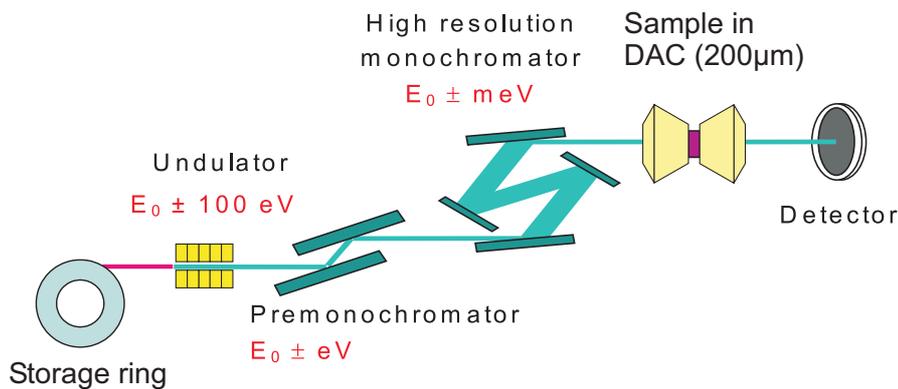
Figure 3.15: Typical experimental setup for nuclear NFS experiments. The incident SR beam comes from the left hand side.

3.2.6   High resolution neutron diffraction

The time-of flight powder diffraction data were collected at the high resolution powder diffractometer (HRPD) of beamline S8, at ISIS (Rutherford Appleton Laboratory, England). The time-of-flight diffractometer, such as the HRPD, utilises a polychromatic neutron beam and therefore data were recorded by fixed-angle detectors (engery dispersive). The neutron wavelengths were discriminated by their time of arrival since $t \propto 1/v_n \propto \lambda_n \propto d$, where t is the the time of flight, v_n is the neutron velocity, λ_n is the neutron wavelength and d is the $d-$spacing of a particular Bragg reflection. The HRPD offers three detector arrays at backscattering $\langle 2\theta \rangle$ = 168°, 90° and 30°. For constrained sample environments, such the present case with a high pressure cell, 90° scattering is optimal since with suitable collimation a diffraction data may be obtained without contamination from the cell components (see Figure 3.16). For the present experiment recorded using the 90° detectors, the time-of-flight ranges used was 15 to 115 ms corresponding to a d-spacing range of between $\approx$ 0.43 to 3.33 Å and wavelength range λ = 0.61 to 4.71 Å. Under these experimental settings the diffraction data have an approximately constant resolution of $\Delta d/d = 2 \cdot 10^{-3}$.
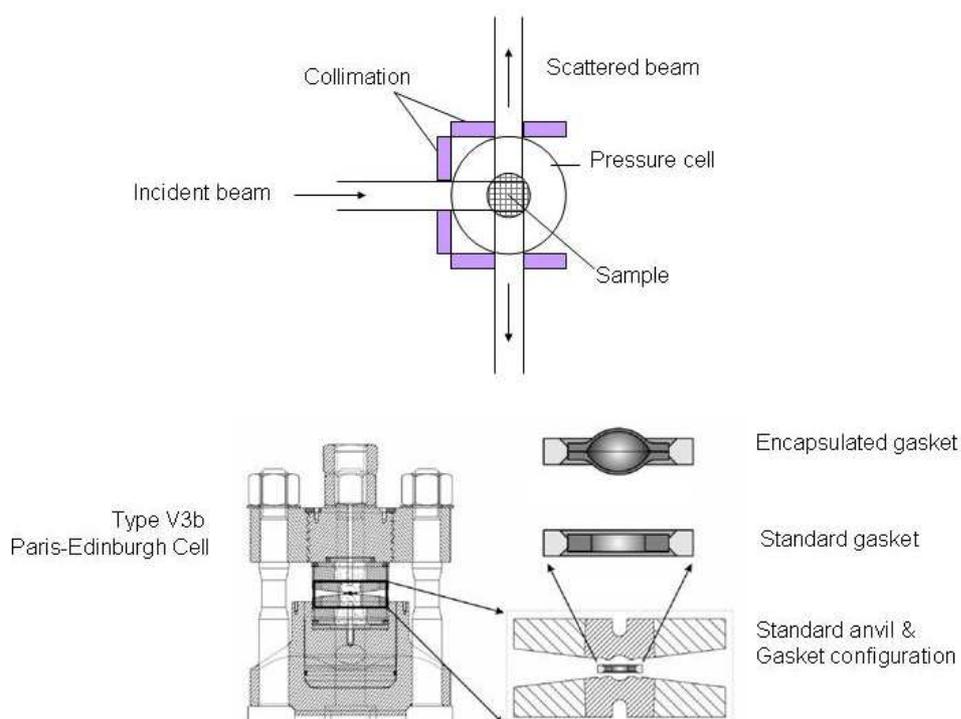
Figure 3.16: Above: Experimental setup of the HRPD. The incident neutron beam comes from the left-hand side. Below: Schematic sketch of the Paris-Edinburgh high pressure cell and the used encapsulated gasket.

The pressure cell used for the experiment is shown on the bottom of Figure 3.16. It is a so-called Paris-Edinburgh high pressure cell in which a powder sample is compressed between two opposite tungsten carbide anvils. The confinement of the sample was achieved by means of null-scattering (TiZr-alloy) gasket which was located between the anvils. Instead of a standard gasket, we used a modified designed gasket, consisting of two flanged hemispherical shells enclosing the sample. This encapsulated gasket (see Figure 3.16 bottom right) fits perfectly in corresponding grooves of the anvils. A detailed description of this cell can be found in Ref. [78]. The pressure transmitting media inside the capsule was a 4:1 mixture of methanol-ethanol. Pressure was applied by an in-situ hydraulic ram, whereas the pressure was determined by the pressure dependence of the lattice parameters as well as of the volume of $LuNiO_3$ from Ref. [79].

Chapter 4

High pressure studies on $RNiO_3$

4.1 Basic properties of $RNiO_3$ at ambient pressure

4.1.1 Structural aspects

According to chemical literature of crystallography [80], the series of rare-earth nickelates ($RNiO_3$) crystallize in an orthorhombically distorted perovskite structure. The aristotype of this structural family is the mineral $CaTiO_3$, whose general chemical formula can be written as AMX_3 and which shows a perfect perovskite structure above 900°C, see Figure 4.1. AMX_3 compounds consists of corner-shared MX_6 octahedra (M = cation), located at the edges of a simple cubic lattice and with a larger A cation in the body centre of the unit cell. This A cation will fit perfectly inside this ideal perovskite structure if the condition $d_{A-X} = d_{M-X} \cdot \sqrt{2}$ is satisfied, where d means the bond length between two ions. To assure electrical neutrality the X atom is an anion which is the oxygen in the $RNiO_3$ series.
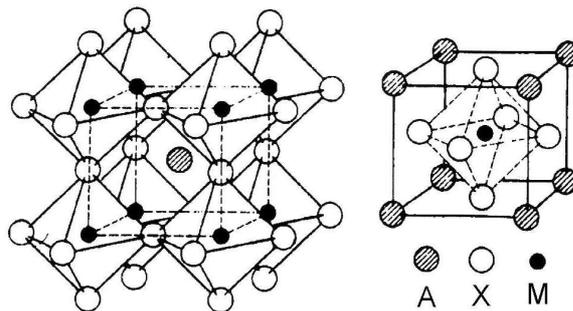
Figure 4.1: Two different views of the ideal cubic AMX_3 perovskite structure.

In the $RNiO_3$ series[1] the criterion for a perfect perovskite structure is not satisfied

---

[1]R = rare earth ions: La,..., Lu and Y.

since the A cation in the centre is too small. As a result, the NiO_6 octahedra, which have been found to remain practically undistorted along the series, are tilted to fill extra interstitial space. These rotations cause the unit cell to be smaller and more distorted than the ideal cubic cell. From geometry it is possible to derive a relation of distortion between the relative distances $d_{M-X} = d_{Ni-O}$ and $d_{A-X} = d_{R-O}$. This can be discussed in terms of the *tolerance factor* t [81] which is defined as

$$t \equiv \frac{d_{A-X}}{\sqrt{2} \cdot d_{M-X}} \tag{4.1}$$
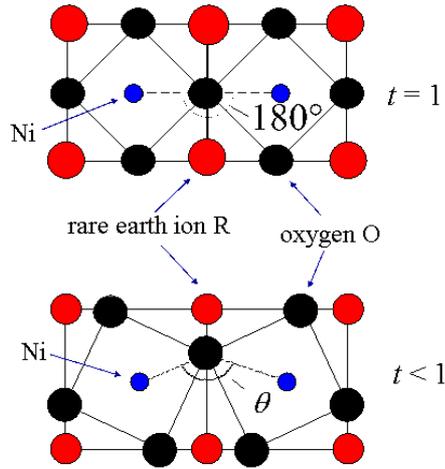
Figure 4.2: Schematic view of the distortion of a perovskite structure. The t is the tolerance factor defined in the text and θ the Ni-O-Ni bond angle.

It can be calculated from the equilibrium (A-X) and (M-X) bond lengths for ambient conditions from the sums of the ionic radii which are listed in tables [23] from x-ray data at room-temperature and ambient pressure. Experimentally, it is observed that when t is slightly less than 1 unity, the NiO_6 octahedra are rotated around the (1 1 1) cubic axis (see Figure 4.2) [82]. Is t even smaller, than a tilt of the octahedra around the (1 1 0) and (0 0 1) cubic axes is observed which results in the orthorhombic $GdFeO_3$-structure [83] and for much smaller $t < 0.7$ other, non-perovskite structures are preferred [80].

Figure 4.3 shows the variation of the lattice parameters as a function of the tolerance factor. One can deduce from this picture, that the orthorhombic distortion, which becomes even more important with decreasing R^{3+} radius, is stable from $t \approx 0.932$ (Lu) to $t \approx 0.975$ (Pr). For $LaNiO_3$ the high value of $t = 0.986$ allows to stabilize the less distorted rhombohedral structure. The boundary between these two phases has been localized at $t = 0.980$ [85].
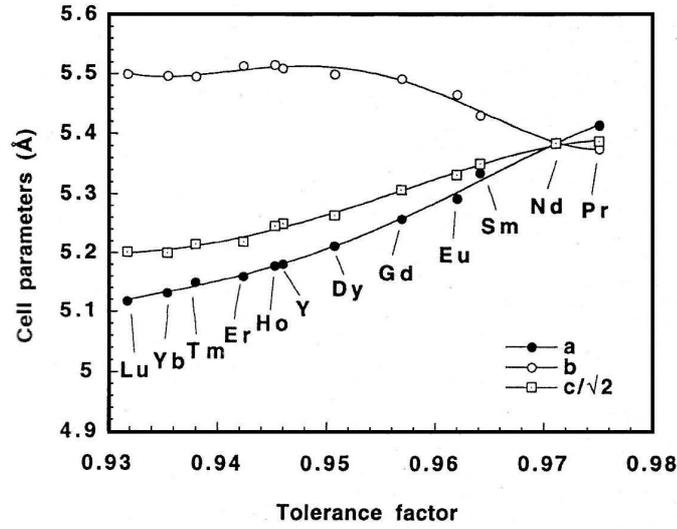
Figure 4.3: Variation of lattice parameters as a function of the tolerance factor t in the RNiO$_3$ series. The value of t have been calculated by using a constant distance of d_{Ni-O} for all nickelates and the R-O distances given in [84] for trivalent rare earth ions in coordination 12.

An interesting trend in the whole series of nickelates is the practical invariance of the average Ni-O distance. Thus, the NiO$_6$ octahedra can approximately be seen as rigid bodies.

For AMX$_3$ perovskites with *Pbnm* orthorhombic symmetry the volume V can be described in the following way:

$$V = abc = 32 \cdot l^3 \cos^2 \phi \tag{4.2}$$

where a, b, c are the unit-cell lattice parameters, l the bond length M-X, and ϕ is the angle of rotation of the octahedra about the threefold axis [86]. It is important to distinguish the *angle of rotation* ϕ from the *tilting angle* ω of the MX$_6$ octahedra.

Usually, ω is defined as

$$\omega = \frac{\pi - \theta}{2} \tag{4.3}$$

with θ being the M-X-M superexchange angle or *bond angle*. Thus, two distinct values of θ can be defined for *Pbnm* symmetry: $\theta_1 = $ M-X$_1$-M and $\theta_2 = $ M-X$_2$-M with X$_1$ and X$_2$ being the anions occupying the 2 apical and 4 basal positions of the MX$_6$ octahedra, respectively. For RNiO$_3$ perovskites (R = Pr, Nd), θ_1 and θ_2 differ only in a few tenth of degree [7]. As a result, one often talks about an average bond

angle

$$\theta \equiv \langle\theta\rangle = \frac{(\theta_1 + 2\theta_2)}{3} \qquad (4.4)$$

and an average tilting angle

$$\omega \equiv \langle\omega\rangle = \frac{(\pi - \langle\theta\rangle)}{2}. \qquad (4.5)$$

A useful schematic draw of the *Pbnm* symmetry, with the important angles $\phi, \theta_1, \theta_2, \omega_1$ and ω_2 is given in Figure 4.4.
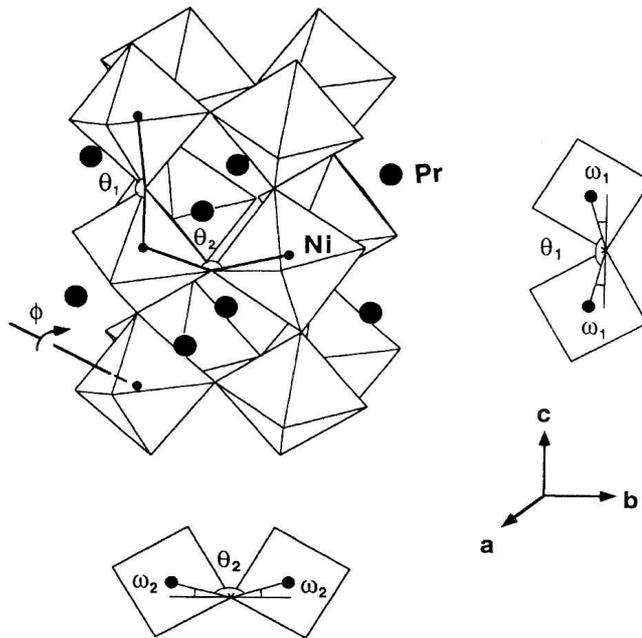
Figure 4.4: Schematic sketch of the distorted *Pbnm* perovskite structure showing the $\phi, \theta_1, \theta_2, \omega_1$ and ω_2 angles; taken from [87].

Alternatively, the structural parameters of AMX$_3$ in the setting of a *Pnma* symmetry can be expressed in terms of the $\langle$M-X$\rangle$ bond length l and the angle of rotation ϕ about the three-fold axes [88]:

$$a = l\{8(2 + \cos^2 \phi)/3\}^{1/2}; \quad b = l\{48/(1 + 2\sec^2 \phi)\}^{1/2}; \quad c = l\sqrt{8}\cos \phi. \qquad (4.6)$$

The tilting angle ϕ can be deduced from the volume (4.2) and the lattice parameters by

$$\phi = \arccos\left(\sqrt{\frac{V}{32l^3}}\right) = \arccos\left(\frac{\sqrt{2}c^2}{ab}\right). \tag{4.7}$$

The connection to the angles ω_1 and ω_2 is then given by

$$\cos\omega_1 = \sqrt{\frac{3\cos^2\phi}{(2+\cos^2\phi)}} \tag{4.8}$$

and

$$\cos\omega_2 = \sqrt{\frac{l + 2\cos^2\phi}{3}}. \tag{4.9}$$

With some geometrical derivatives, one obtains for θ following useful expression [89]:

$$\theta = \pi - 2\omega = \pi - 2\arccos(a^2\sqrt{2}/bc). \tag{4.10}$$

4.1.2   Electronic properties

The RNiO$_3$ family provides an interesting window to study the evolution of electronic features of oxides which show metallic conductivity. One reason why they are so exciting to study is their perfect oxygen stoichiometry which allows to discover electronic changes, such as the MI transition, very easily in contrast to the family of cuprates or manganites where the non-stoichiometry is the basic tool to achieve physical properties like superconductivity or giant-magnetoresistance.

The nominal valence of Ni ($3d^7$) in RNiO$_3$ is 3+ with d-electron configuration t_{2g}^6 e_g^1 and $S = 1/2$ (LS) as ground state. Like e.g. Mn^{3+} in LaMnO$_3$ ($3d^4$), Ni^{3+} in RNiO$_3$ is Jahn-Teller active too, but there has been observed no measurable influence on the properties of RNiO$_3$ as in comparison in the manganite compounds [90]. The NiO$_6$ octahedra seems to be very regular in the whole RNiO$_3$ family [9, 91].

Except LaNiO$_3$ which has the largest one-electron bandwidth and is metallic down to low temperatures, the whole series of RNiO$_3$ has an insulating ground state, i.e. they have a small charge-transfer gap between O-$2p$ and the Ni-$3d$ upper Hubbard band and can be regarded as a self-doped Mott-insulator [92, 93, 94]. RNiO$_3$ exhibits a thermally driven metal-insulator transition at T_{MI} and a further transition to a long-range antiferromagnetic order at $T_N \leq T_{MI}$. These latter two very interesting aspects will be discussed in detail in the subsequent sections. Here, we want to focus

firstable on the electronic ground state properties.

Deduced from x-ray absorption (XAS) and photoemission spectra on RNiO$_3$, the established image of a purely ionic ground state was suddenly uncertain. Due to the unusually high valency of Ni^{3+} a strong hybridization was discovered and used to describe a new realistic model for the ground state [95, 96, 97]:

$$|\Psi^G_{covalent}\rangle = \alpha|3d^7 2p^6\rangle + \beta|3d^8\underline{L}\rangle \qquad (4.11)$$

where $\underline{L}$ represents an anion (ligand) hole, $\alpha^2 + \beta^2 = 1$ and usually $\alpha > \beta$. The values of α and β in principle can be deduced from the x-ray spectra. At the O 1s K edge, and by allowing only intra-atomic XAS transition matrix elements, the intensity of the pre-peak is proportional to β^2 and it is a measure of the covalency in the ground state. Thus, the electronic structure of rare earth nickelates can be described by a mixture of their $3d^7 2p^6$ (Ni^{3+} O^{2-}) ionic character and a $3d^8\underline{L}$ (Ni^{2+} O$^-$) configuration including covalency, indicating a weight range between 30 and 70%.

Typical values for the energy gap (E_g) in RNiO$_3$ are $\lesssim 100$ meV ($\Delta < U$, with Δ the charge-transfer energy) and listed for some compounds in Table 2. In principal, these values are 1-2 orders in magnitude less than for typical Mott-Hubbard insulators or those reported for other Ni oxides e.g. NiO and La$_2$NiO$_4$ ($E_g \approx 4$ eV) [98]. Due to the strong hybridization it is therefore easy to induce either an insulating or metallic state just by changing the temperature.

Table 4.1: Thermal energies $k_B T_{MI}$ for RNiO$_3$ perovskites, taken from [90].

	$k_B T_{MI}$ (meV)
LaNiO$_3$	metallic
PrNiO$_3$	11.2
NdNiO$_3$	17.2
SmNiO$_3$	34.4
EuNiO$_3$	41.4

4.2   Temperature-induced metal-insulator transition

4.2.1   RNiO$_3$ phase diagram

The detailed behavior of the structural, electronic and magnetic phase transitions can be described best in the mapped out RNiO$_3$ phase diagram (Figure 4.5).
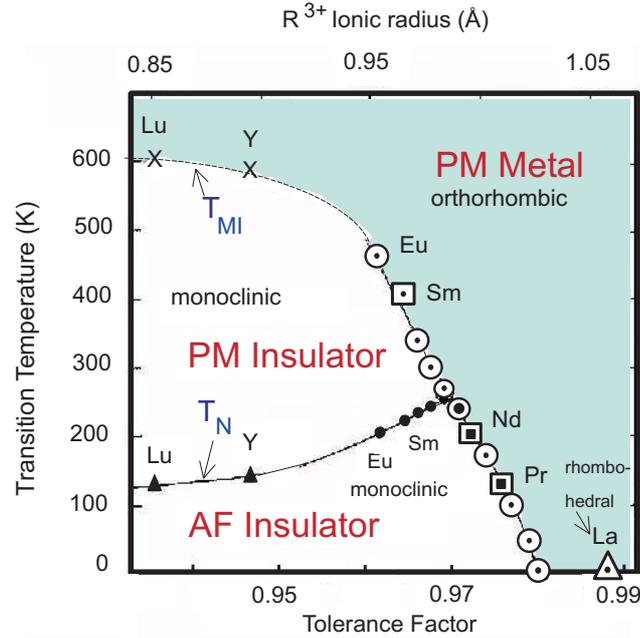
Figure 4.5: Modified phase diagram of the RNiO$_3$ series from [6]. Transition temperature as a function of the R^{3+} ionic radius and tolerance factor. The large open circles between LaNiO$_3$ and NdNiO$_3$ are different solid solutions of Nd$_{1-x}$La$_x$NiO$_3$, those between NdNiO$_3$ and SmNiO$_3$ are solid solutions of Sm$_{1-x}$Nd$_x$NiO$_3$. According to [92] and [101], the structure of NdNiO$_3$ below T_{MI} is monoclinic ($P2_1/n$).

The phase diagram shows the transition temperature as a function of the ionic size of the R^{3+} transition metal ions and the related tolerance factor t, which has been introduced in section 4.1.1.
In RNiO$_3$ with R = La, the largest rare earth ion, the system shows a Pauli paramagnetic metallic state down to lowest temperatures and crystallizes in a rhombohedral (R$\bar{3}c$) perovskite symmetry. By substitution of La with smaller R^{3+} ions (Pr → Lu),

the series immediately becomes insulating by opening of a small charge-transfer gap. Above the MI transition temperature (T_{MI}) all members of the RNiO$_3$ familiy (R $\neq$ La) crystallize in an orthorhombic (*Pbnm*) paramagnetic structure, which is symbolized by the blue color in the phase diagram.

Structural anomalies at the MI transition

For PrNiO$_3$ and NdNiO$_3$ the MI transition is accompanied by an antiferromagnetic (AF) ordering at T_N of the Ni sublattice, i.e. T_{MI} coincidence with T_N. For the smaller R^{3+} ions (Sm $\rightarrow$ Lu) they separate and T_N is always much lower than T_{MI} (e.g. SmNiO$_3$: T_{MI} = 400 K [85], T_N = 225 K [6], EuNiO$_3$: T_{MI} = 463 K [99], T_N = 205 K [6, 100], YNiO$_3$: T_{MI} = 582 K [101, 8], T_N = 138 K [101] and LuNiO$_3$: T_{MI} = 599 K [8], T_N = 130 K [89]), suggesting that the MI transition is not connected with the onset of AF ordering. Below T_N the system shows an AF insulating behavior, whereas above T_N one observes a Curie-Weiss-like paramagnetic behavior.

For R = Pr, Nd, Sm and Eu no change of the lattice symmetry (*Pbnm*) has been observed on going from the metallic to the insulating state. But there has been observed some subtle structural anomalies in the volume of the unit cell at the MI transition which results in a slight increase of the Ni-O bond length (Figure 4.6(a)) and a simultaneous decrease of the Ni-O-Ni bond angle θ (Figure 4.6(b)) [99, 7].
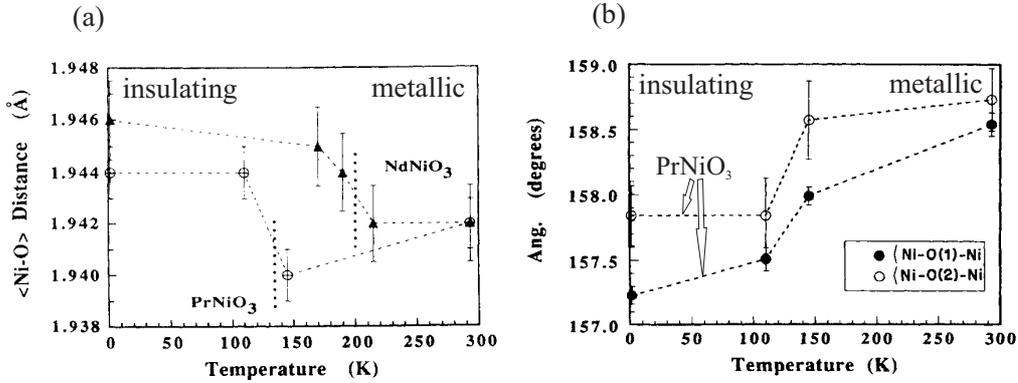
Figure 4.6: (a) Variation of the d_{Ni-O} bond lenght which shows the anomalies of the structure at the MI transition both for PrNiO$_3$ and NdNiO$_3$. Bold dotted lines show the MI transition. (b) Jump of the Ni-O-Ni bond angles at transition temperature T_{MI} in PrNiO$_3$ which govern the transfer integral between the Ni 3d and O 2p orbitals. Both figures taken from neutron measurements [7].

In fact, the value of T_{MI} has been found to be related to the steric effect induced by the size of the R^{3+} ion across the change of d_{Ni-O} and θ which determines the degree of overlapping of Ni(3d) and O(2p) orbitals and hence the electronic bandwidth.
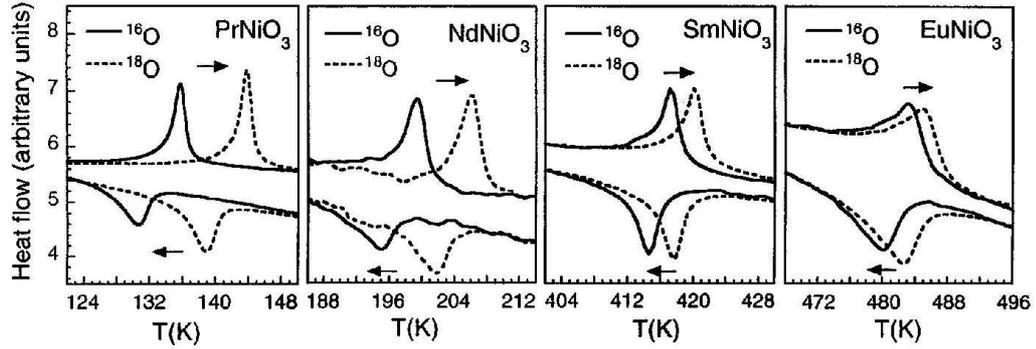
Figure 4.7: Differential scanning calorimetry (DSC) measurements across the metal-insulator transition recorded by heating and by cooling (see arrows) for the two series of nickelates (^{16}O and ^{18}O). The sharp maximum/minimum indicates the occurrence of the MI transition in all cases [102].

On the other hand, the observation of very large ^{16}O–^{18}O isotope shifts (see Figure 4.7) of T_{MI} in RNiO$_3$ (R = Pr, Nd, Sm and Eu) demonstrates the importance of a strong electron-lattice coupling in these systems [102]. This is also confirmed by neutron diffraction measurements on PrNiO$_3$ where a clear shift of T_{MI} has been found [102]. It should be mentioned, that the orthorhombic → rhombohedral structural phase transition observed at much higher temperatures is not affected at all by the mass of the oxygen isotope, thus indicating that the observed isotope shift is a specific feature of MI transition [102].

Lattice dynamics at the MI transition

To explain the evolution of ΔT_{MI} along the series, a simple model, based on the existence of Jahn-Teller polarons [103] has been used. The charge fluctuations in the metallic regime ($T > T_{MI}$) are expected to correspond to electron transfers between Ni and O sites (Ni^{3+}O^{2-} ↔ Ni^{2+}O$^-$). However, since Ni^{2+} ions are not Jahn-Teller active, Jahn-Teller polarons will appear as a consequence of the suppression of the Jahn-Teller distortion when an electron moves from an O^{2-} to a Ni^{3+}. Conduction electrons will then move through the lattice destroying the Jahn-Teller distortion at the Ni sites in a similar way as e_g electrons in Mn hole doped perovskites do. Hereby the main effect of Jahn-Teller polarons in the transport properties is to reduce the bandwidth. A reduction of the bandwidth W occurs by increasing the mass of the O isotope, which leads to a raise of T_{MI} and that is exactly that what is observed in Figure 4.7.

Structural phase transition and charge ordering

A different situation was found for RNiO$_3$ with much smaller R^{3+} ionic radius (R = Ho $\rightarrow$ Lu). X-ray and neutron diffraction measurements on HoNiO$_3$, YNiO$_3$, ErNiO$_3$ and LuNiO$_3$ show a clear change of the lattice parameters at T_{MI} [8]. They indicate a thermal induced structural phase transition from monoclinic ($P2_1/n$) to orthorhombic ($Pbnm$) (Figure 4.8).
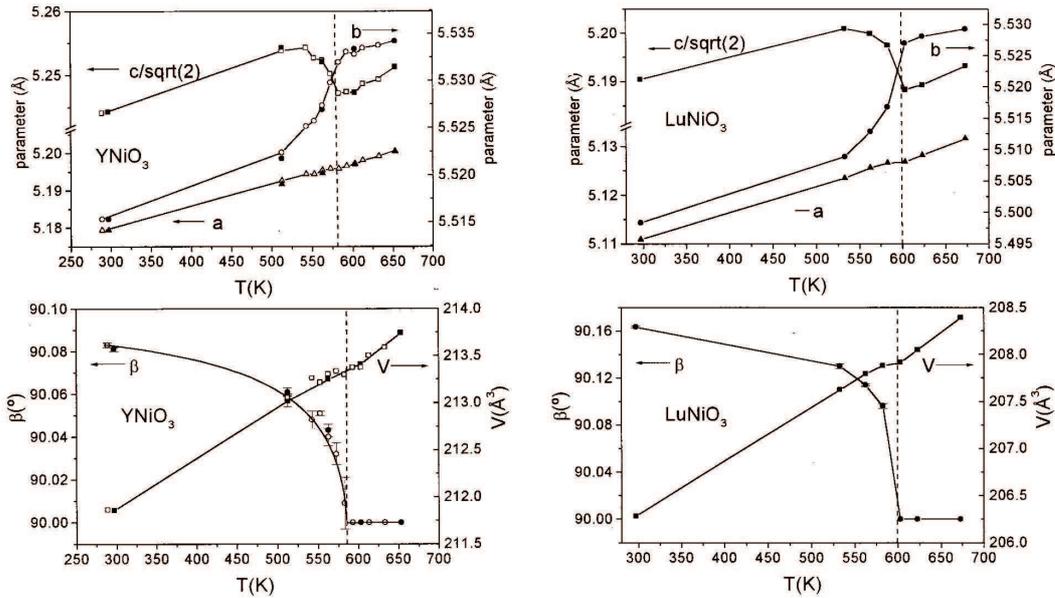
Figure 4.8: Structural parameters for YNiO$_3$ (left) and LuNiO$_3$ (right) as well as their related monoclinic angle β and unit cell volume V as a function of temperature. Measurements from high resolution neutron and angle resolved synchrotron x-ray powder diffraction [8].

The analysis of high resolution synchrotron powder diffraction measurements revealed that the strongly distorted members of the RNiO$_3$ series, e.g. YNiO$_3$ and LuNi$_3$, have a charge ordered ground state, which is also called **charge disproportionation** [9, 99, 104].

The interpretation of charge disporportionation in RNiO$_3$ is based on the observed symmetry lowering to monoclinic $P2_1/n$ crystal structure ($\beta = 90.08°$) in the insulating phase, which breaks up the single Ni site in the metallic phase into two non-equivalent crystallographic sites when the charge-transfer gap opens. One Ni1 octahedra with expanded Ni-O bond length (1.994(3) Å) and a Ni2 octahedra with contracted Ni-O bonds (1.923(3) Å), respectively. Figure 4.9 presents the octahedral oxygen coordination around the Ni1 and Ni2 atoms. They signal two different charge states which alternate around the three crystallographic axes. The most remark-
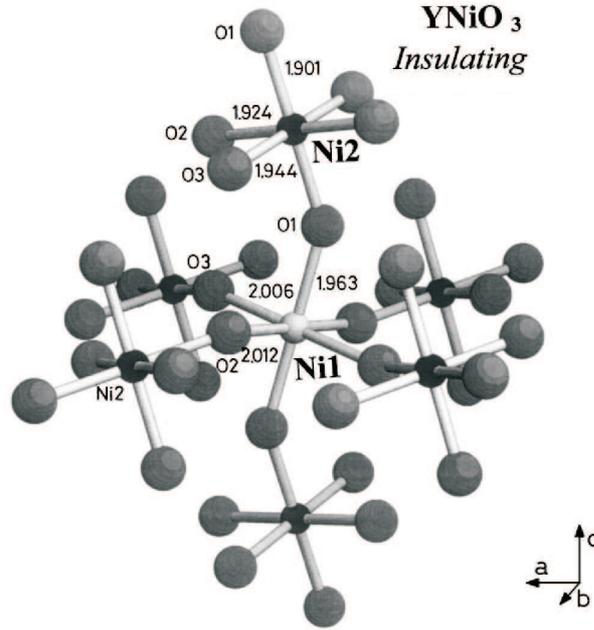
Figure 4.9: Oxygen coordination for Ni1 and Ni2 in monoclinic (insulating phase) YNiO$_3$ measured by neutron diffraction spectroscopy [9]. Each Ni1O$_6$ shares corners with six Ni2O$_6$ octahedra, and vice versa.

able finding is that the monoclinic symmetry is a consequence of very significant differences in the average size of both kind of octahedra.

Based on the fact of these two distinct octahedra, Alonso et al. [9] suggested a Ni^{3+} charge disproportionation as following: Ni$^{3+\delta}$ + Ni$^{3-\delta'}$ $\rightarrow$ 2Ni^{3+}, with $\delta \approx 0.3$e$^-$, where $|\delta| \approx |\delta'|$.

An evidence for a charge ordered state in the insulating phase in RNiO$_3$ compounds with larger lanthanides (Dy $\rightarrow$ Pr) has recently presented by de la Cruz et al. by phonon spectroscopy [101] and Staub et al. by resonant x-ray scattering on an epitaxial thin film of NdNiO$_3$ [92]. As a result, de la Cruz et al. observed in infrared transmission and reflectivity measurements on NdNiO$_3$, SmNiO$_3$, EuNiO$_3$, HoNiO$_3$ and YNiO$_3$ between 77 and 700 K, that below T_{MI} a lower symmetry than orthorhombic lattice distortion has taken place and again the signature of the monoclinic distortion has been found. Their measurements clearly show a disappearing of phonon frequencies above T_{MI} which are associated with a structural phase transition.

In Figure 4.10 the nickelate phonon bands at 77 K are shown as a function of the R^{3+} radius, sequencing the degree of structural distortion. As to see, the octahedral breathing modes at ~ 600 cm^{-1} are the vibrations that are being more affected by the octahedral tilting and shape, i.e. the O(2p)-Ni(3d) hybridization. With increasing
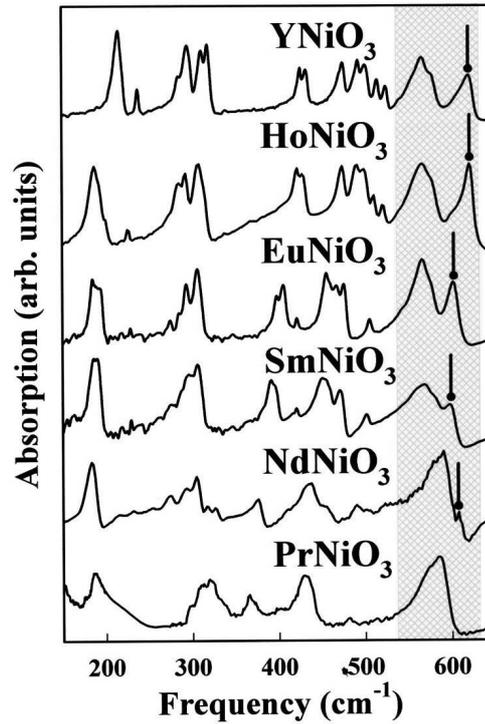
Figure 4.10: Lattice absorption spectra of different RNiO$_3$ at 77 K [101]. The arrow at
~ 600 cm^{-1} indicates the splitting of the phonon band which is related to a
monoclinic structure that correlates well with charge disproportionation as
a more subtle monoclinic distortion in RNiO$_3$ with large R^{3+} ionic radius.

R^{3+} ionic radius this peak becomes smaller and vanishes apparently for PrNiO$_3$. But
also in PrNiO$_3$ (where only a main band asymmetry and not an explicit phonon
splitting has been observed) charge ordering is in accordance with the measurements
of Piamonteze et al. [105, 106, 107].

Furthermore, Staub et al. recently observed charge ordering at the metal insulator
transition in NdNiO$_3$ epitactical films by using resonant x-ray scattering. They
report that the MI phase transition is associated with structural and vibrational
changes at T_{MI} described by a *Pbnm* to *P2$_1$/n* lattice phase transition. Their
findings show that the MI transition in NdNiO$_3$ can be understood on the basis of
charge order [92].

In conclusion, many recent publications suggest that the whole series of RNiO$_3$ (R
$\neq$ La) share a common triggering mechanism of the temperature-induced MI phase
transition, which is related to octahedral tilting and distortion. They support the
idea that charge order may occur in all RNiO$_3$ [92, 108].

Magnetic properties and magnetic structure of RNiO₃:

For LaNiO$_3$ neither susceptibility nor neutron diffraction measurements found magnetic ordering down to lowest temperatures. The temperature dependence of the magnetic susceptiblity was found to be consistent with a Pauli paramagnetic behavior. Magnetic susceptibility measurements on other RNiO$_3$ compounds (R $\neq$ La) found a Curie-Weiss behavior and a sudden increase of χ^{-1} which was interpreted as the onset of cooperative ordering of the Ni magnetic moments.

In fact, all RNiO$_3$ with R $\neq$ La, show above the magnetic ordering temperature (T_N) a paramagnetic behavior, whereas below T_N an unusual magnetic ordering with a propagation vector $\mathbf{k} = (\frac{1}{2}, 0, \frac{1}{2})$ with respect to the orthorhombic unit cell was determined [7, 100, 90]. This corresponds to an up-up-down-down stacking of ferromagnetic planes along the pseudocubic [111] direction. As the twofold degenerate orbital e_g is singly occupied, one may expect a significant Jahn-Teller distortion and associated orbital ordering in the insulating state of the RNiO$_3$ compounds [100]. Such a formation of an orbital superlattice could indeed explain the unusual magnetic ordering. However, thus far, no evidence for a Jahn-Teller distortion has been found. Moreover, it was argued that the orbital ordered state has a relatively high energy, suggesting that it is not responsible for the magnetic structure [109, 110].
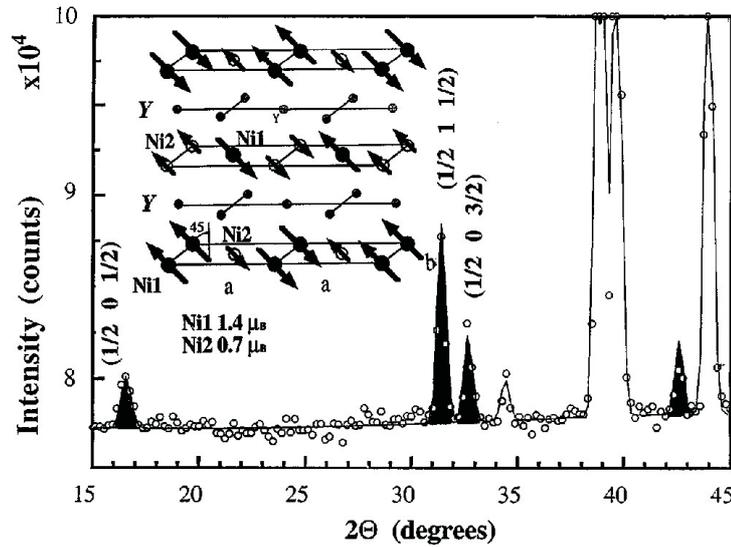
Figure 4.11: Detail of the main magnetic reflections (shadowed) refined at 1.5 K. Inset: Type of magnetic ordering described in the text [9].

Figure 4.11 depicts the main magnetic reflections of YNiO$_3$ at 1.5 K [9]. The magnetic moments are situated in the ac plane, deviated around $45°(\pm\ 10°)$ from the z-axis. As a result of this fit, one obtains two unequal moment values of 1.4(1) μ_B

and 0.7(1) μ_B for Ni1 and Ni2, respectively [9]. This implies an accumulation of extra electrons at the Ni1 site at expenses of inducing charge defects at the adjacent Ni2 sites. This suggests that the observed charges (Ni1: 3 - δ) and (Ni2: 3 + δ) in YNiO$_3$ correspond to $\delta \cong 0.35$.

As a result, the data provide evidence for the stabilization of an uncompleted charge disproportionation, $2\text{Ni}^{3+} \rightarrow \text{Ni}^{2+}$ ($S = 1$) + Ni^{4+} ($S = 0$), which is associated with the MI transition. Altogether, these findings represent an important advance for the understanding of the charge localization in transition metal oxides with orbitally degenerated electrons.

4.3   Previous high pressure work on RNiO$_3$

In the following we briefly summarize previous high pressure results on RNiO$_3$.

$R(p, T)$ on PrNiO$_3$ and NdNiO$_3$:

The first measurements of the electrical resistivity under high pressure of RNiO$_3$ have been performed by Obradors [111] and Canfield [112] on PrNiO$_3$ and NdNiO$_3$ in the early 90th, showing a sharp pressure-induced MI transition above 1.3 GPa for PrNiO$_3$ and at 2.5 GPa for NdNiO$_3$ under linear approximation [112], see Figure 4.12(a,b). They report of a strong shift of T_{MI} with increasing pressure up to 1.5 GPa at a rate of $\partial T_{MI}/\partial p = -42$ K/GPa and -76 K/GPa, whereas this rate is for the same compounds, see Figure 4.12(c). This discrepancy is related to different cooling and rating rates used in both cases [87]. Whereas Obradors et al. report of a linear dependence of $T_{MI}(p)$, Canfield's data fit better to an approximately quadratic
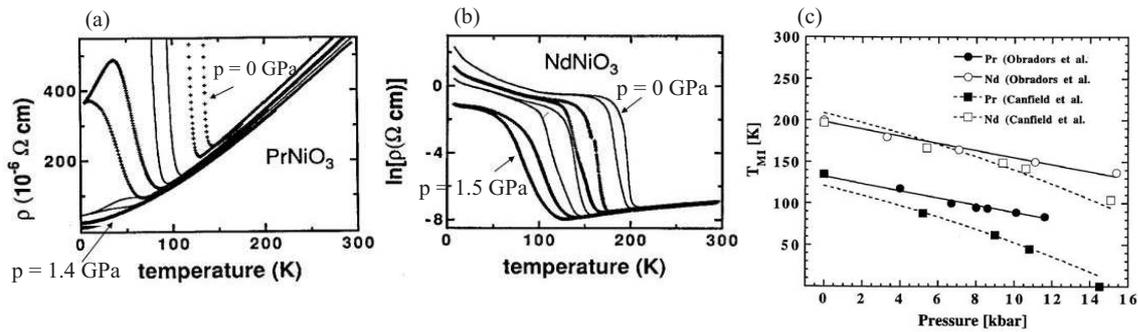
Figure 4.12: Pressure dependence of $\rho(T)$ for (a) PrNiO$_3$ and (b) NdNiO$_3$ for $0 \leq p \leq$ 1.5 GPa. With increasing pressure the MI transition shifts to lower temperatures. (c) T_{MI} as a function of pressure in PrNiO$_3$ and NdNiO$_3$. Both taken from [112, 111].

function. Both are the opinion, that $\partial T_{MI}/\partial p$ appears to be the same for PrNiO$_3$ and NdNiO$_3$. This means that a common structural parameter is controlling the development of $T_{MI}(p)$. In the author's point of view, this is related to the Ni-O-Ni bond angle θ.

Furthermore, strong hysteresis in the resistance was found, varying the temperature across the first-order MI transition. Moreover, reentrant metallic and thermal history effects were observed in transport measurements due to incomplete relaxation processes [112, 111, 87].

Neutrons and x-ray diffraction measurements of the structural parameters on RNiO$_3$ under pressure:

The investigation of the crystal structure by neutron diffraction on PrNiO$_3$ under pressure up to 0.5 GPa exhibited that the main structural changes consist of a small diminution of the Ni-O bond length (d_{Ni-O}) and the simultaneous increase of the Ni-O-Ni bond angle (θ), see Figure 4.13(a,b) [87].

Moreover, the authors show, that the symmetry of the unit cell in PrNiO$_3$ and NdNiO$_3$ changes from $Pbnm$ to $R\bar{3}c$ above 4 GPa. The evolution of the structure under external pressure is then qualitatively similar to the observations made by substitution of rare earth ions with different ionic radius (chemical pressure). This leads to a less distorted framework together with an enhanced metallic conductivity.
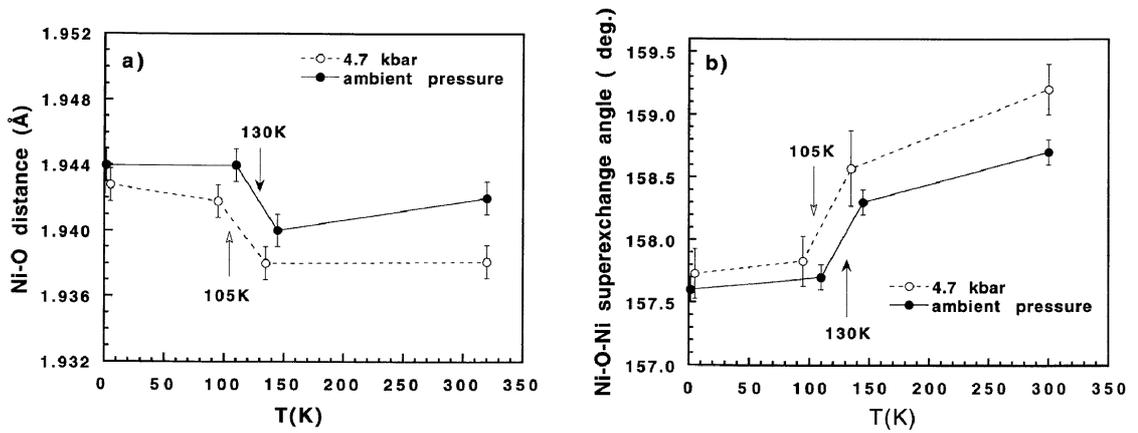
Figure 4.13: Pressure dependence of (a) the average Ni-O distance d_{Ni-O} and (b) the Ni-O-Ni bond angle θ of PrNiO$_3$ as a function of temperature at ambient pressure and 0.47 GPa. The dotted lines are guide to the eye [87].

A structural phase transition (orthorhombic $\rightarrow$ rhombohedral) has also been observed by Amboage [79] by angle-resolved x-ray diffraction measurements but at p

$= 11$ and 6 GPa for NdNiO$_3$ and PrNiO$_3$, respectively.

Certain structural anomalies in the lattice parameter have also been observed in SmNiO$_3$ [113] by means of x-ray powder diffraction measurements with angle-resolved synchrotron radiation. They found that around 2.5 GPa the cell parameter b undergoes a small abrupt contraction (see Figure 4.14 and inset) which in the authors sense is related to the beginning of the expected pressure-induced metallization at room-temperature [113]. Together with this contraction, they found a strong in-
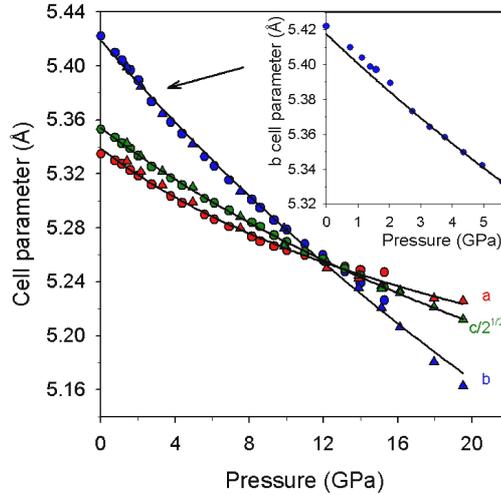
Figure 4.14: Pressure dependence of the SmNiO$_3$ lattice parameters. The inset shows a zoomed view of the b lattice parameter as a function of pressure [113].

crease of the Ni-O-Ni bond angle θ with increasing pressure. θ enlarges from $153.4°$ at ambient pressure about $3°$ to more than $156°$ at 3 GPa. Furthermore, they observed a structural phase transition from the orthorhombic ($Pbnm$) to the less distorted rhombohedral ($R\bar{3}c$) perovskite structure for $p \geq 26$ GPa [113].
In constrast to the observations made on the large RNiO$_3$ coumpounds (R = Pr, Nd and Sm), angle resolved high resolution x-ray diffraction measurements on the smaller RNiO$_3$ compounds (R = Lu and Y) brought no indication for such a small anomaly of the local structure under pressure. Instead of this (see Figure 4.15(a)), LuNiO$_3$ undergoes a real structural phase transition (monoclinic ($P2_1/n$) $\rightarrow$ orthorhombic ($Pbnm$)) at $p \geq 16$ GPa which can be seen best in the c lattice parameter [79]. Similar observations have also been made for YNiO$_3$ (Figure 4.15(b)). The a-cell parameter shows no appreciable change through the phase transition. The behavior of the b- and c-parameters is different: they undergo an abrupt change through the transition, b expanding and c contracting. Here the structural phase transition (monoclinic $\rightarrow$ orthorhombic) could already be found at 14 GPa [108].
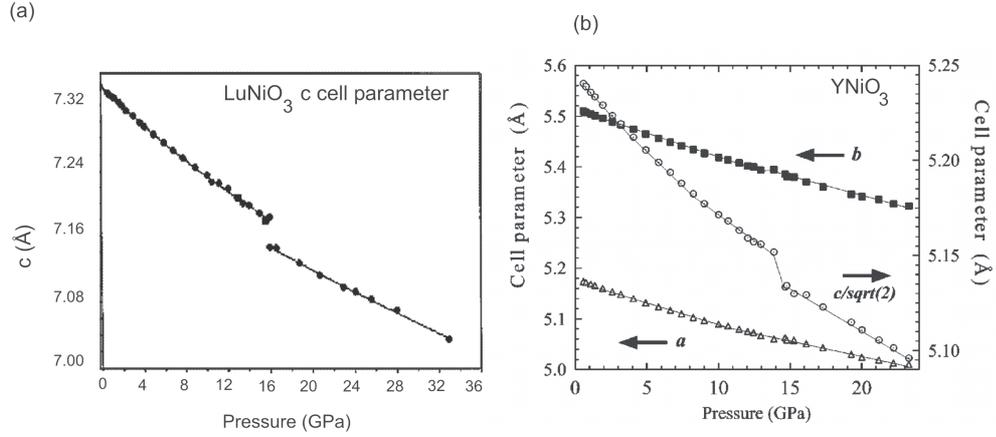
Figure 4.15: Pressure dependence of (a) the c-lattice parameter in LuNiO$_3$ [79] and (b) of the a, b, c-lattice parameters in YNiO$_3$ [108]. The change of the structural phase transition in LuNiO$_3$ and YNiO$_3$ can be best viewed in the c-cell parameter.

4.4   Motivation for high pressure studies on RNiO$_3$

As mentioned before, the temperature-induced MI transition in RNiO$_3$ series is connected with structural changes and simultaneous charge ordering. However, a common physical picture for the driving mechanism of the thermally-induced MI transition is still far from being fully understood.

As it was shown in NdNiO$_3$ and PrNiO$_3$, external pressure was able to suppress the transition temperature T_{MI} of the MI transition, stabilizing the metallic state to lowest temperatures [111, 112]. Thus, a promising approach for a better understanding of the driving mechanism of the MI transition is to investigate the effect of pressure on the transport, magnetic and structural properties of RNiO$_3$ with smaller R, i.e. R = Sm,..., Lu. Such a study allows one to explore the following interesting aspects:

(i) the pressure-induced insulator metal (IM) transition and its possible connection with the structural phase transition and in particular charge ordering; both are observed at the temperature-induced MI transition.

(ii) The crossover from antiferromagnetic insulator to a nonmagnetic metal through a quantum critical point (QCP) (see Figure 4.16, where the sample under investigation (R = Sm,.., Lu) are located at different distances from the QCP. Here, the central issue is whether the expected metallic state at high pressure is magnetic or nonmagnetic. And the next question will be what is the nature of ground state near the QCP?
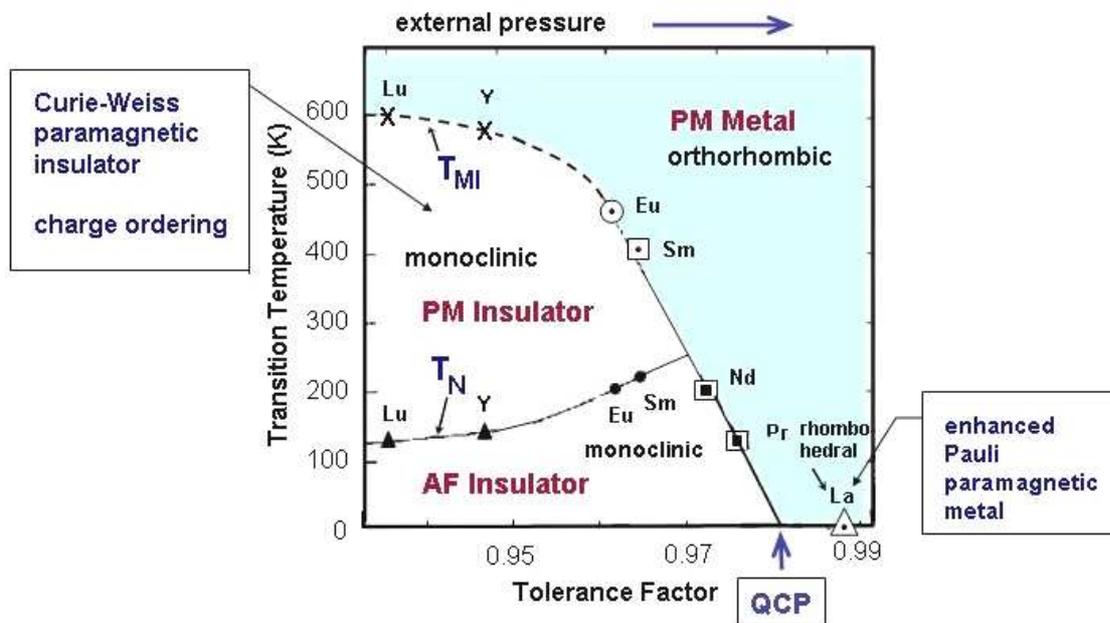
Figure 4.16: RNiO$_3$ phase diagram with the investigated samples under high pressure.

To give an answer to the above given questions, we have investigated the transport, magnetic and structural properties of selected RNiO$_3$ compounds (R = Sm, Eu, Y and Lu) under high pressure using different experimental methods. We mainly have used the electrical resistance to account for the occurrence of the pressure-induced insulator metal (IM) transition in all RNiO$_3$ samples, while x-ray diffraction and ^{151}Eu nuclear forward scattering of synchrotron radiation were used for structural and magnetical studies in EuNiO$_3$, respectively. In the case of LuNiO$_3$ we have performed magnetization as well as high resolution neutron diffraction experiments.

4.5 Experimental Results on RNiO$_3$

This chapter presents the experimental results performed on the selected rare earth nickelate compounds. For simplicity, we treat the results obtained from our measurements on RNiO$_3$ compounds in two categories, according to the size of their ionic radius: (a) LuNiO$_3$ and YNiO$_3$ represent the smaller rare earth nickelates and (b) EuNiO$_3$ and SmNiO$_3$ represent those with larger rare earth ions which are closer to the crossover localized–itinerant.

All RNiO$_3$ samples used in this thesis were prepared by Dr. J. A. Alonso et al. (Instituto de Ciencia de Materiales de Madrid, CSIC, Cantoblanco, Madrid, Spain) by solid state reactions as polycrystalline powders. Their preparation is described elsewhere [99].

The first part of this section is dedicated to the electrical resistance measurements under high pressure. Then we consider the structural stability of the selected compounds under high pressure and discuss possible mechanisms for the pressure-induced insulator to metal (IM) transition in the large and small RNiO$_3$.

Subsequently, we present and discuss our investigation of the effect of pressure on T_N in selected samples as obtained from electrical resistivity, magnetization and nuclear forward scattering measurements under high pressure. Finally we discuss the magnetic phase diagram of LuNiO$_3$ and EuNiO$_3$.

4.5.1 The pressure-induced insulator metal transition

4.5.1.1 Electrical resistivity measurements on LuNiO$_3$ and YNiO$_3$:

At room-temperature LuNiO$_3$ and YNiO$_3$ are paramagnetic insulators with an antiferromagnetic ordering temperature of $T_N = 130$ and 138 K and a MI transition temperature of $T_{MI} = 599$ and 582 K at ambient pressure, respectively. In the whole series of RNiO$_3$ perovskites, LuNiO$_3$ is the most distorted one, since it has the smallest ionic radius r(Lu^{3+}) = 0.848 Å followed by YNiO$_3$ with r(Y^{3+}) = 0.9 Å.

LuNiO$_3$:

In the following we present the results of the high pressure electric resistivity measurements on LuNiO$_3$. Figure 4.17 (a) shows the pressure dependence of the electrical resistance of LuNiO$_3$ between 4.2 and 300 K at different pressures up to 23 GPa. Since the value of T_{MI} for LuNiO$_3$ at ambient pressure is much higher than room temperature, one observes an insulating behavior, i.e. dR/dT < 0 at $p = 1.2$ GPa. With increasing pressure ($1.2 < p < 5.8$ GPa) we observe a strong reduction of $R(T)$ and a gradual decrease of the magnitude of dR/dT. For $p \geq 2.7$ GPa one observes the evolution of a small anomaly with a maximum (T_{max}) in $R(p, T)$ around
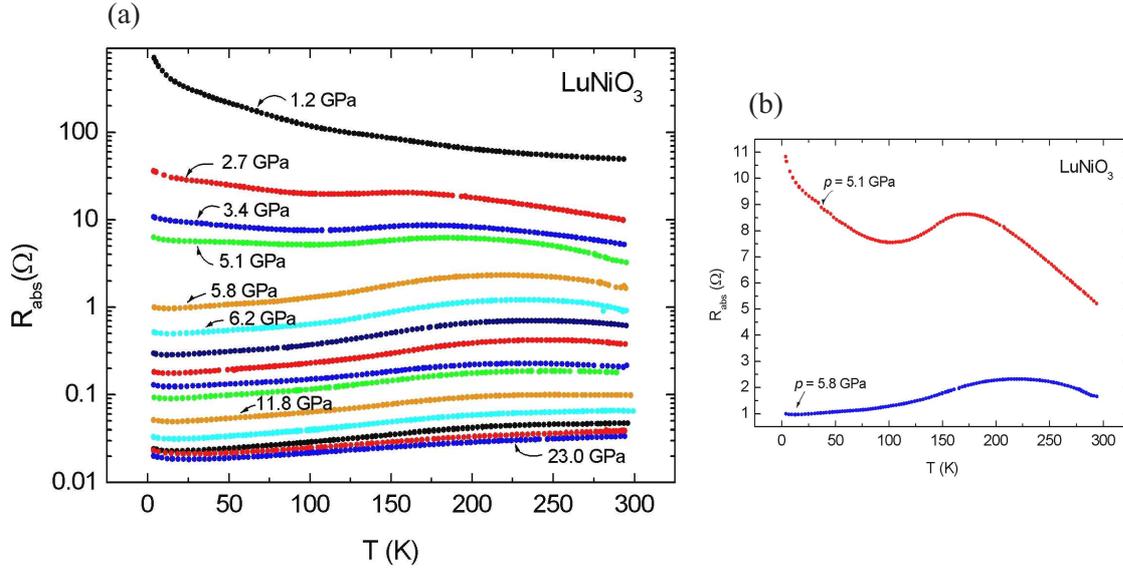
Figure 4.17: (a) Pressure dependence of the electrical resistance of LuNiO$_3$ under high pressure. The pressure of the curves between $p = 6.2$ GPa and $p = 23.0$ GPa are 7.0, 8.0, 9.5, 10.4, 11.8, 14,4, 16.2, 18.9 GPa. (b) $R(p, T)$ for $p = 5.1$ and 5.8 GPa. The change of the signum in dR/dT indicates the IM transition.

150 K which shifts to higher temperatures with increasing pressure. We attribute this anomaly to be correlated with the magnetic ordering temperature T_N in the sample which will be discussed later in chapter 4.6.2. The small increase of the resistivity below 10 K is found to be pressure independent and is probably due to a small impurity phase in the sample. This will be not further discussed.

As shown in Figure 4.17(b) at $p = 5.1$ GPa and below $T_{max} \approx 175$ K , the resistance decreases to about 110 K and then increases down to 4.2 K, indicating a semiconductor like behavior. In contrast to this, the resistivity at $p = 5.8$ GPa shows a continuous decrease below T_{max} at ≈ 220 K down to lowest temperatures. Here, the value of $R(T)$ at 4.2 K is found to be lower than $R(T)$ at room-temperature (see Figure 4.17(b)). This signals a metallic like behavior ($\mathrm{d}R/\mathrm{d}T > 0$) or a phase transition from the insulating to a metallic state. It has to be mentioned here, that above 5.8 GPa, we find a further decrease of $R(T)$ with increasing pressure. This effect is due to the existence of grain boundaries in the used powder samples and is found to be of different size in different RNiO$_3$ samples.

From the geometry of the contacted sample inside the sample chamber of the DAC, we roughly estimate the specific resistance (ρ) of LuNiO$_3$ of the order of $10^{-3}\Omega$cm for $p = 5.8$ GPa at 4.2 K and $\approx 10^{-5}\Omega$cm for $p = 23.0$ GPa at 4.2 K. These values are higher than those typical for metallic systems, but comparable with those

reported for other members of the RNiO$_3$ series. For example, the value of ρ in the metallic state of PrNiO$_3$ and NdNiO$_3$ amounts to $\rho \approx 0.4$ and $1.3 \times 10^{-3} \Omega$cm at 300 K, respectively [114, 115]. This is a common feature for all investigated RNiO$_3$ samples in the metallic state (s. below).

In Figure 4.18 we compare the $R(p, T)$ curves in the high pressure range $14.4 < p < 23.0$ GPa, i.e. across the monoclinic-orthorhombic structural phase transition at $p = 16$ GPa [79]. As evident from the figure, all $R(p, T)$ curves show metallic behavior and no significant change of the shape across the structural phase transition is observed.
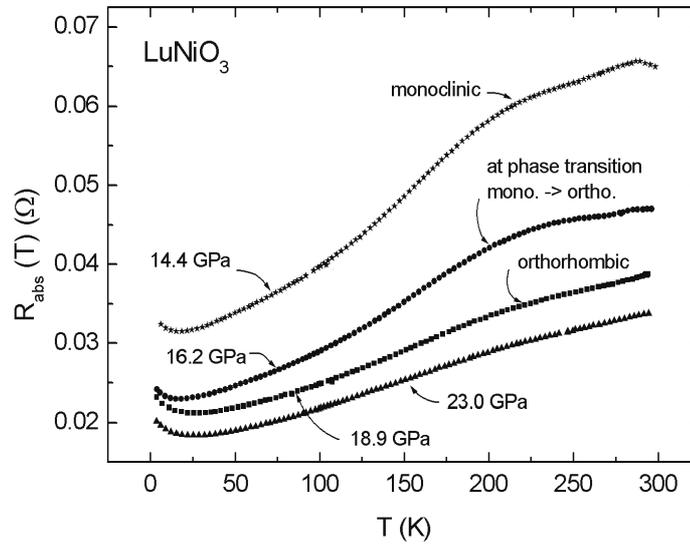
Figure 4.18: Pressure dependence of the electrical resistance of LuNiO$_3$ in the monoclinic structure at 14.4 GPa, at the structural phase transition (monoclinic $\rightarrow$ orthorhombic) at 16.2 GPa and in the orthorhombic phase at 18.9 and 23.0 GPa.

YNiO$_3$:

Figure 4.19(a) shows the pressure dependence of the electrical resistance of YNiO$_3$ between 4.2 and 300 K at different pressures up to 12.5 GPa. At ambient pressure YNiO$_3$ is semiconducting and for pressures up to 4.6 GPa we observe an increase of the electric resistance from room-temperature down to 4.2 K. Similar to the behavior in LuNiO$_3$, we observe a strong reduction of $R(T)$ and a gradual decrease of the magnitude of dR/dT with increasing pressure up to $p < 5.4$ GPa. For $p \geq 2.2$ GPa we find, similar to LuNiO$_3$, an anomaly in $R(T)$ around 175 K, which is attributed to be related to T_N and shifts to higher temperatures with increasing pressure. This will be discussed later in chapter 4.6.2.
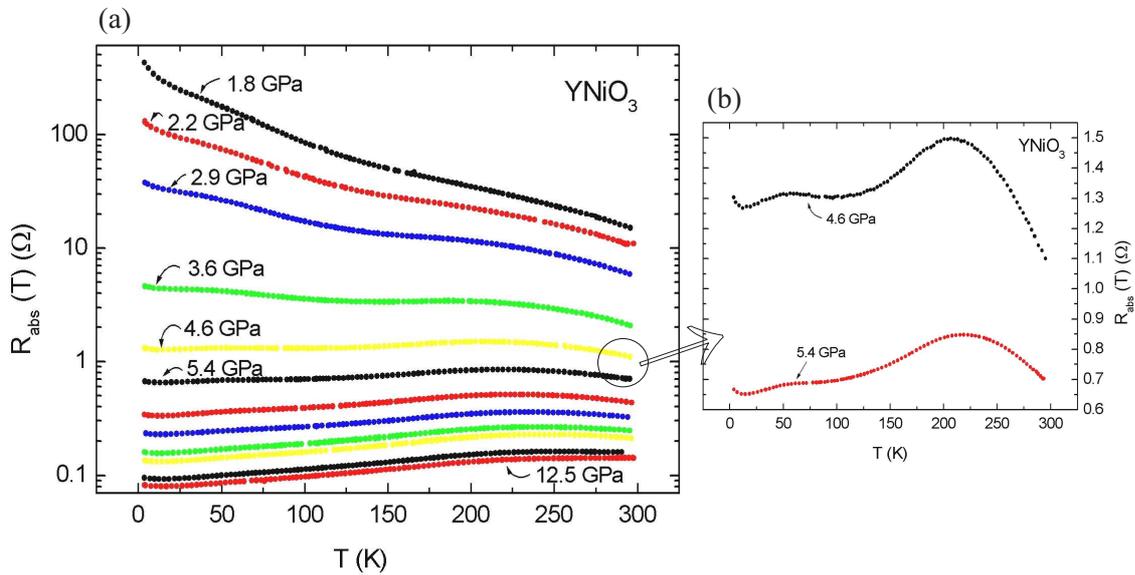
Figure 4.19: (a) Pressure dependence of the electrical resistance of YNiO$_3$ up to 12.5 GPa. The pressure of the curves between $p = 5.4$ and 12.5 GPa are 6.3, 7.7, 8.8, 10.2 and 11.5 GPa. (b) Electrical resistance of YNiO$_3$ at the pressure-induced IM transition at $p_c = 5.4$ GPa.

In Figure 4.19(b) we present the pressure dependence of $R(T)$ for $p = 4.6$ and 5.4 GPa. We find a change in the sign of dR/dT, indicating a pressure-induced IM transition in YNiO$_3$ at a critical pressure of $p_c = 5.4$ GPa.

On the other hand, all curves show around 50 K a kink which is found to be pressure independent. Measurements of $R(T)$ in magnetic fields up to 15 T did not influenced this anomaly. Since this is observed in all the subsequent rare earth nickelates, we do not comment it further on.

4.5.1.2 Electrical resistivity measurements on EuNiO$_3$ and SmNiO$_3$:

At room-temperature SmNiO$_3$ as well as EuNiO$_3$ are paramagnetic insulators with an antiferromagnetic ordering temperature of $T_N = 225$ and 205 K and a MI transition temperature of $T_{MI} = 400$ and 463 K at ambient pressure, respectively. EuNiO$_3$ has a ionic radius of 0.947 Å and belongs hereby together with SmNiO$_3$ (0.964 Å) to the larger rare earth nickelates.

EuNiO$_3$:

Figure 4.20 presents the pressure dependence of the electrical resistance of EuNiO$_3$ between 4.2 and 300 K up to 22.5 GPa. Since EuNiO$_3$ is insulating up to 463 K at ambient pressure, one observes an semiconducting behavior, i.e. $dR/dT < 0$. By applying pressure $0 \leq p \leq 5.8$ GPa, we observe a strong reduction of $R(T)$ and a gradual decrease of the magnitude of dR/dT. For $p \geq 5.8$ GPa we find a metallic-like behavior $(dR/dT > 0)$ in the whole temperature range and a further decrease of $R(T)$ with increasing pressure.
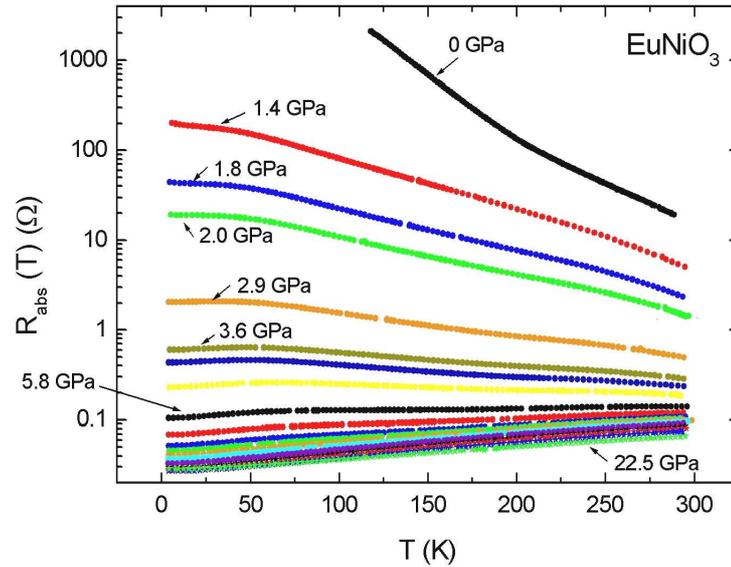
Figure 4.20: Pressure dependence of the electrical resistance of EuNiO$_3$ under high pressures up to 22.5 GPa. The pressure of the curves above 3.6 GPa are 4.0; 4.8; 5.8; 7.2; 8.5; 9.2; 10.1; 11.5; 13.2; 14.8; 15.9; 17.6 and 22.5 GPa.

As shown in Figure 4.21, at $T = 125$ K, $R(T)$ decreases by more than four orders of magnitude between 0 and 5.8 GPa. This is an indication of a gradual pressure-induced insulator to metal transition at $p_c = 5.8$ GPa.
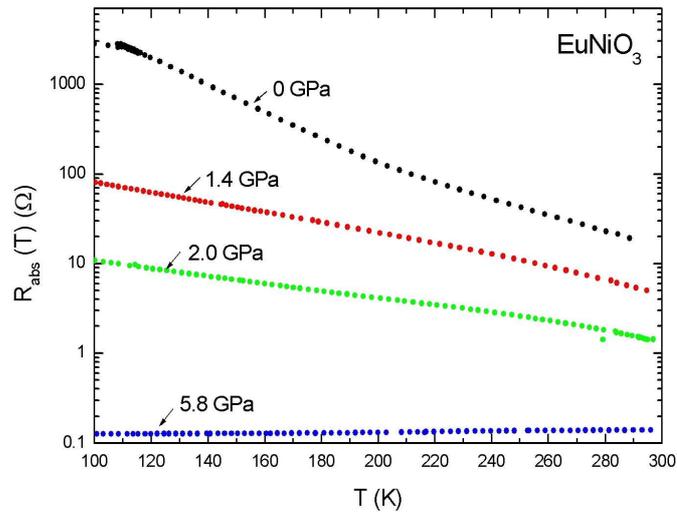
Figure 4.21: Zoomed view of the pressure-induced IM transition in EuNiO$_3$ at $p_c = 5.8$ GPa.

It has to be mentioned here, that the $R(p, T)$ curves in EuNiO$_3$ show no features that could be assigned to $T_N(p)$ as in the case of LuNiO$_3$ and YNiO$_3$.

SmNiO$_3$:

Figure 4.22(a) shows the temperature dependence of the electrical resistance on SmNiO$_3$ between 4.2 and 300 K and up to 6.7 GPa. Since SmNiO$_3$ is insulating up to 400 K at ambient pressure, we observe an insulating behavior for pressures up to 6.1 GPa. In this pressure range $R(T)$ strongly decreases together with a gradual decrease of the magnitude of dR/dT. At $p \geq 6.2$ GPa we find a continuous decrease of $R(T)$ from 300 K down to lowest temperatures ($dR/dT > 0$) which signals a metallic like behavior. No significant change in $R(T)$ is found at 6.7 GPa. As shown in Figure 4.22(b), the critical pressure for the IM transition is about 6.2 GPa.

Beyond that, also here in SmNiO$_3$ we find no indication for T_N in $R(T)$ like in LuNiO$_3$ and YNiO$_3$.
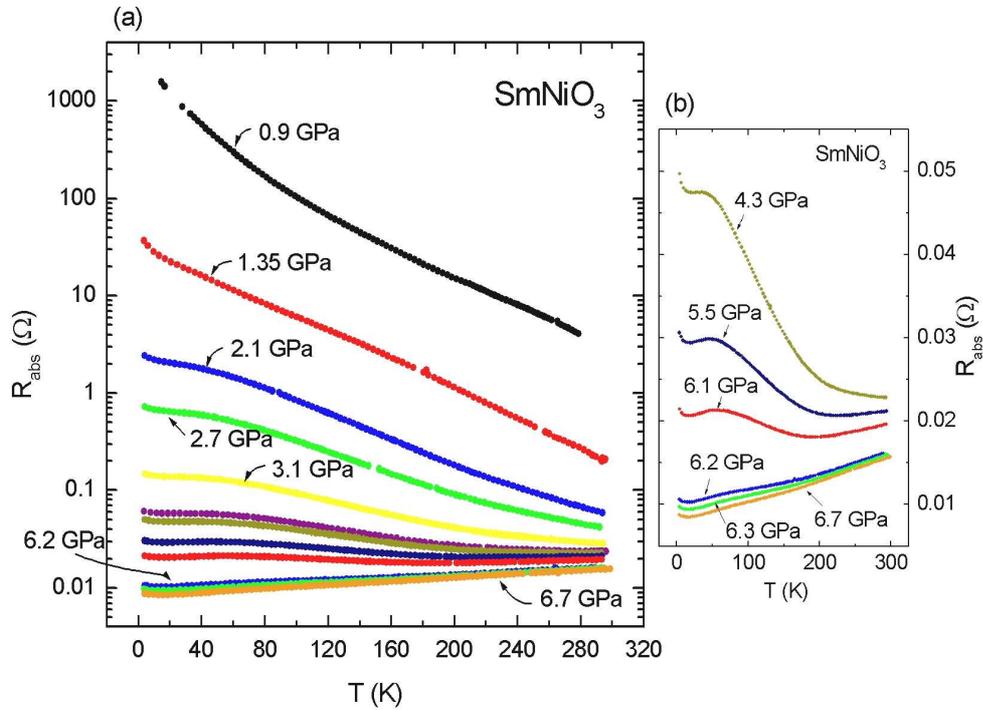
Figure 4.22: (a) Pressure dependence of the electrical resistance of SmNiO$_3$ under high pressure up to 6.7 GPa. The pressure of the curves above 3.1 GPa are 3.7; 4.3; 5.5; 6.1; 6.2; 6.3 and 6.7 GPa. (b) Electrical resistance for some selected pressures.

Pressure dependence of $T_{MI}(p)$ in SmNiO$_3$:

Since T_{MI} in SmNiO$_3$ is much lower than that in EuNiO$_3$, YNiO$_3$ and LuNiO$_3$, it was possible to determine the pressure dependence of T_{MI} at high temperatures without changing the oxygen content of the sample. Attempts to determine $T_{MI}(p)$ for EuNiO$_3$ ($T_{MI} = 463$ K at ambient pressure) were not successful due to the oxygen loss by heating the sample above 450 K.

For this particular purpose, we prepared a completely new kind of high pressure cell with a body made of Titanium alloy (Ti-6Al-4V). This material is very stable at high temperatures and prevent the cell from deformation and thereby pressure instabilities. This setup allows one to perform electrical resistivity measurements in the temperature-range $1.5 < T < 600$ K. The results for some selected pressures are shown in Figure 4.23. The inset of Figure 4.23 shows the $R(T)$ measurement at ambient pressure between 200 and 500 K on a pressed SmNiO$_3$ sample. Here, we
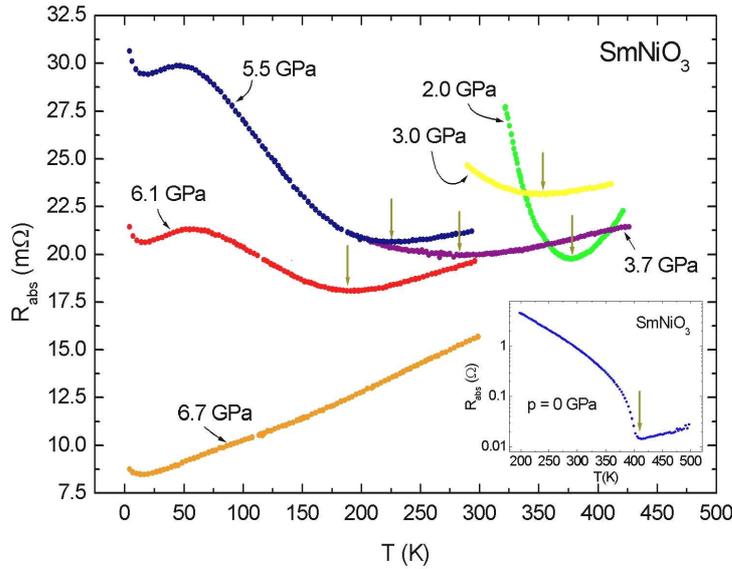
Figure 4.23: Electrical resistance of SmNiO$_3$ as a function of pressure between 4.2 and 450 K. The arrows indicate T_{MI}. The inset shows $R(T)$ at ambient pressure.

find a temperature-induced MI transition at $T_{MI} \approx 405$ K, which is in very good agreement with previous data [85]. From the curve at 2.0 GPa and high temperatures, one can clearly see the MI transition and determine T_{MI} at 377 K. At 3.0 GPa the MI transition becomes broader but T_{MI} can smoothly be determined at 353 K. These values of $T_{MI}(p)$ have been estimated from the first derivative of $R(T)$, where $\partial R/\partial T = 0$. All values for $T_{MI}(p)$ in SmNiO$_3$ are listed in Table 4.2.

p (GPa)	0	2.0	3.0	3.7	4.3	5.5	6.1	6.2
T_{MI} (K)	405	377	353	285	280	225	192	0

Table 4.2: MI transition temperatures for SmNiO$_3$ at different pressures. Due to the sharp derivatives we could estimate the value of T_{MI} within an error of $\pm$ 1 K, whereas the error of p is around $\pm$ 0.2 GPa.

In Figure 4.24 we plot the pressure dependence of T_{MI} for SmNiO$_3$ as deduced from our experimental data. Our results are compared with those reported for $T_{MI}(p)$ in PrNiO$_3$ and NdNiO$_3$ by Canfield et al. [112] and Obradors et al. [111]. As shown in the figure, PrNiO$_3$ is already metallic at 1.4 GPa and NdNiO$_3$ is expected to be metallic at 2.5 GPa. In contrast to the strong decrease of T_{MI} with pressure in PrNiO$_3$ and NdNiO$_3$, the change of $T_{MI}(p)$ in SmNiO$_3$ is quite different: The rate of decrease of T_{MI} increases with increasing pressure and shows a sudden decrease towards $T \rightarrow 0$ at 6.2 GPa. This transition is quite sharp and suggests a first order phase transition. This can be ascribed to the more localized character of SmNiO$_3$ with respect to PrNiO$_3$ and NdNiO$_3$. This point will be considered in the discussion of the mechanism of the pressure-induced IM transition section 4.6.1.
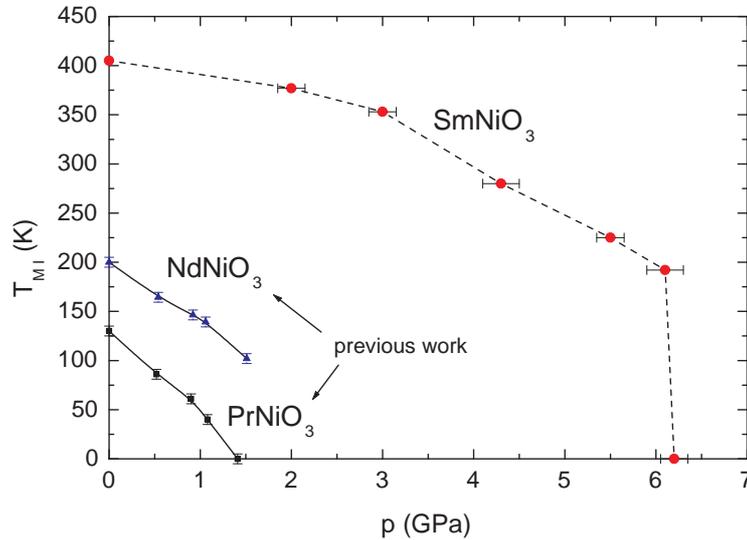
Figure 4.24: Pressure dependence of $T_{MI}(p)$ of PrNiO$_3$, NdNiO$_3$ and SmNiO$_3$. The values for PrNiO$_3$ and NdNiO$_3$ are taken from [112].

4.5.2 Structural stability of RNiO$_3$ at the pressure-induced insulator metal transition

Up to now we have found, that the pressure-induced IM transition in all examined RNiO$_3$ compounds takes place around 5 – 7 GPa. In the following section we want to demonstrate that the pressure-induced insulator metal transition is not connected with a structural phase transition.

4.5.2.1 x-ray diffraction measurements on LuNiO$_3$ and YNiO$_3$

First, we want to check if the pressure-induced IM transition for the small RNiO$_3$ compounds is connected with a structural phase transtition or not. As one can see from recent angle-resolved x-ray diffraction measurements in Figure 4.25 [79, 108], for LuNiO$_3$ (a) and YNiO$_3$ (b), there is neither an indication for a structural phase
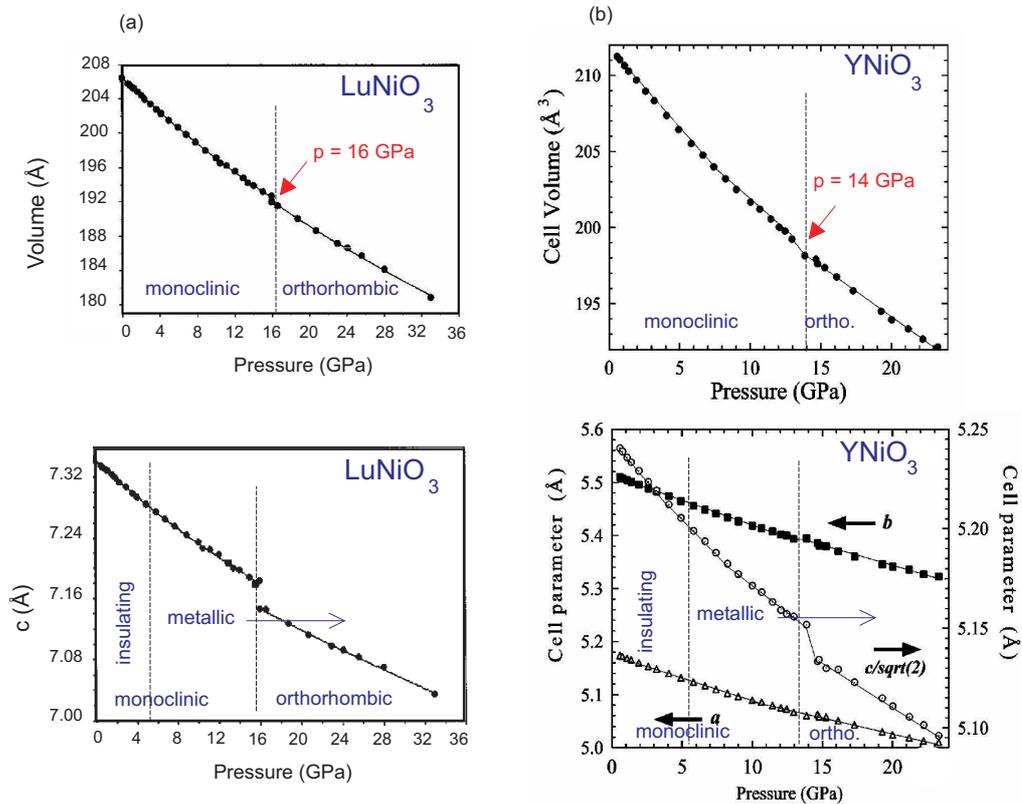
Figure 4.25: Pressure dependence of the lattice parameters and the volume in LuNiO$_3$ (a) and YNiO$_3$ (b) at 300 K. The monoclinic–orthorhombic structural phase transitions takes place at 16 and 14 GPa, respectively [79, 108]. The critical pressures for the pressure-induced IM transition are indicated by dashed lines at 5.8 and 5.4 GPa, respectively.

transition nor structural anomalies in the lattice parameters as well as in the volume at the pressure-induced IM transition. As introduced in section 4.3, a structural phase transition (monoclinic → orthorhombic) in both compounds has been found at 16 and 14 GPa, respectively. But these phase transitions take place at much higher pressures and apparently have nothing to do with the observed pressure-induced IM transition which we find in our measurements. As a result, we can conclude that the pressure-induced IM transition in LuNiO$_3$ and YNiO$_3$ is not connected with a structural phase transition.

4.5.2.2   x-ray diffraction measurements on EuNiO$_3$ and SmNiO$_3$

We now consider the pressure dependence of the lattice parameters (a, b and c) and the volume of the orthorhombic unit cell in EuNiO$_3$ as obtained from our energy dispersive x-ray (EDX) diffraction measurements at 300 K at beamline F3 at Hasylab (Hamburg). Figure 4.26 presents the x-ray diffraction patterns of EuNiO$_3$ as
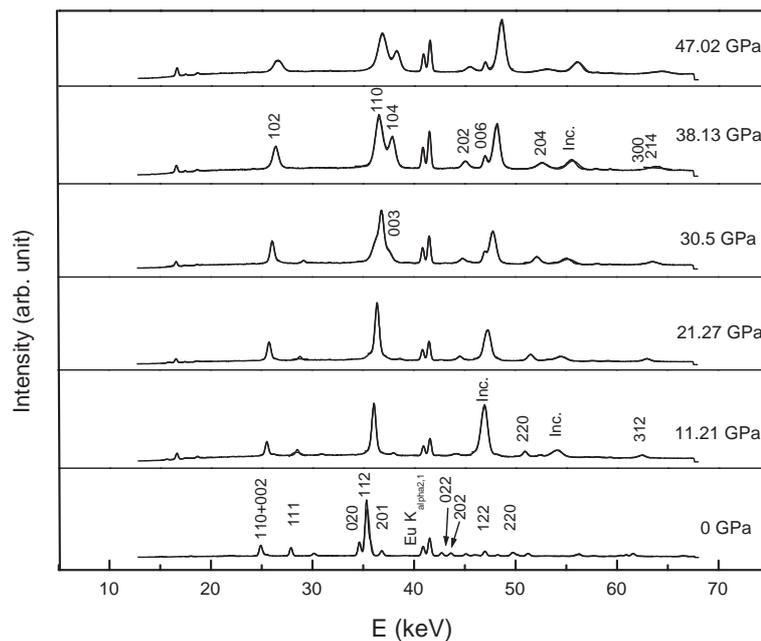
Figure 4.26: Energy dispersive x-ray diffraction patterns of EuNiO$_3$ between ambient pressure and 47 GPa. Above 30 GPa the symmetry changes from an orthorhombic ($Pbnm$) to a rhombohedral ($R\bar{3}c$) structure. All patterns are refined with the program EDXPowd.

a function of energy for some selected pressures between 0 and 47.02 GPa. The most important peaks are labeled by their (hkl). For $p \leq 30.5$ GPa the patterns are described in an orthorhombic ($Pbnm$) symmetry and above in a rhombohedral ($R\bar{3}c$) symmetry. Due to the tiny sample chamber ($\oslash \approx 150~\mu$m) one additionally observes some Bragg reflections of the Inconel gasket in the diffraction patterns. These characteristic peaks are labeled with Inc. One can also see very clearly the K$_{\alpha 1}$ and K$_{\alpha 2}$ fluorescence peaks of Eu around 41 and 42 keV. They are pressure independent and can be seen through the whole experiment up to highest pressures at the same energy.

The most interesting feature is the splitting of the huge 112 peak at ~ 35 keV with increasing pressure. At 30.5 GPa this peak becomes definitely broader and as one can clearly see in the spectra at 38.13 GPa, it splits into two peaks, indicating a structural phase transition (orthorhombic ($Pbnm$) $\rightarrow$ rhombohedral ($R\bar{3}c$)).

In Figure 4.27 we show the pressure dependence of the lattice parameters a, b and c of EuNiO$_3$ at room-temperature up to 47.02 GPa. With increasing pressure b decreases more rapidly than a and c, and the value of c seems to saturate around 20 GPa. Such a change of a, b and c indicates a gradual decrease of the orthorhombic distortion of the unit cell with increasing pressure. The saturation behavior of the lattice parameter c around 20 GPa can be considered as a first indication that the orthorhombic structure is approaching a structural phase transition with higher symmetry. Indeed, our measurements indicate a structural phase transition above 30 GPa from orthorhombic to rhombohedral symmetry across a mixed phase between 25 and 30 GPa. Up to 25 GPa the lattice parameters can be well described in an orthorhombic symmetry, whereas above 25 – 30 GPa the quality of the fits become poor, indicating a coexistence of the two phases. In any case, above 32 GPa we find a clear rhombohedral structure. This orthorhombic $\rightarrow$ rhombohedral phase transition has also been observed in PrNiO$_3$, NdNiO$_3$ and SmNiO$_3$ at 6; 12 and above 28 GPa, respectively [79].

To be able to compare the cell parameters of cell with different symmetry, they have been reduced to their equivalent cubic values. Thus, we normalized the orthorhombic a- and b-cell parameters by $\sqrt{2}$ and the c-cell parameter was divided by a factor of 2. The rhombohedral cell parameters are referred to the hexagonal setting[2], the a-cell parameter is normalized by $\sqrt{2}$, while the rhombohedral c-cell parameter was divided by $2\sqrt{3}$. The dashed lines in Figure 4.27 display the zone in which both structures can coexist.

We have also determined the pressure dependence of the unit cell volume (see inset of Figure 4.27) up to 20 GPa (in the orthorhombic phase) which we fitted to the Birch-Murnaghan equation of state. The values of the bulk modulus B_0 and its

---

[2]The volume of the hexagonal unit cell can be calculated as $V = \frac{\sqrt{3}}{2} \cdot a^2 c$.
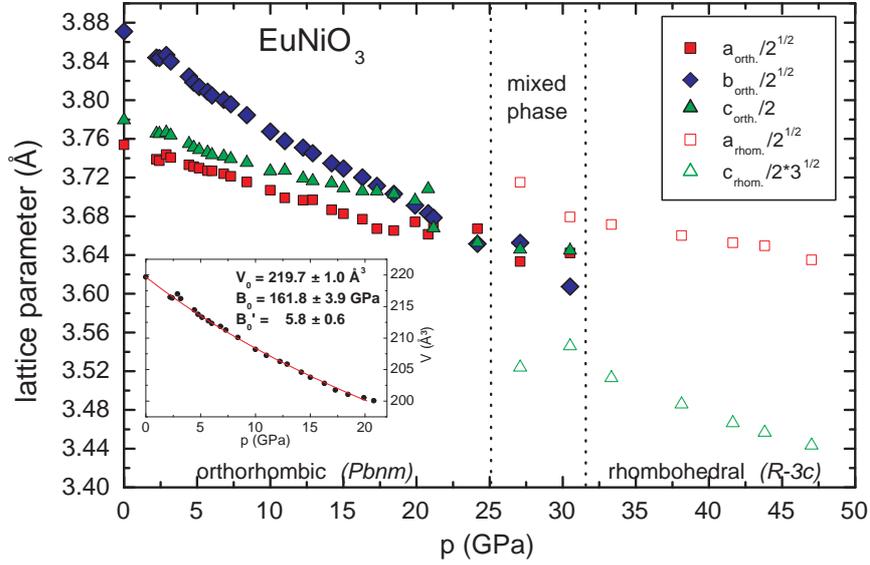
Figure 4.27: Pressure dependence of the lattice parameters of EuNiO$_3$ as obtained from high pressure energy dispersive synchrotron x-ray diffraction measurements at 300 K. At the critical pressure for the pressure-induced IM transition ($p_c = 5.8$ GPa) we find no indication for a structural phase transition. Inset: Pressure dependence of the volume of EuNiO$_3$ fitted to the Birch-Murnaghan equation of state in the orthorhombic structure.

derivative B_0' are 161.8 GPa and 5.8, respectively. These are comparable to the values found in SmNiO$_3$ ($B_0 = 167$ GPa, $B_0' = 4.3$)[113].

Thus, within the accuracy of the measurement, we find no discontinuity in the pressure dependence of the lattice parameters a, b and c (and the volume), showing any indication of a structural anomaly or phase transition at the pressure-induced IM transition around $p_c = 5.8$ GPa. Therefore, the above mentioned high pressure results clearly show that the transition from the insulating state to a metallic state at 5.8 GPa is not connected with a change of the symmetry of the orthorhombic structure.

Also in SmNiO$_3$ (see Figure 4.28), no indication for a structural phase transition at the pressure-induced IM transition ($p = 6.2$ GPa) could be found. However, as shown in the inset of Figure 4.28, the authors found structural anomalies in the b lattice parameter at 300 K and 2.5 GPa as already mentioned in section
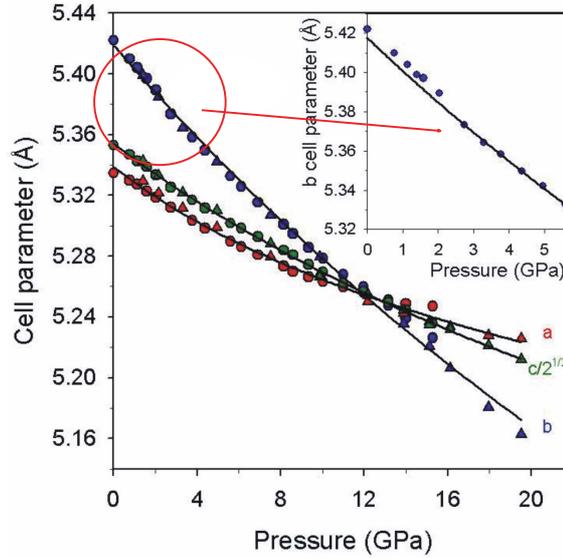
Figure 4.28: Change of local structure at 2.5 GPa and room-temperature in SmNiO$_3$ as obtained from angle resolved x-ray diffraction measurements [113].

4.3. According to this they observed a large anomaly in the Ni-O-Ni bond angle. They explain this behavior with a beginning of metallization without calling this pressure-induced state above 2.5 GPa "metallic". Apart from such small structural anomalies in SmNiO$_3$, no structural phase transition could be found to explain the pressure-induced IM transition at $p_c = 6.2$ GPa. In chapter 4.6.1.1 we will discuss the possible connection of the structural anomalies in the b lattice parameter to the pressure-induced IM transition.

In summary, from our structural considerations on RNiO$_3$'s under high pressure we can now conclude that the symmetry of the monoclinic and/or orthorhombic structure does not change at the pressure-induced insulator to metal transition. For the RNiO$_3$ with small R^{3+} ionic radius no further indication could be detected, whereas for the larger RNiO$_3$ (SmNiO$_3$, NdNiO$_3$ and PrNiO$_3$) subtle changes of the local structure have been observed with increasing pressure. This latter point will be discussed in the following section 4.6.1.1.

4.6 Discussion

4.6.1 Possible mechanism of the pressure-induced insulator metal transition in RNiO$_3$

Now we want to discuss the possible mechanism which could be responsible for the pressure-induced IM transition in all RNiO$_3$ compounds. As mentioned in section 4.5.2, the pressure-induced IM transition in RNiO$_3$ compounds is not connected with a structural phase transition. In the following we would like to investigate its connection to changes of structural parameters e.g. d_{Ni-O} bond length and $\theta_{Ni-O-Ni}$ bond angle.

4.6.1.1 Change of structural parameters

From angle resolved x-ray diffraction measurements on SmNiO$_3$ under pressure by Amboage et al. [113], we know that the abrupt decrease of the b-cell parameter is directly connected with an anomaly in the Ni-O-Ni bond angle θ (see Figure 4.29(a)). The authors explain this behavior at 2.5 GPa and 300 K, by the beginning of metallization, without calling this state metallic.

If we compare their results with our findings from the resistivity measurements on SmNiO$_3$ under pressure and at room-temperature, we can correlate the observed structural anomaly with the drop of the room-temperature resistivity to values typical for metals. This is shown in Figure 4.29(b) which displays the change of the absolute resistance with pressure in SmNiO$_3$ at 290 K. With increasing pressure, the
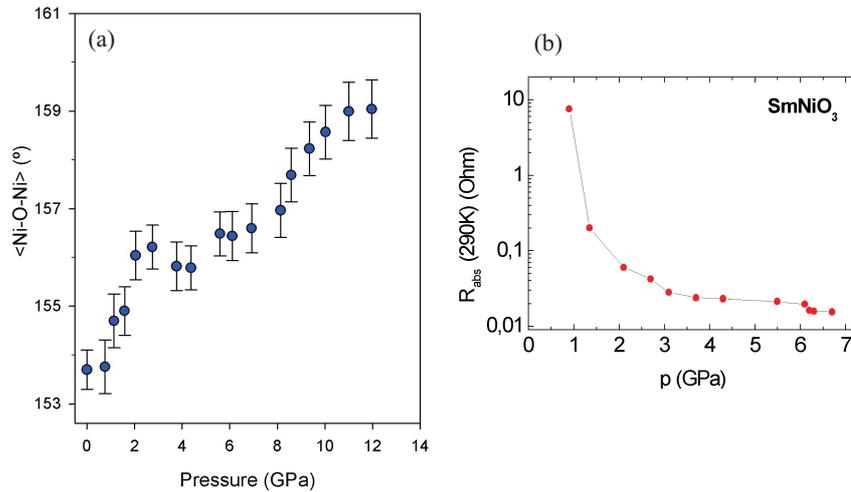
Figure 4.29: (a) Pressure dependence the average bond angle $\theta_{Ni-O-Ni}$ of SmNiO$_3$ [113]. (b) Pressure dependence of the room-temperature electrical resistivity of SmNiO$_3$.

absolute resistance strongly decreases from 10 Ω at $p \approx 1$ GPa to about 20 mΩ at
3 GPa ($\rho \approx 10$ $\mu\Omega$cm) and remains nearly unchanged at higher pressures. Also for
EuNiO$_3$ careful angle resolved x-ray diffraction measurements using synchrotron ra-
diation show a very small contraction of the b-cell parameter around 4.5 GPa [116].
This again correlates with our resistivity data on EuNiO$_3$ (see Figure 4.20). Thus,
our observation of a metallic conductivity at room-temperature in SmNiO$_3$ indicates
that the transition temperature T_{MI} decreases from ≈ 400 K at ambient pressure to
~ 300 K above 3 GPa, which is supported by our results of the pressure dependence
of T_{MI} in SmNiO$_3$ (see Figure 4.24). A similar but much larger reduction of T_{MI}
with pressure has been observed in NdNiO$_3$ and PrNiO$_3$ [112] (see Figure 4.24). It
has been explained by a gradual decrease of the average $\langle$Ni-O$\rangle$ bond length d_{Ni-O}
and a simultaneous increase of the average $\langle$Ni-O-Ni$\rangle$ bond angle θ with increasing
pressure [112, 90]. Both changes of $\langle d_{Ni-O} \rangle$ and $\langle \theta_{Ni-O-Ni} \rangle$ result in an increase of
the effective bandwidth ($W \sim \cos\omega / d_{Ni-O}^{3.5}$, with $\omega = 2\pi - \theta$, [117]) and thereby
closing the small charge transfer gap.

However, we would like to comment on the change of $\langle \theta_{Ni-O-Ni} \rangle$ with increasing
pressure regarding the observed pressure-induced IM transition in the RNiO$_3$ se-
ries. Figure 4.30 shows the change of $\langle \theta_{Ni-O-Ni} \rangle$ caused by external pressure and
due to change of R^{3+} size (internal pressure). According to the phase diagram of
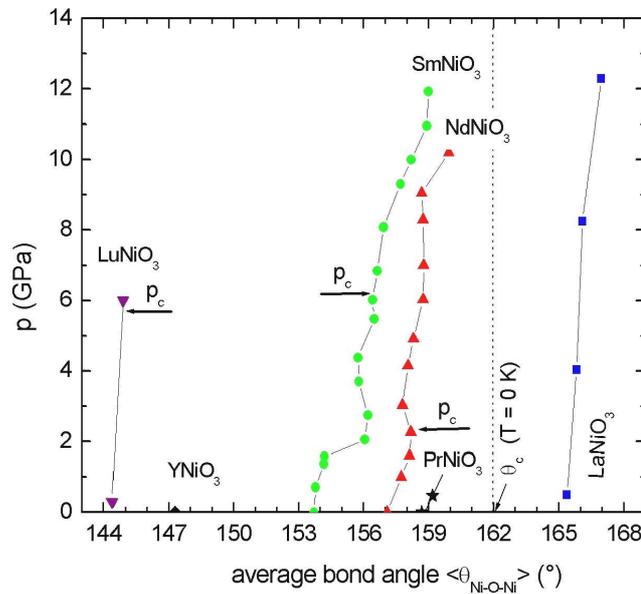
Figure 4.30: The effect of internal and external pressure on the average bond angle θ
in RNiO$_3$. Above θ_c all systems are metallic for $T \rightarrow 0$ K and ambient
pressure. The arrows indicate the values of the critical pressures p_c for the
pressure-induced IM transition in NdNiO$_3$, SmNiO$_3$ and LuNiO$_3$ at 2.5,
6.2 and 5.8 GPa, respectively.

$RNiO_3$ series (see Figure 4.5), the crossover between the insulating and metallic state at ambient pressure and $T \to 0$ is defined by a tolerance factor $t \approx 0.98$, which corresponds to a critical bond angle of $\theta_c \approx 162$ K. This is also indicated in Figure 4.30. This figure clearly demonstrates that the increase of θ, necessary for a crossover from the insulating to the metallic state by external and internal pressure, is quite different: While internal pressure causes a very large decrease of θ (e.g. θ for $LuNiO_3$ ($\sim 144°$), which is about $18°$ smaller than θ_c ($\sim 162°$)), the effect of external pressure is an order of magnitude smaller (e.g. θ increases by $1 - 2°$ at the pressure-induced IM transition of $NdNiO_3$ and $SmNiO_3$, respectively). Consequently, the metallic state can be achieved at values of θ which are much lower than θ_c. Indeed, as we will show later in the case of $LuNiO_3$, we nearly find no change of θ with pressure at the pressure-induced IM transition. From this we can conclude that the pressure-induced IM transition in $RNiO_3$ is dominated by a decrease of the $\langle Ni\text{-}O \rangle$ bond length rather than by an increase of the average bond angle θ. This last point will be discussed in the case of $LuNiO_3$ in the next section 4.6.1.2.

In the following we compare the pressure dependence of T_{MI} for $SmNiO_3$ with that for $NdNiO_3$ and $PrNiO_3$. Figure 4.31(a,b) shows the comparison of the volume dependence of T_{MI} for $SmNiO_3$ as obtained from our high pressure resistivity data and that reported for $PrNiO_3$ and $NdNiO_3$ [112, 111], by using the values of the bulk modulus for $PrNiO_3$ ($B_0 = 148$ GPa), $NdNiO_3$ ($B_0 = 163$ GPa) and $SmNiO_3$ ($B_0 = 167$ GPa) [79]. Two essential differences are evident from the figure:
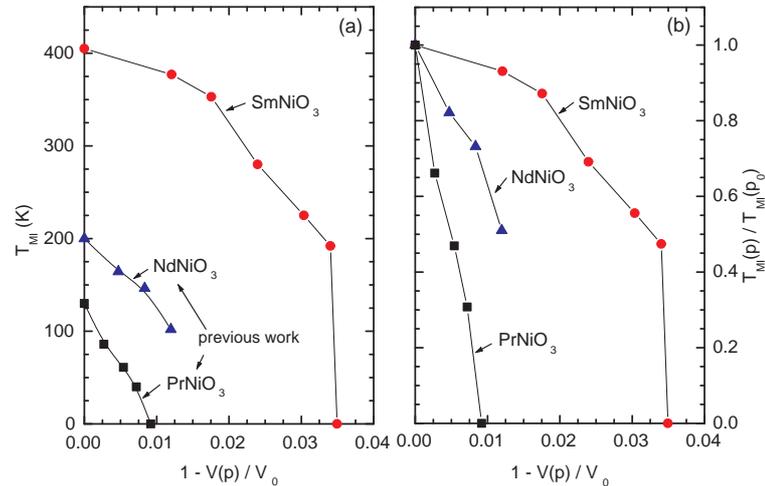
Figure 4.31: (a) Comparision of the volume dependence of T_{MI} of $SmNiO_3$ with $PrNiO_3$ and $NdNiO_3$. (b) Normalized $T_{MI}(p)$ as a function of volume reduction.

(i) the initial decrease of T_{MI} with decreasing volume for SmNiO$_3$ is much smaller than that for PrNiO$_3$ and NdNiO$_3$; and (ii) the sharp drop of T_{MI} at the critical pressure suggests that the pressure-induced insulator metal transition in SmNiO$_3$ is of a first order.

The reason for such differences could be related to the fact, that in SmNiO$_3$ pressure acts on a charge ordered state that is strongly coupled to the lattice, whereas in PrNiO$_3$ it mainly acts on the antiferromagnetic state (probably spin density wave like). In addition, PrNiO$_3$ is closer to the crossover to a nonmagnetic state (i.e. quantum critical point [10]) than SmNiO$_3$. Thus, the different nature of the insulating states in PrNiO$_3$ and SmNiO$_3$ can strongly affect the pressure dependence of T_{MI}. For a better understanding of this mechanism, further systematic studies of $T_{MI}(p)$ in smaller RNiO$_3$ are highly desired.

4.6.1.2   Influence of charge ordering

In the previous section we have discussed the pressure-induced IM transition in EuNiO$_3$ and SmNiO$_3$ and its possible connection with small changes of the structural parameter d_{Ni-O} and $\theta_{Ni-O-Ni}$. In the case of LuNiO$_3$ and YNiO$_3$, high pressure angle resolved x-ray diffraction studies reveal no anomalies of the structural parameter at the critical pressure of the pressure-induced IM transition at 5.8 and 5.4 GPa, respectively (see Figure 4.25(a,b)). The puzzle that remains to be solved is the observation of a pressure-induced metallic state with a monoclinic structure in which a charge ordered state exists. One has to recognize that the structural phase transitions (monoclinic $\rightarrow$ orthorhombic) have been observed at much higher pressures of 16 and 14 GPa for LuNiO$_3$ and YNiO$_3$, respectively [79, 108].

In order to understand the interplay between the charge ordering, local structure and the evolution of the metallic state in RNiO$_3$ series, we have performed room-temperature high resolution neutron powder diffraction measurements on LuNiO$_3$ at the Rutherford Appleton Laboratory (ISIS, Oxford) at ambient pressure and 6 GPa in the pressure cell. A Paris-Edinburgh high pressure cell with an encapsulated gasket for nearly hydrostatic pressure condition has been used. The setup and the pressure cell are described in chapter 3.6.2.

The neutron powder diffraction patterns (NDP) (0 and 6 GPa) at 300 K are shown in Figure 4.32(a,b). The refinement of the NDP was performed by the Rietveld method implemented by the program GSAS (Larsen and Von Dreele) in the monoclinic space group ($P2_1/n$) [118]. The measurement at ambient pressure was performed in the high pressure cell for a period of 560 μAh (ca. 17.3 h), whereas the data set at 6 GPa was recorded of 740 μAh (ca. 22.9 h). The values of the structural parameters at ambient pressure $d_{\mathrm{Ni}i-\mathrm{O}j}$ and $\theta_{\mathrm{Ni}i-\mathrm{O}j-\mathrm{Ni}k}$ (with $i, k = 1, 2$ ($i \neq k$) and $j = 1, 2, 3$) are in a very good agreement with those previously reported [104].

The values of the structural parameters evaluated at ambient pressure and 6 GPa
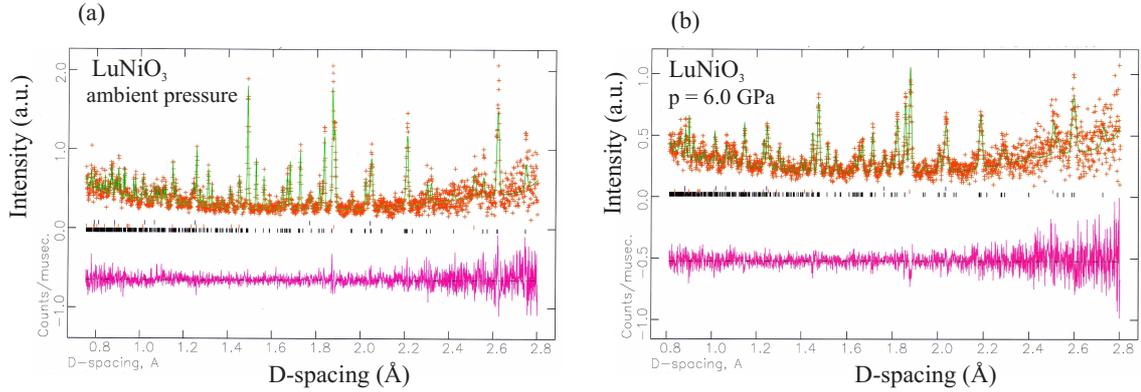
Figure 4.32: Neutron diffraction patterns on LuNiO$_3$ at 300 K at (a) $p \approx 0$ GPa and (b) $p = 6$ GPa measured at ISIS (Oxford).

bond length d	ambient pressure	6 GPa	$\Delta d/d$ (%)
2× Ni1–O1	1.955(14) Å	1.913(23) Å	2.15
2× Ni1–O2	2.039(15) Å	2.014(23) Å	1.2
2× Ni1–O3	2.005(13) Å	1.985(19) Å	1.0
2× Ni2–O1	1.902(15) Å	1.903(24) Å	≈ 0
2× Ni2–O2	1.904(13) Å	1.889(21) Å	0.8
2× Ni2–O3	1.935(14) Å	1.914(22) Å	1.1
bond angle θ	ambient pressure	6 GPa	$\Delta\theta/\theta$ (%)
Ni1–O1–Ni2	144.3(4)°	144.9(6)°	0.42
Ni1–O2–Ni2	144.4(9)°	144.7(13)°	0.21
Ni1–O3–Ni2	144.6(8)°	145.1(13)°	0.35

Table 4.3: Structural parameters (d_{Ni-O} bond length and $\theta_{Ni-O-Ni}$ bond angle) as obtained from the analysis of high resolution neutron powder diffraction measurements on LuNiO$_3$ at ambient pressure and 6 GPa.

for the two Ni-sites (Ni1 and Ni2) which form the Ni1O$_6$ and Ni2O$_6$ octahedra, respectively are given in Table 4.3. Comparing the change of the bond lengths with increasing pressure in the two octahedra, we obtain the following interesting results: The bond lengths of Ni1-O2 and Ni1-O3 decrease by nearly the same amount ($\Delta d/d \sim 1$ %) as those of Ni2-O2 and Ni2-O3. In contrast to this, the Ni1-O1 bond length decreases by more than 2 %, while that of Ni2-O1 remains unchanged (see Figure 4.33). At 6 GPa, the values of d_{Ni1-O1} amounts to 1.913(23) Å and become nearly equal to that of d_{Ni2-O1} (1.903(24) Å). Such an anisotropic response of the apex Nii-O1 bond length of the two Ni-sites destroys the alternating long-short bond length periodicity along the c-axis. This leads to a pressure-induced partial melting of the charge ordering of Ni^{3+} ions which results in a metallic conductivity along the c-axis and thereby triggers the insulator metal transition with increasing pressure. Here, it is important to mention that in such a metallic state the Ni1O$_6$
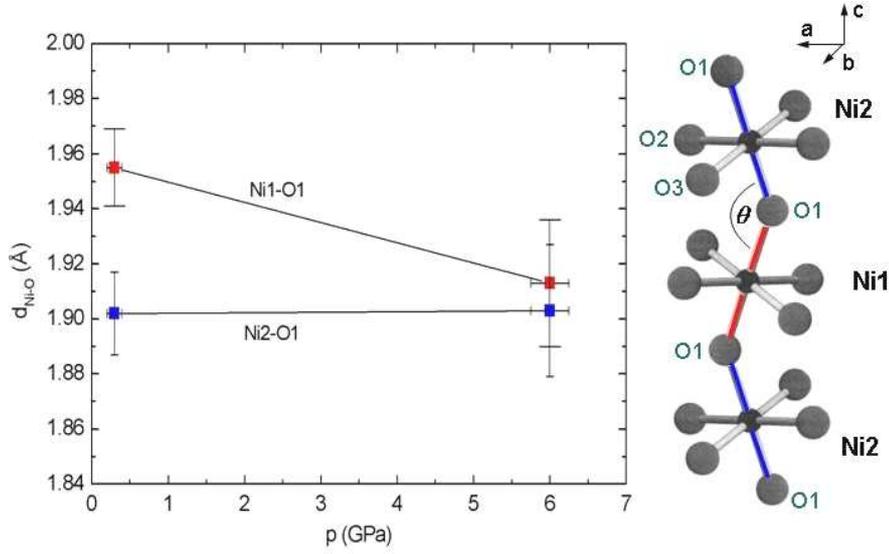
Figure 4.33: Pressure dependence of Ni1-O1 and Ni2-O1 bond length of LuNiO$_3$ at ambient pressure and 6 GPa as obtained from high resolution neutron diffraction spectroscopy.

and Ni2O$_6$ octahedra are still different in size along the a, b-plane and the c-direction and alternate in all 3 crystallographic directions. This explains the coexistence of the metallic state with partially melted charge ordered state in the monoclinic structure under pressure.

It has to be mentioned here, that a smaller monoclinic distortion below T_{MI} has been recently observed in larger RNiO$_3$ (R = Eu, Sm) and extends to NdNiO$_3$ using infrared spectroscopy [101], Raman-scattering [119] and resonant x-ray scattering [92]. We, thus, feel that our observation of a partial melting of charge ordering in LuNiO$_3$ provides a common physical picture for the pressure-induced insulator-metal transition in RNiO$_3$ series.

4.6.2   Pressure dependence of T_N in RNiO$_3$

The next aspect which we want to consider is the pressure dependence of T_N in some selected RNiO$_3$ samples. As mentioned in section 4.5.1.1, the pressure dependence of T_N can be followed from the anomaly (maximum) observed in the $R(p,T)$ data (T_{max}) for LuNiO$_3$ and YNiO$_3$, while this anomaly has not been observed in EuNiO$_3$ and SmNiO$_3$. In this section we present the pressure dependence of T_{max} in LuNiO$_3$ and YNiO$_3$ as deduced from our $R(p,T)$ measurements. In addition, we have directly determined the initial change of T_N with pressure from magnetization measurements up to 1.5 GPa in LuNiO$_3$. In the case of EuNiO$_3$, we have obtained information on the pressure dependence of T_N using high pressure ^{151}Eu nuclear forward scattering (NFS) of synchrotron radiation. All of these results will be presented and discussed below.

4.6.2.1   LuNiO$_3$ and YNiO$_3$:

From our high pressure resistance measurements on LuNiO$_3$ (see Figure 4.17), we find a pronounced maximum (T_{max}) in $R(p,T)$ for $p \geq 2.7$ GPa, which we assume that it is related to T_N. The value of T_{max} at 2.7 GPa is estimated to be 152.5 K[3], which is higher than the value of $T_N = 128$ K at ambient pressure [79]. Following the assumption that T_{max} is related to T_N, this value of T_{max} indicates an increase of T_N with increasing pressure (see Figure 4.34), which would be expected for a localized $3d$ state in the insulating state of LuNiO$_3$. In order to support our assumption, we have performed DC magnetization measurements on LuNiO$_3$ under pressure (1.5 GPa). These magnetization measurements have been done in collaboration with Dr. Andrew Podlesnyak from the Paul-Scherrer-Institut (Villigen, Switzerland) and were performed by using a Quantum Design PPMS (Physical Property Measurement System). The used high pressure cell is similar to that described in section 3.2.2. In Figure 4.35(a,b) we show the temperature dependence of the inverse magnetization ($1/M$) at ambient pressure and at 1.5 GPa. The results clearly show an increase of T_N from 125 K (ambient pressure) to 131 K (1.5 GPa). This is a strong support that the increase of T_{max} with increasing pressure is correlated to an increase of T_N.

A quantitative analysis of the initial change of T_N with pressure results in a value of $\frac{1}{T_N}\frac{\partial T_N}{\partial p} \cong 3.3 \times 10^{-2}$ GPa^{-1} which corresponds to a volume dependence of $\frac{1}{T_N}\frac{\partial T_N}{\partial \ln V} \cong 6.2$. This value is very similar to that very recently obtained for SmNiO$_3$ ($\cong 6.1$) [120]. Thus, the positive coefficient ($\partial T_N/\partial p > 0$) found in LuNiO$_3$ and SmNiO$_3$ confirms the localized character of the $3d$-states of RNiO$_3$ (R = Sm,..,Lu) in the insulating state.

---

[3]We determined $T_{max}(p)$ by the first derivative of $\partial R_{abs}(T)/\partial T = 0$ and defined the zero point to be T_{max}.
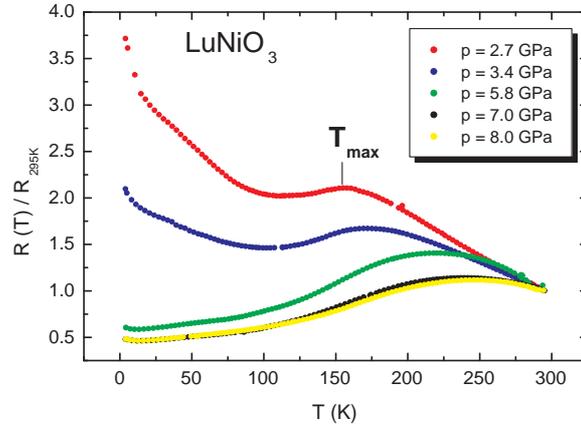
Figure 4.34: Normalized resistance of LuNiO₃ for $2.7 < p < 8.0$ GPa. The diagram shows the shift of T_{max} to higher temperatures with increasing pressure.
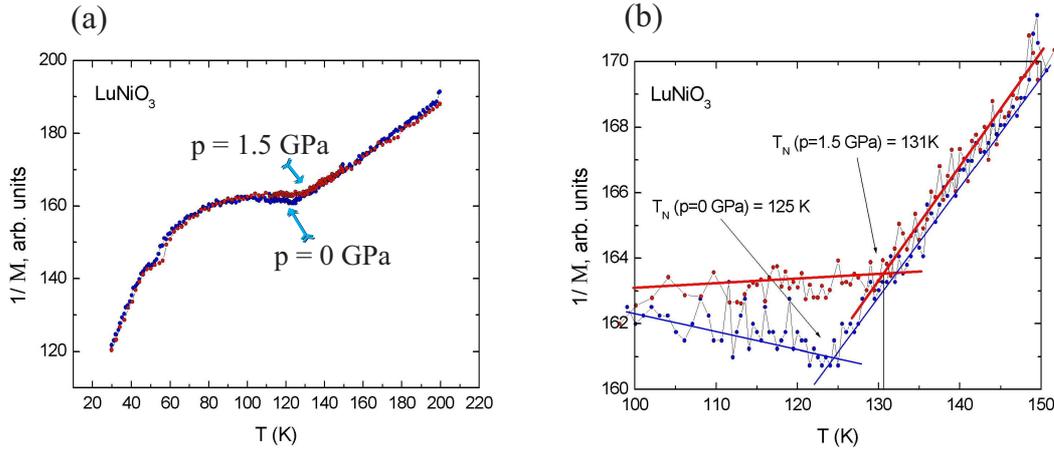
Figure 4.35: Temperature dependence of the inverse magnetization on LuNiO₃ at ambient pressure and 1.5 GPa. Under pressure T_N increases from 125 to 131 K. (a) Total view of the measurements (b) zoomed interesting region of $T_N(p)$.

We now discuss the pressure dependence of T_{max} in LuNiO₃ which reflects at least qualitatively the pressure dependence of T_N. The values of T_{max} as deduced from $R(p,T)$-data up to 23 GPa are shown in Figure 4.36 together with the values of T_N obtained from the magnetization measurements at 0 and 1.5 GPa. As evident from the figure, the pressure-induced increase of T_{max} (T_N) is larger in the insulating state ($p \leq 5.8$ GPa) than that in the metallic state ($5.8 < p < 11$ GPa). In the
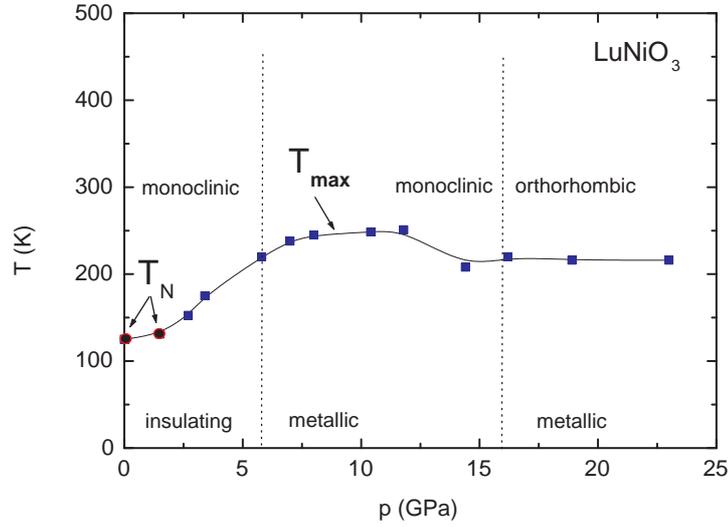
Figure 4.36: $T_N(p)$ as deduced from magnetization measurement (at $p = 0$ and 1.5 GPa) under pressure and $T_{max}(p)$ derived from the pressure dependent maximum in $R(p, T)$.

pressure range across the structural phase transition at 16 GPa, we find within the accuracy of determining T_{max} no significant change. The different pressure dependence of T_{max} observed in the insulating and metallic states is due to the fact that the nature of the magnetic ground state in these two phases is essentially different: while magnetism in the insulating state is determined by superexchange interactions between localized $3d$ electrons, it is governed in the metallic state by itinerant $3d$ electrons, e.g. by a spin density wave-like state. Accordingly, the large increase of T_{max} with pressure in the insulating state can be explained by the increase of the effective hopping $(t_{pd} \propto \left(\frac{1}{d_{Ni-O}}\right)^\alpha, \alpha = 3.5)$ which results in an increase of the effective exchange interaction $(J_{ex} \propto t_{pd}^2)$ and a large increase of T_N. On the other hand, it is difficult to predict the strength of the pressure dependence of T_N in the pressure-induced metallic state. In the case of the metallic state the dependence of T_N on pressure is more complex, as pressure can affect the coupling constant, band width and the shape of the Fermi surface [121]. Such complicity may lead to a weaker pressure dependence of T_N as observed in LuNiO$_3$ (see Figure 4.36).

In the case of YNiO$_3$, we obtain similar results which are shown in Figure 4.37: The increase of $T_{max}(p)$ in the insulating state $(p \leq 5.4$ GPa$)$ is stronger than that for the metallic state $(p > 5.4$ GPa$)$. Also, the rate of increase of $T_{max}(p)$ in the
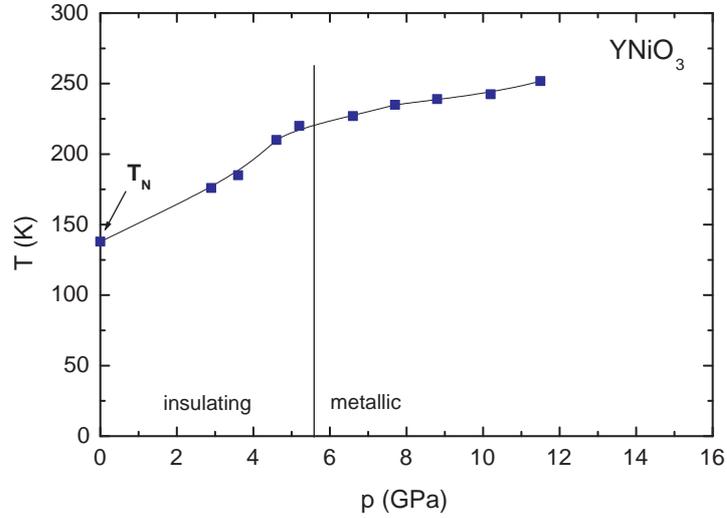
Figure 4.37: Pressure dependence of T_{max} of YNiO$_3$.

insulating state $(\partial T_{max}/\partial p \cong 16$ K·GPa$^{-1})$ is quite similar and can be explained in the same way as in the case of LuNiO$_3$ (see above).

4.6.2.2   EuNiO$_3$:

As we can not find any indication for T_N from our resistivity data in the case of EuNiO$_3$, we have performed high pressure measurements using ^{151}Eu nuclear forward scattering (NFS) spectroscopy of synchrotron radiation on EuNiO$_3$. This method has been introduced in section 3.2.5. It allows one to probe the magnetic state of the Ni sublattice under high pressure via the induced magnetic hyperfine (hf) field B_{ind} at the ^{151}Eu nuclei, which results from the ordered Ni ($3d$) moments. B_{ind} originates from the Ni−Eu exchange field due to the admixture of the excited Eu^{3+} states (e.g. $^7F_1$) into the nonmagnetic ground state ($^7F_0$) [122]. Some selected ^{151}Eu NFS spectra of EuNiO$_3$ collected at $T = 3$ K for different pressures (0; 9.4 and 14.4 GPa) are shown in Figure 4.38. The temperature dependence of NFS spectra measured at 9.4 GPa is displayed in Figure 4.38(b)[4].

---

[4]The fits to these spectra were performed using the program package CONUSS [123] by incorporating the full dynamical theory of nuclear resonance scattering, including the diagonalization of the complete hyperfine Hamiltonian.
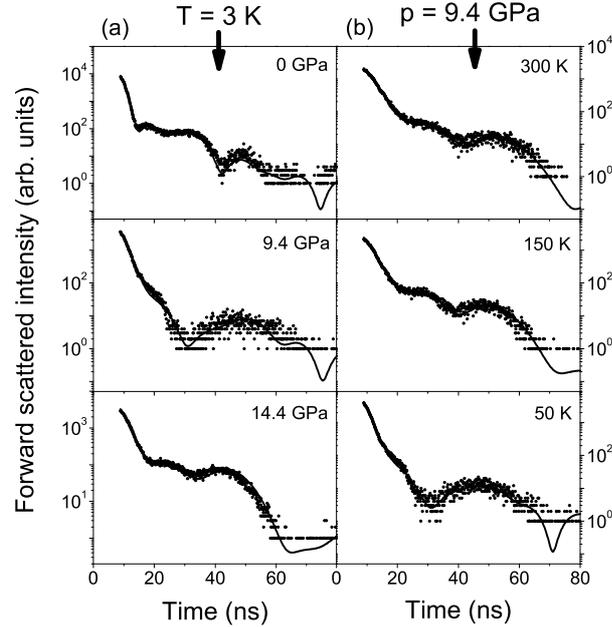
Figure 4.38: ^{151}Eu NFS spectra of EuNiO$_3$ (a) measured at $T = 3$ K and at pressures of 0; 9.4 and 14.4 GPa; and (b) measured at 9.4 GPa and at temperatures of 300, 150 and 50 K. The curves through the data points are fits (see the text).

At ambient pressure and at $T = 3$ K (see figure 4.38(a)), i.e. in the insulating state, the spectrum can be best fitted by assuming an induced hf field $B_{ind} = 1.4(2)$ T combined with a small quadrupole interaction ($\Delta E_Q = eQ_g V_{zz} = 6.0(4)$ mm/s), which is due to the orthorhombic point symmetry of the Eu lattice sites. The induced hf field is due to the Ni−Eu exchange field of the four parallel spins surrounding the Eu atoms as reported by neutron diffraction data on EuNiO$_3$ [100]. At 9.4 GPa and $T = 3$ K, i.e. in the metallic state, we find within the accuracy of measurements no significant change of the values of B_{ind} and eQV_{zz}. This clearly indicates that the metallic state at $p = 9.4$ GPa is magnetically ordered at $T = 3$ K. At 14.4 GPa ($T = 3$ K) no induced magnetic hf field could be detected, and only a quadrupole splitting is left, suggesting the disappearance of magnetic ordering between 9.4 and 14.4 GPa. In order to have an estimate of the transition temperature of the magnetically ordered state at 9.4 GPa, we have measured NFS spectra at different temperatures between 300 and 3 K (see figure 4.38(b)). The NFS spectra at 300 and 150 K could be fitted by assuming a pure quadrupole splitting, indicating a paramagnetic state. In contrast, for the analysis of the spectrum at 50 K we had to assume a combined quadrupole and magnetic hf interaction. We obtain values for $E_Q = 6.4(4)$ and $B_{ind} = 1.3(3)$ T, which are similar to those found at 3 K (see above). This indicates

that at 50 K the magnetically ordered state is nearly saturated. The analysis of
the temperature dependence of the spectra at 9.4 GPa shows that the transition
temperature is around 120 K, which is considerably lower than that at ambient
pressure ($T_N = 220$ K).

4.6.2.3   Pressure-temperature phase diagram of LuNiO$_3$ and EuNiO$_3$

Now we want to discuss the pressure-temperature phase diagram in RNiO$_3$ com-
pounds. Exemplary for this, we illustrate our data for LuNiO$_3$ and EuNiO$_3$ as
representative for the small and large RNiO$_3$, respectively.

(a) LuNiO$_3$:

Figure 4.39 displays the (p, T) phase diagram of LuNiO$_3$. Beside $T_{max}(p), T_N(p)$
and $T_{MI}(p)$, we plot the pressure dependence of the transition temperature (T_S) at
which the high temperature orthorhombic phase transforms to the monoclinic one.
These data are taken from high pressure - high temperature angle resolved x-ray
studies by Amboage [79].
As evident from the figure, T_{MI} and T_S have rather different pressure dependencies.
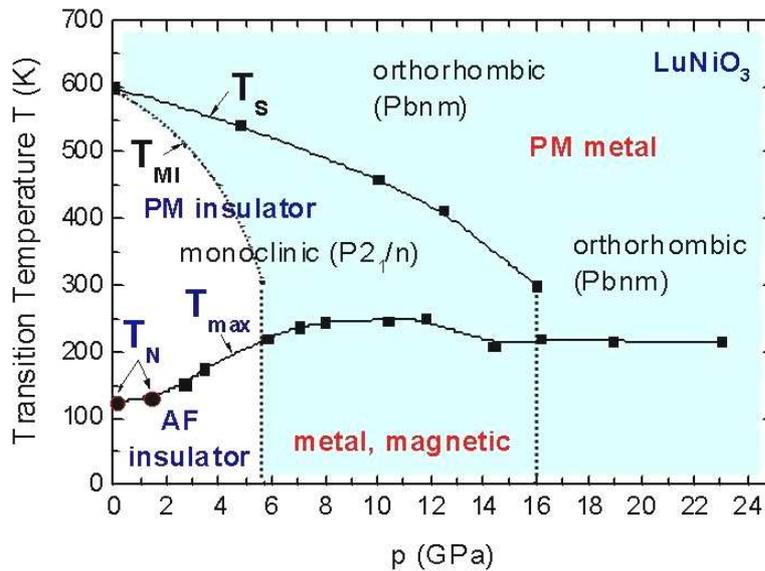
Figure 4.39: Proposed magnetic phase diagram for LuNiO$_3$ as deduced from our mea-
surements.

This means that their intimate connection at ambient pressure does not hold at high pressures, with the consequence that the metallic state exists in the monoclinic phase in which charge order exists. As shown from our neutron diffraction measurements on $LuNiO_3$ (section 4.5.3.2), the pressure-induced IM transition is driven by a partial melting of the charge ordering along the c-axis, while $LuNiO_3$ preserves its monoclinic structure.

As we mentioned in section 4.5.4.1, the pressure dependence of T_{max} which can be correlated to that of T_N can be divided into three regions. A large increase with pressure in the insulating phase ($0 < p < 5.8$ GPa), a moderate increase through a weak maximum in the metallic phase ($5.8 < p < 16$ GPa), and a very weak change above 16 GPa after the monoclinic-orthorhombic structural phase transition. Assuming that the antiferromagnetic ordering remains unchanged in the insulating and metallic states, one can qualitatively explain the different behavior of $T_N(p)$ to be due to different magnetic ground states in the insulating and metallic phase: exchange interactions of superexchange type in the insulating state and itinerant magnetism (e.g. spin density wave like) in the metallic phase [91]. At higher pressures ($p \gg 16$ GPa), one would expect a delocalization of the magnetic moment due to increasing the effective bandwidth of the Ni $3d$ states in $LuNiO_3$ as observed in $EuNiO_3$ at the QCP (see section 4.5.4.2). However, the occurrence of a structural phase transition at 16 GPa seems to help magnetism to survive up to 23 GPa.

(b) $EuNiO_3$:

Figure 4.40 shows a preliminary (p, T)-phase diagram for $EuNiO_3$. The pressure dependence of T_{MI} indicates the boarderline between the insulating and metallic state. The vertical part of the dotted line is located at the critical pressure (p_c = 5.8 GPa), above which the sample is in a metallic state at 4.2 K up to 300 K. The decrease of T_{MI} with pressure at temperatures above 300 K is assumed to be qualitatively similar to that measured in $SmNiO_3$ (see Figure 4.24).

Regarding the pressure dependence of T_N (as obtained from our NFS measurements, see section 4.5.4.2) we hardly can say anything about the initial change of T_N with pressure in the insulating phase. However, it is obvious that magnetic ordering exists in the metallic state (9.4 GPa) and that magnetism disappears at 14.4 GPa. This implies that the value of critical pressure corresponds to a QCP which is higher than 9.4 GPa, with an upper limit of 14.4 GPa. In this respect, we want to discuss the non-Fermi-liquid (NFL) behavior in $EuNiO_3$ near a QCP, i.e. in the pressure range $11.5 < p < 17.9$ GPa as obtained from our $R(p, T)$ data at low temperatures.

To analyze the data, we used the power-law fitting to $R(p, T)$ of $EuNiO_3$ in the temperature range between 10 and 45 K with $R(T) \sim T^n$, where $n = 2$ for Fermi-liquid (FL) and $1 < n < 2$ for NFL. As shown in Figure 4.41(a) the power-law with n = 1.6 fits the experimental data extremely well for $p = 11.5$; 13.2 and 14.8 GPa, whereas for 15.9 GPa the curve slightly deviates from the fit at low temperatures.
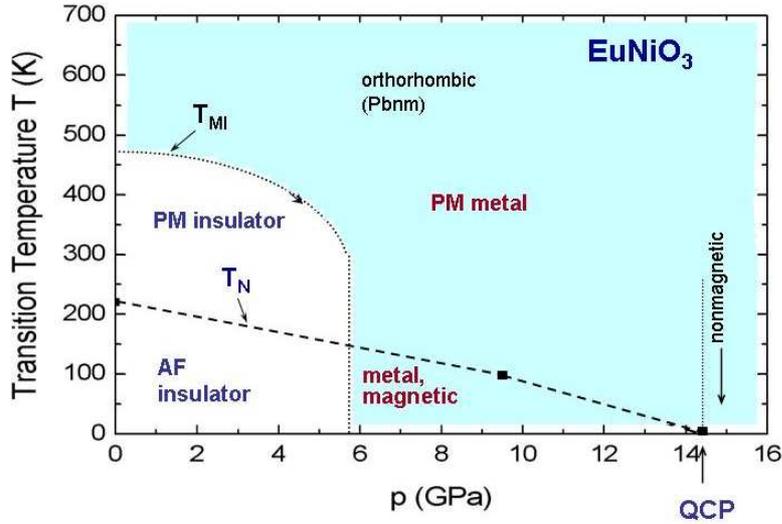
Figure 4.40: Preliminary (p, T) phase diagram for EuNiO$_3$

This indicates that an other exponent n should be used for $p \geq 14.8$ GPa. In Figure 4.41(b) we used the power-law fitting for $p = 15.9$ and 17.6 GPa and the best fitting is obtained with $n = 2$ (T^2-fit), suggesting a FL behavior, expected in the nonmagnetic state. Thus, these findings coincident with our observations of a nonmagnetic state at 14.4 GPa from the NFS measurements.

In the following we want to compare our results with those very recently reported on PrNiO$_3$ [10]. Zhou et al. [10] show that the suppression of the insulating state of PrNiO$_3$ above 1.3 GPa is accompanied by a transformation to a (NFL) phase in which the resistivity ρ varies proportional to T^n with $n \cong 1.33$ and 1.6 over a broad pressure range. They claim, that although a percolated NFL metallic phase may exist in the pressure range $0.8 < p < 1.3$ GPa, a bulk NFL phase may exist at higher pressures. Moreover, the step in the exponent n from 1.33 to 1.6 at 2.0 GPa remains a novel feature which needs theoretical attention.

Our finding of a NFL behavior in EuNiO$_3$ with $n = 1.6$ is consistent with that reported by Zhou et al. [10]. Since our QCP in EuNiO$_3$ is not precisely located, we can not check the possibility of such a step in the exponent n. However, in contrast to the observation of an extended NFL in PrNiO$_3$, we find a clear FL behavior in EuNiO$_3$ with orthorhombic symmetry already at pressures above the QCP ($p \geq$ 15.9 GPa). This last finding does not support the authors' suggestion [10] that a FL metallic phase can be only found in a perovskite structure with rhombohedral symmetry.
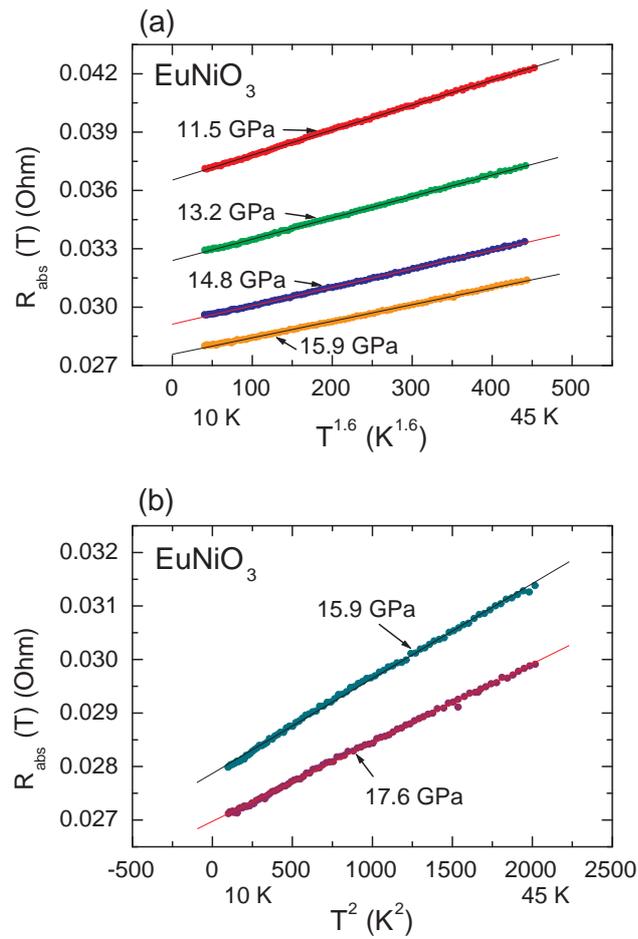
Figure 4.41: Electrical resistance of EuNiO₃ fitted with the power-law $R(T) \propto T^n$ between 10 and 45 K. (a) Fit with $n = 1.6$ between 11.5 and 15.9 GPa. (b) Fit with $n = 2$ at 15.9 and 17.6 GPa.

Chapter 5

High pressure studies on La$_{0.82}$Sr$_{0.18}$CoO$_3$

5.1 Basic properties of La$_{1-x}$Sr$_x$CoO$_3$ at ambient pressure

In the following we want to present the physical properties of the undoped perovskite-type LaCoO$_3$ which can also be described in an AMX$_3$ structure like the RNiO$_3$ perovskite compounds in chapter 4 (see Figure 4.1). All structural x-ray and neutron diffraction investigations on LaCoO$_3$ suggest a rhombohedral ($R\bar{3}c$) symmetry [124].

Considerable interest in LaCoO$_3$ originates from the puzzling nature of two transitions in this compound and the vicinity to a metal insulator transition. The existence of different spin-states in Co^{3+} which change with temperature is known since more than 50 years [125, 126]. These transitions can occur if the crystal-field energy Δ_{CF} and the intraatomic exchange energy J_{ex} (Hund's rule coupling) are comparable. The ground state of LaCoO$_3$ is nonmagnetic and insulating and no long-range magnetic order exists at all temperatures. At low temperatures ($T \approx$ 100 K) LaCoO$_3$ changes to a paramagnetic insulator and at $\approx$ 500 K it undergoes a temperature-induced semiconductor-metal transition. In Figure 5.1 we present the magnetic susceptibility $\chi(T)$ of LaCoO$_3$ as a function of temperature. The susceptibility shows a maximum at around 100 K and decreases Curie-like for temperatures $100 < T < 500$ K. Between 500 and 600 K, $\chi(T)$ shows a temperature-independent plateau which is ascribed to the insulator metal transition and above 600 K the measurement shows again a Curie-like decrease. The increase of the susceptibility below 30 K is attributed to magnetic impurities and/or oxygen nonstoichiometry [16].

Initially, the maximum of $\chi(T)$ at 100 K was attributed to a LS ($t_{2g}^6 e_g^0$, $S = 0$) to HS ($t_{2g}^4 e_g^2$, $S = 2$) transition [127, 17, 128, 129], in order to explain the insulating phase
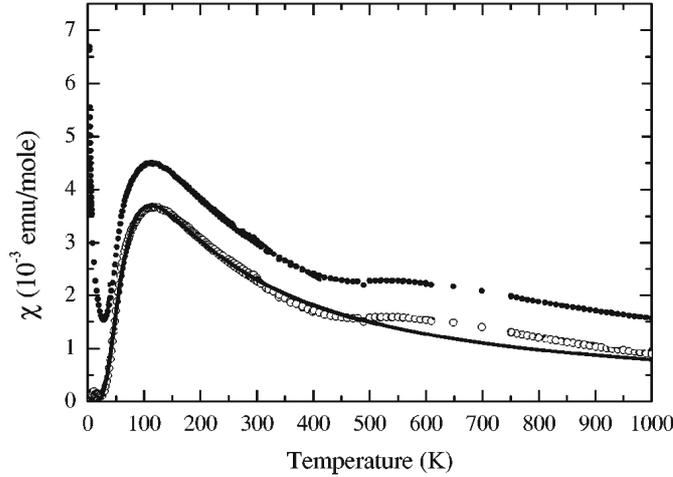
Figure 5.1: The black dotted line is the total, the open circles are Curie susceptibility ($\chi^C(T)$) of LaCoO$_3$. The maximum around 100 K signals the spin-state transition of the Co^{3+} ions. The increase of $\chi(T)$ below 30 K is probably due to magnetic impurities and/or oxygen nonstoichiometry. The solid line is a fit of $\chi^C(T)$ up to 400 K for a LS/IS scenario. Modified from [16].

up to 500 K (IM transition), whereas in more recent publications the scenario of an IS state ($t_{2g}^5 e_g^1$, $S = 1$) instead of HS has been proposed [130, 15, 131, 132, 133]. Also LDA+U calculations [14] favor the stabilization of the IS state due to large hybridization between Co-e_g and O-2p levels. This leads to a Jahn-Teller (JT) active IS state, caused by the partially filled e_g level. The degeneracy of the e_g orbitals of Co^{3+} ions in the LS state is then expected to be lifted in the IS state by a JT distortion. Within this scenario the existence of orbital ordering and its melting have been proposed to explain the insulating nature below 500 K and the IM transition, respectively [14]. However, the nature of these transitions is still unclear and controversial discussed.

Another aspect of cobaltates which is controversially discussed is the effect of charge-carrier doping. This can be achieved by substitution of La^{3+} by R^{2+} rare earth ions, with e.g. R = Ba, Ca or Sr. It is generally accepted that for example replacing of La^{3+} by Sr^{2+} creates formally Co^{4+} ions and that the double exchange between Co^{4+} and the remaining Co^{3+} leads to a ferromagnetic coupling [19, 22].

In the following we want to consider the properties of LaCoO$_3$ by doping with Sr^{2+} ions. It has been found in La$_{1-x}$Sr$_x$CoO$_3$ that with increasing x the LS ground state is rapidly suppressed. For small x a spin-glass like behavior has been observed at low temperatures, whereas for $x \geq 0.18$ a ferromagnetic order has been found (see Figure 5.2) [17, 134]. On the other hand, the electrical resistivity decreases with
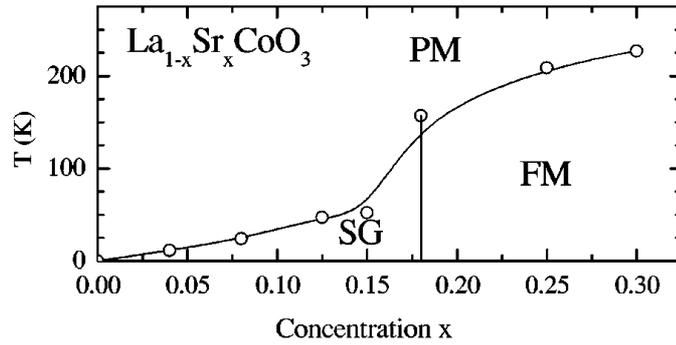
Figure 5.2: Magnetic phase diagram of La$_{1-x}$Sr$_x$CoO$_3$. PM, FM and SG are the abbreviations for paramagnetic, ferromagnetic and spin-glass phase. Taken from [21].

increasing Sr^{2+} content and for $x \approx 0.20$ the samples show a metallic temperature dependence of the resistivity over the entire temperature range [18, 19, 20, 21]. For x = 0.18, 0.25 and 0.3 $\rho(T)$ shows a distinct anomaly near the critical temperatures of ferromagnetic order. This is illustrated in Figure 5.3 for $0 < x < 0.3$. Furthermore, the rhombohedral distortion decreases with increasing x and at about $x \approx 0.5$ the structure becomes nearly cubic.
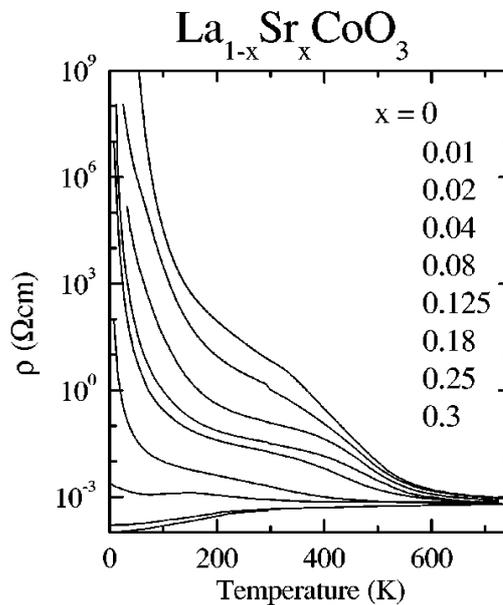
Figure 5.3: Electrical resistivity as a function of temperature for La$_{1-x}$Sr$_x$CoO$_3$ for different Sr^{2+} concentrations. Taken from [21].
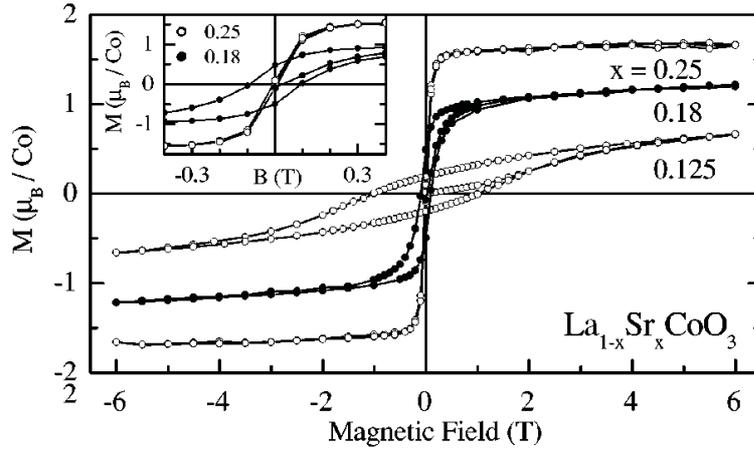
Figure 5.4: Magnetization curves of $La_{1-x}Sr_xCoO_3$ vs. magnetic field for $x = 0.125$; 0.18 and 0.25 at 4 K. Inset: zoomed view of the low field region, showing that the hysteresis for $x = 0.18$ and 0.25 is very small. Taken from [21].

In Figure 5.4 we present the magnetization measurement on $La_{1-x}Sr_xCoO_3$ at 4 K for $x = 0.125$; 0.18 and 0.25 as a function of applied magnetic field. The shape of the curve changes as a function of Sr^{2+} doping. Whereas the sample with the lowest Sr concentration shows a broad hysteresis, the hysteresis for $x = 0.18$ and 0.25 decreases with increasing x. The inset of Figure 5.4 displays the tiny hysteresis for $x = 0.18$ and 0.25. Furthermore, the latter two concentrations show a steep change of $M(B)$ around the coercive field. Beyond that, the sample with $x = 0.25$ seems to be saturated in a field of 6 T with a value of 1.65 μ_B/Co-atom. However, it is not clear which spin-states are present and whether or not spin-state transitions take place as a function of temperature in the Sr-doped systems [135, 136, 137]. Only the magnetization measurements $M(T)$ on $La_{1-x}Sr_xCoO_3$ with very low doping ($x < 0.01$) provide information about a change of the spin-state, whereas for larger doping the $M(T)$ curves will be dominated by the occurrence of spin-glass and ferromagnetically ordered phases [21].

From the measured value of 1.65 μ_B/Co of the saturation magnetization in the ferromagnetic phase ($x = 0.25$) the authors were able to fit their value best to the expected average spin-only value (S_{avg}) of 1.75 μ_B/Co assuming Co^{4+} LS ($t_{2g}^5 e_g^0$) and Co^{3+} IS ($t_{2g}^4 e_g^1$) states. This value has been obtained by using a simple model to calculate the average spin-state[1] in $La_{1-x}Sr_xCoO_3$ assuming: (a) a spin-only behavior of the sample, (b) an homogeneous distribution of Co^{3+} and Co^{4+} ions (i.e. no generation of spin clusters) and (c) linear dependence of spin and concentration

---

[1]I.e. for $La_{1-x}Sr_xCoO_3$ with $x = 0.25$ Sr concentration one obtains: with $\mu_S = 2 \cdot S_{avg} \Rightarrow S_{avg} = (S^{3+} + x(S^{4+} - S^{3+}))$, with $S^{3+} = Co^{3+}$ IS ($S = 1$) and $S^{4+} = Co^{4+}$ LS ($S = 1/2$) one obtains: $(1 + 0.25(1/2 - 1)) = 0.875 \Rightarrow \mu_S = 2 \cdot S_{avg} = 1.75$ μ_B/Co-atom which close to the 1.65 μ_B/Co deduced from the magnetization measurement.

x. The configuration of these spin-states (Co^{3+} IS and Co^{4+} LS) realizes the importance of the double exchange mechanism and the similarities to the manganites since the spin-states differ only by two additional down-spin electrons in the t_{2g} level from the corresponding HS state of Mn^{4+} ($t_{2g}^3 e_g^0$) and Mn^{3+} ($t_{2g}^3 e_g^1$). However, little is known about the correlation between the spin- and charge degree of freedom near the MI transition, i.e. whether and to what extent these spin-state transitions affect the MI transition.

To clarify these open questions we have investigated the effect of pressure on the electronic, magnetic, and structural properties of a conducting, ferromagnetic single crystal of La$_{1-x}$Sr$_x$CoO$_3$ with $x = 0.18$, which is located near the boundary of the MI transition. For that purpose, we performed electrical resistivity, x-ray diffraction, magnetization and inelastic x-ray emission spectroscopy measurements under high pressure. All results are presented and discussed in the following section of this chapter.

5.2 Results on La$_{0.82}$Sr$_{0.18}$CoO$_3$

5.2.1 Pressure-induced metal insulator transition

This chapter presents the experimental results on La$_{1-x}$Sr$_x$CoO$_3$ ($x = 0.18$) single crystal perovskite compound. The crystals were created by T. Lorenz et al. (II. Physikalisches Institut, University of Cologne), their preparation is described elsewhere [21]. In the following we first consider the electrical resistance.

5.2.1.1 Pressure dependence of the electrical resistivity

We measured the pressure dependence of the electrical resistivity of a $25 \times 140 \times 280$ μm^3 single crystal La$_{0.82}$Sr$_{0.18}$CoO$_3$ up to 14 GPa by conventional four-terminal method between 4.2 K $\leq T \leq$ 300 K in a Bridgman-type high pressure cell (large volume high pressure cell) which has been described in chapter 3.2.

In Figure 5.5(a) we display $\rho(p, T)$ at different pressures up to 5.7 GPa. With increasing pressure the electrical resistivity increases dramatically by about 4 orders of magnitude, indicating a strong reduction of electron hopping with increasing pressure (e.g. ρ at 4.2 K increases from 0.2 mΩcm ($p = 0$ GPa) to 4.6 Ωcm ($p = 5.7$ GPa)). No further increase of $\rho(T)$ for pressures above 5.7 GPa was observed; instead of this, we find a decrease of $\rho(T)$ by about 30% at 14 GPa and $T = 4.2$ K
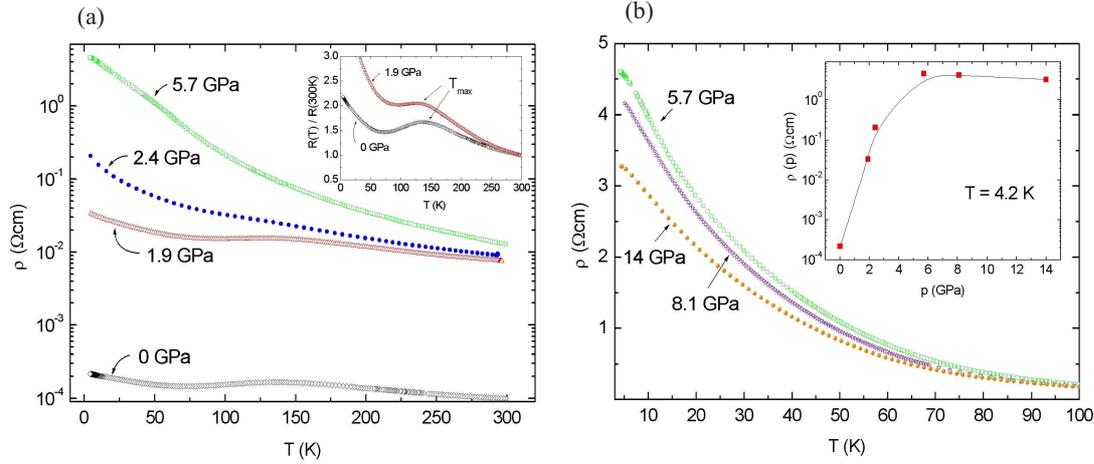
Figure 5.5: Temperature dependence of the electrical resistivity of $La_{1-x}Sr_xCoO_3$ with $x = 0.18$. (a) $\rho(p, T)$ for pressures up to 5.7 GPa. The inset presents the shift of the maximum in $\rho(T)$ which is related to T_C. (b) $\rho(p, T)$ for pressures between 5.7 and 14 GPa. The inset shows the values of $\rho(p)$ at $T = 4.2$ K as a function of pressure in the whole pressure range.

compared with the corresponding value at 5.7 GPa (Figure 5.5(b)). The inset of Figure 5.5(b) shows the two regions of the pressure dependence of $\rho(p)$ at 4.2 K between 0 and 14 GPa. In the first range up to 5.7 GPa, $\rho(p)$ strongly increases whereas in the second one above 5.7 GPa the resistance seems to saturate, indicating two different scattering mechanisms (see below).

As shown in the inset of Figure 5.5(a), the $\rho(T)$-curve at ambient pressure shows a local maximum at a temperature $T_{max} \approx 138$ K which is slightly below the transition temperature T_C to a ferromagnetic state[2]. We find that under pressure the maximum of $\rho(T)$ (T_{max}), which is correlated to T_C, shifts to lower temperatures. We obtain a decrease of T_{max} of about -8 K between $p = 0$ and 1.9 GPa[3]. Under the assumption that this decrease of T_{max} is equal to that of T_C, we estimate a pressure-induced relative decrease of T_C which amounts to $\partial \ln T_C / \partial p \approx -2.6 \times 10^{-2}$ GPa^{-1}.

The observation of a strong increase of the electrical resistivity (i.e., suppression of electron hopping), and the reduction of T_C with increasing pressure is unexpected and opposite to results reported on related transition metal oxides, e.g. $La_{1-x}Sr_xMnO_3$ [3] and $La_{1-x}Sr_xFeO_3$ [5]. For example, in $La_{0.85}Sr_{0.15}MnO_3$ (see Figure 5.6) one finds an enhancement of electron hopping with increasing pressure

---

[2]$T_C \approx 157$ K (at ambient pressure) as deduced from magnetization measurements [21].
[3]By estimating the first derivative of $\rho(T)$, where $\partial \rho(T)/\partial T = 0$.

that stabilizes the ferromagnetic metallic state via double exchange. The relative increase of T_C with pressure in this system amounts to $\partial\ln T_C/\partial p \approx +6.4 \cdot 10^{-2}$ GPa^{-1}.
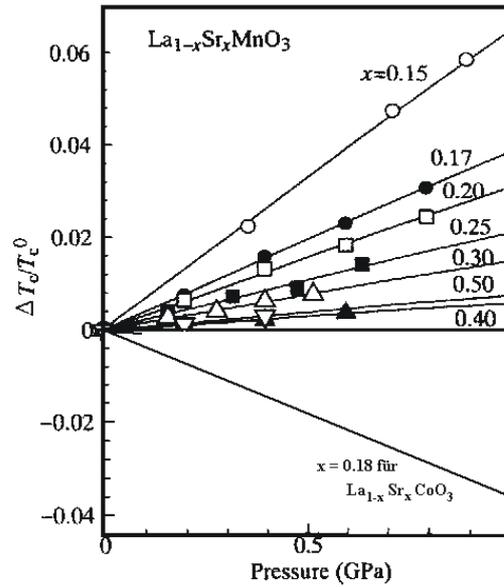
Figure 5.6: Pressure dependence of $T_C(p)$ in $La_{1-x}Sr_xMnO_3$ as deduced from [3] and $La_{1-x}Sr_xCoO_3$ with $x = 0.18$ (present work). Note the opposite pressure dependence of T_C in $La_{1-x}Sr_xCoO_3$ ($x = 0.18$).

5.2.1.2 Crystal structure under pressure

In the following we want to find out if the pressure-induced MI transition is connected with a structural phase transition. For this purpose, we have performed high pressure energy dispersive x-ray diffraction measurements on $La_{0.82}Sr_{0.18}CoO_3$ using synchrotron radiation at beamline F3 at Hasylab (Hamburg).

In Figure 5.7(a) we present the pressure dependence of the lattice parameters (a, c) of the hexagonal unit cell at 300 K up to 25.5 GPa. Within the error bars, we find
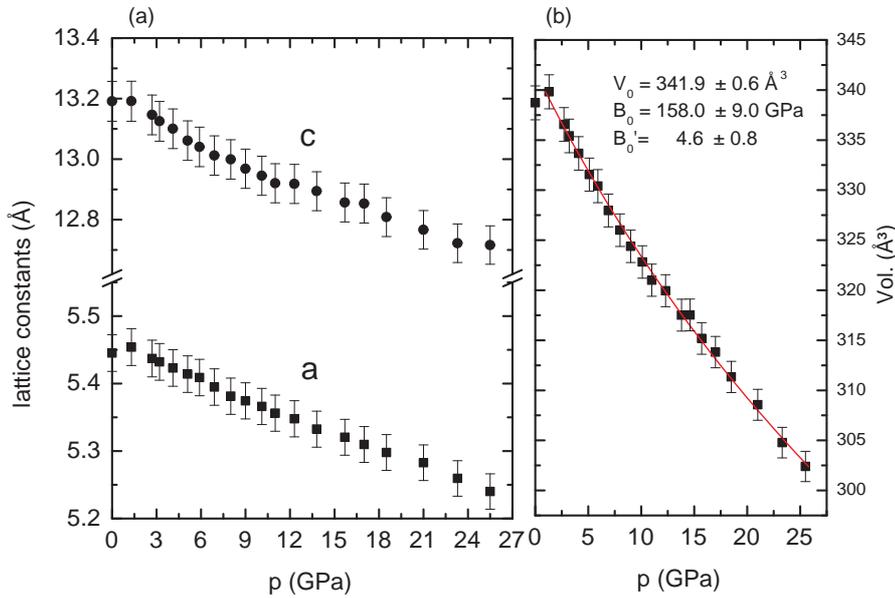
Figure 5.7: (a) Pressure dependence of the (a, c)-lattice parameters of $La_{1-x}Sr_xCoO_3$ $(x = 0.18)$ at room-temperature as obtained from our energy dispersive synchrotron x-ray diffraction measurements. (b) Fit to the volume of the Birch-Murnaghan equation of state. The errors for the pressure in (a) and (b) are about $\pm$ 0.25 GPa for each measurement.

no discontinuity in the lattice parameters or in the volume (Figure 5.7(b)); thus, no indication of a structural phase transition.
We also fitted the volume to the Birch-Murnaghan equation of state and obtained for the bulk modulus $B_0 = 158(9)$ GPa and its derivative $B_0' = 4.6(0.8)$. These values are close to those found for $LaCoO_3$ ($B_0 = 150(2)$, $B_0' = 4$) [138]. This result indicates that the pressure-induced MI transition is not caused by a structural phase transition.

5.3   Discussion: Mechanism of the pressure-induced metal insulator transition

In the following we want to find an explanation for the suppression of the electron hopping and the reduction of T_C. Two possible explanations for this unusual behavior will be discussed: 1. a pressure-induced unusual change of the Co-O-Co bond angle and Co-O bond length or 2. a change of the Co^{3+} spin-state under pressure.

5.3.1   Change of structural parameters under pressure

Unfortunately, it was not possible from our x-ray diffraction measurement to deduce any information about the Co-O bond length as well as of the Co-O-Co bond angle. For these information we have to regard high resolution angle dispersive x-ray diffraction measurements on $LaCoO_3$ under pressure in Figure 5.8 (a,b) [138]. In their paper the authors show that with increasing pressure (a) the Co-O bond length decreases more rapidly than that of La-O which results (b) in an huge opening of the Co-O-Co bond angle from $166°$ to $177°$ at 4 GPa. Such an increase of the bond angle with increasing pressure is the usual structural response of transition metal oxides with perovskite structure and results in an enhanced electron hopping and stabilizing of the metallic state. But we find in $La_{0.82}Sr_{0.18}CoO_3$ under pressure exactly the opposite behavior. Therefore, one has to discuss another explanation which is not based on structural changes, namely the possibility of a pressure-induced spin-state transition from the magnetic IS Co^{3+} state to a nonmagnetic LS state.

This is based on two experimental facts: (i) the ionic radius of LS Co^{3+} (0.545 Å) is smaller than that of HS/IS Co^{3+} (0.61 Å) [23], (ii) the crystal field splitting Δ_{CF}
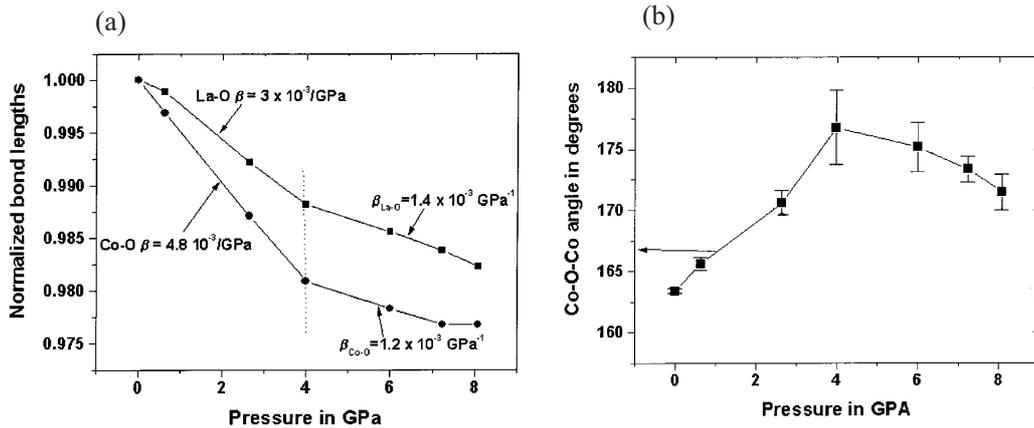
Figure 5.8: Pressure dependence of (a) the normalized La-O and Co-O bond length and (b) of the Co-O-Co bond angle on $LaCoO_3$. Both figures deduced from [138].

of $LaCoO_3$ is found to increase remarkably with increasing pressure [139]. This is clearly seen in Figure 5.9 which shows the temperature dependence of the susceptibility of $LaCoO_3$ as a function of pressure up to 1.8 GPa [139]. The increase of the spin-state transition temperature with increasing pressure is evident and reveals a large increase of the energy gap between the LS ground state and the excited magnetic IS(HS) state. This means that pressure causes a continuous population of the LS state at the expense of depopulation the IS state. A consequence of such a depopulation of the magnetic IS state to a nonmagnetic LS state would be a reduction of the Co magnetic moment with increasing pressure. In the following we will discuss our experimental results which provide evidence for a pressure-induced spin transition.
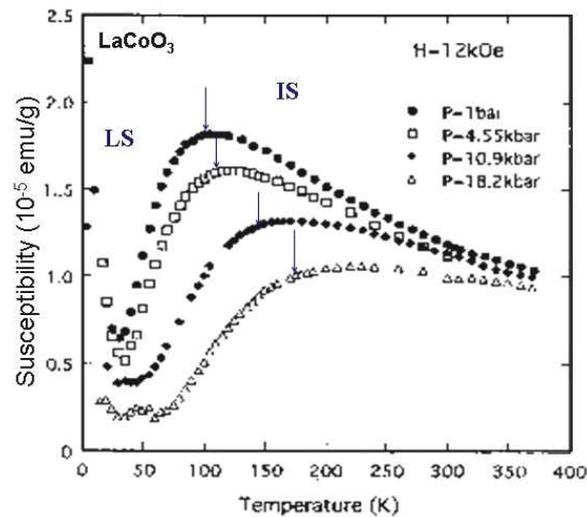
Figure 5.9: Susceptibility of $LaCoO_3$ under pressure. With increasing pressure the energy gap between LS and IS increases [139]. Thus, the IS will be depopulated under pressure and LS state will be more populated.

5.3.2   Change of Co^{3+} spin-state under pressure

5.3.2.1   Effect of pressure on the Co magnetic moment

To verify that pressure suppresses the magnetic IS state to a nonmagnetic LS state, we have performed measurements of the saturation magnetization of Co (μ_{Co}) in $La_{0.82}Sr_{0.18}CoO_3$ in an external magnetic field of 2 T at ambient pressure and 1.0 GPa as shown in Figure 5.11 by using the pressure cell described in chapter 3.4. We experimentally find a decrease of μ_{Co} of 5.4(2) % at lowest temperatures between ambient pressure and 1.0 GPa. Under the assumption that μ_{Co} decreases linearly, this reduction from 1.11(1) μ_B at $p = 0$ GPa to 1.05(1) μ_B at 1.0 GPa signifies a reduction of at least 30 % at 5.7 GPa.
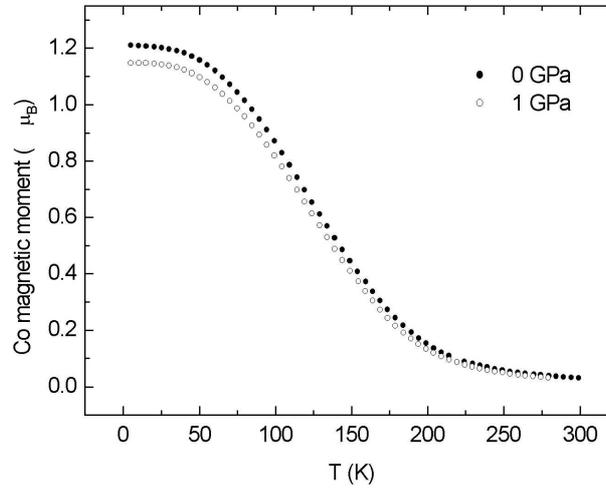
Figure 5.10: Temperature dependence of the Co magnetic moment of $La_{0.82}Sr_{0.18}CoO_3$ in an external magnetic field of 2 T at ambient pressure and 1.0 GPa as deduced from magnetization measurements.

Additionally, we find a reduction of T_C of ≈ -4 K/GPa. This is in accordance to that value, obtained from our resistivity data above. Thus, the decrease of T_C with increasing pressure is a consequence of the suppression of the Co magnetic moment. These findings strongly support our suggestion of a pressure-induced change of the Co spin-state (from magnetic IS to nonmagnetic LS in $La_{0.82}Sr_{0.18}CoO_3$).

Since these measurements only *support* our interpretation of the pressure-induced spin-state transition, we further apply a spectroscopic method which can give a clear microscopic evidence of our statement. This evidence (see section 5.3.2.2) was brought by the inelastic x-ray emission spectroscopy, introduced in chapter 3.2.5.

5.3.2.2 Microscopic evidence for a pressure-induced spin-state transition

The aim of the experiment was the investigation of the Co spin-state as a function of pressure in $La_{0.82}Sr_{0.18}CoO_3$ in order to explore the mechanism behind the pressure-induced metal-insulator (MI) transition. The investigations were carried out using inelastic x-ray emission spectroscopy (XES) at the Co K β ($3p \rightarrow 1s$) line. The experiment was performed at beamline ID16 at ESRF as described in chapter 3.2.4.

Figure 5.11 shows the Co K β x-ray emission spectra of $La_{0.82}Sr_{0.18}CoO_3$ for pressures between 0 and 14.4 GPa at 300 K. All spectra are normalized to the transmitted intensity and also shifted so that the peak of the Co K $\beta_{1,3}$ main emission line is set to 7.65 keV. As mentioned in chapter 3.2.4, the magnetic state of Co is characterized by the appearance of the satellite emission peak (K β') located at the lower energy region of the main emission peak (K $\beta_{1.3}$), which is a result of the $3p \rightarrow 3d$ core-hole exchange interaction in the final state of the emission process. As shown in Figure 5.11, we find a gradual decrease of intensity of the satellite peak with increasing pressure, i.e. a transfer of spectral weight from the satellite to the main peak. This indicates a gradual reduction of the spin moment with pressure, reaching nearly a LS at 14.4 GPa.
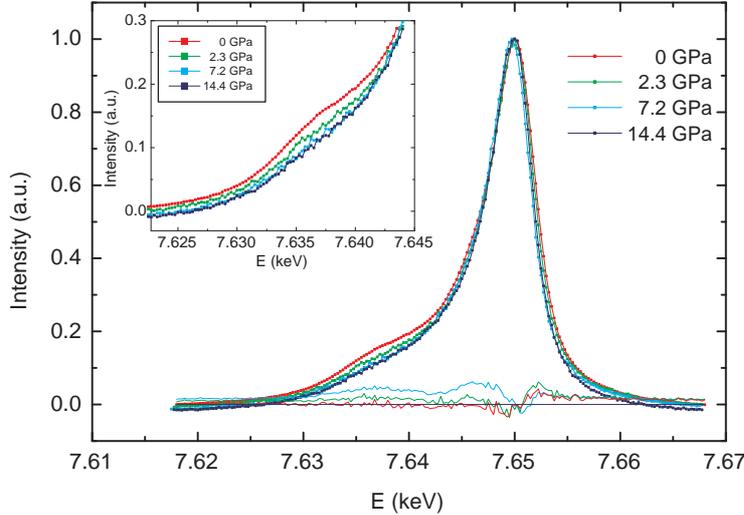
Figure 5.11: K β emission spectra of $La_{0.82}Sr_{0.18}CoO_3$ at 300 K as a function of pressure. The curves below the XES spectra are the difference spectra with respect to the spectrum at 14.4 GPa. The inset shows the gradual decrease of the intensity of the satellite peak with increasing pressure due to IS/HS $\rightarrow$ LS transition.

To extract quantitative information from the XES data, the emission spectra were analyzed with the help of the empirical "sum-rule" that was recently derived [140, 141]. The sum-rule relates the integrated absolute difference (IAD) signal to the spin-state of the transition-metal atom, according to

$$IAD = \int I_{XES}(T, p, \hbar\omega) - I_{XES}(T_0, p_0, \hbar\omega)d\hbar\omega, \qquad (5.1)$$

where the difference is taken between a reference spectrum I_{XES} (denoted with the 0 subscript) and another spectrum at a given temperature T and pressure p.

Figure 5.12 presents the IAD analysis for $La_{0.82}Sr_{0.18}CoO_3$ at $T = 300$ K. The y-scale indicates the IAD value, which does not refer directly to the spin state. A quantitative analysis compares these values with model compounds and calculations in a second step [140, 141]. Our aim is to qualitatively show that the application of pressure on $La_{0.82}Sr_{0.18}CoO_3$ results in a pressure-induced IS/HS $\rightarrow$ LS transition.
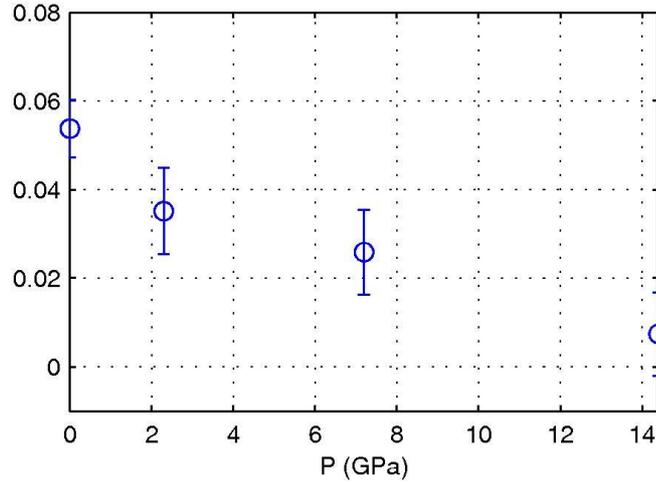
Figure 5.12: IAD signal of $La_{0.82}Sr_{0.18}CoO_3$ at $T = 300$ K as a function of pressure.

We find between 0 and 14.4 GPa a decrease of the IAD signal from 0.055 to ~ 0.008. The gradual decrease of the IAD signal corresponds to a gradual population of the LS state at the expense of the IS/HS state, due to the increase of the crystal-field splitting. As a result, under pressure the LS state will be favored. The consequence of this transition to the LS state has been observed in our resistivity data on $La_{0.82}Sr_{0.18}CoO_3$ (see Figure 5.5(a)), where a strong suppression of the electron hopping is observed under pressure.

Thus, we find for the first time a microscopic evidence for a spin-state transition in $La_{0.82}Sr_{0.18}CoO_3$ from IS/HS $\rightarrow$ LS with increasing pressure which is apparently the driving mechanism of the pressure-induced MI transition.

5.3.2.3 Qualitative model: Effect of the spin-state transition on electron hopping

In the following we briefly introduce a qualitative model explaining why such a spin-state transition results in a suppression of electron hopping. If we assume, that at ambient pressure the $La_{0.82}Sr_{0.18}CoO_3$ ground state is a mixture of IS Co^{3+} and LS Co^{4+} ions, the conduction occurs predominantly by hopping of an e_g electron from Co^{3+} ($t_{2g}^5 e_g^1$) to Co^{4+} ($t_{2g}^5 e_g^0$). This transport process can also account for the magnetic coupling of the localized t_{2g} electrons (double exchange), which results in a ferromagnetic conducting state. This is schematically illustrated in Figure 5.13.
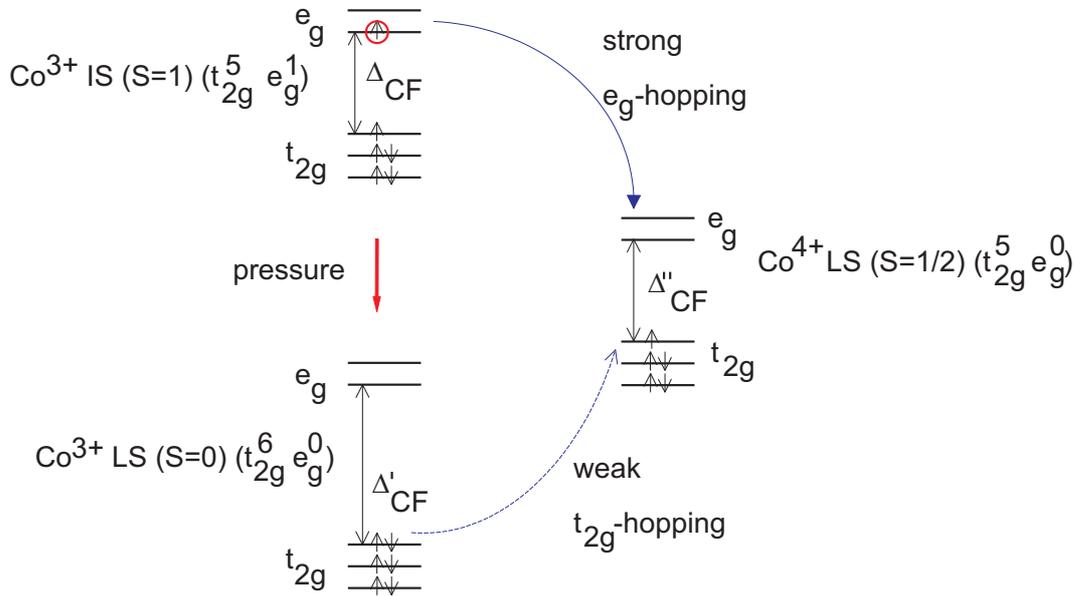
Figure 5.13: Schematic representation of the interplay between spin-state and electron hopping in $La_{0.82}Sr_{0.18}CoO_3$: at ambient pressure conductivity occurs by hopping of an e_g electron from IS Co^{3+} to LS Co^{4+}. With increasing pressure, the crystal-field splitting Δ_{CF} of IS Co^{3+} increases ($\Delta'_{CF} > \Delta_{CF}$) [139]. Consequently, the IS Co^{3+} will be gradually depopulated and the ground state of Co^{3+} is then predominantly a LS state. As a result, the strong e_g hopping between Co^{3+} and Co^{4+} is strongly suppressed and only a weak t_{2g} hopping remains.

The increasing energy of the crystal-field splitting due to the increase of external pressure, leads to a gradual depopulation of the IS Co^{3+} state and its crossover to the LS Co^{4+} state. At sufficiently high pressures, e.g. $p = 5.7$ GPa, the IS state will be mostly depopulated and a large part of the Co^{3+} ground state shows predominantly

a LS ($t_{2g}^6 e_g^0$) configuration. As a result, the strong Co^{3+} to Co^{4+} hopping of an e_g electron would be strongly suppressed and consequently, only a weak t_{2g} hopping from LS Co^{3+} to LS Co^{4+} would remain. Thus, the gradual depopulation of the IS Co^{3+} state with increasing pressure can explain the observed suppression of electron hopping in $La_{0.82}Sr_{0.18}CoO_3$.

It has to be mentioned here, that the effect of the pressure-induced IS to LS transition on the electron hopping prevails over the opposite effect of an increase of the Co-O-Co bond angle with increasing pressure [138]. This clearly shows that the strong correlation between the spin-state and charge degrees of freedom in $La_{0.82}Sr_{0.18}CoO_3$ dominates the pressure-induced MI transition.

Finally, we give an explanation for the reduction of $\rho(p,T)$ in $La_{0.82}Sr_{0.18}CoO_3$ for pressures $5.7 \leq p \leq 14$ GPa which has been shown in Figure 5.5(b). As mentioned above, $\rho(p,T)$ decreases by about 30 % at lowest temperatures which can be explained in the following way: above 5.7 GPa the majority of the Co^{3+} is already transformed from IS to the LS state, so that this mechanism is not efficient anymore and the usual way due to broadening of the effective bandwidth with increasing pressure prevails. This leads to the usual decrease of the electrical resistivity with increasing pressure.

Chapter 6

Summary and Outlook

This thesis describes the effect of external pressure on the electronic, magnetic and structural properties of two novel types of transition metal oxides ($RNiO_3$ and $(La,Sr)CoO_3$). Special emphasis was given to the investigation of the influence of charge ordering, spin-state transition, magnetic ordering and structure on the electrical transport and in particular on the mechanism of the metal insulator (MI) transition.

$RNiO_3$ (R = rare earth) perovskites offer an excellent opportunity to investigate the MI transition, as being stoichiometric (undoped) Mott-insulators. The transition temperature (T_{MI}) of the thermally-induced MI transition increases with decreasing size of the R^{3+} ions (T_{MI} = 130 K (Pr), ..., 600 K (Lu)); for R = La the system remains metallic down to lowest temperatures. The transition from the metallic to the insulating state is connected with a structural phase transition (orthorhombic $\rightarrow$ monoclinic), which implies the presence of charge ordering of the Ni^{3+} ions in the monoclinic insulating phase. Another interesting aspect is the evolution of the magnetism from enhanced Pauli paramagnetism in $LaNiO_3$ to Curie-Weiss paramagnetism with decreasing size of R^{3+}; where the compounds with R = Sm $\rightarrow$ Lu exhibit antiferromagnetic ordering with a Néel temperature $T_N < T_{MI}$. This indicates a crossover from antiferromagnetic insulator (R $\neq$ La) to nonmagnetic metal (R = La) through a quantum critical point (QCP).
In order to shed light on the interplay between charge ordering, local structure, magnetic ordering and the evolution of the metallic state in $RNiO_3$ series, we investigated the effect of pressure on the transport, magnetic and structural properties of selected $RNiO_3$ compounds (R = Sm, Eu, Y and Lu) using different pressure experimental methods. Pressure dependent electrical resistance measurements reveal in all these $RNiO_3$ compounds a pressure-induced insulator metal (IM) transition between 5 and 7 GPa. High pressure x-ray diffraction measurements on these compounds show that the IM transition is not connected with a structural phase transition (monoclinic $\rightarrow$ orthorhombic). To solve the puzzle of the observed pressure-induced metallic state in a monoclinic structure, in which a charge ordered state exists, we

have performed high resolution neutron diffraction measurements on $LuNiO_3$ under high pressure. Analysis of the bond length of the two Ni-sites (Ni1 and Ni2) which form the $Ni1O_6$ and $Ni2O_6$ octahedra, respectively, reveals that the bond lengths along the c-axis (d_{Ni1-O1} and d_{Ni2-O1}) become nearly equal at 6 GPa. This results in a partial melting of the charge ordering along the c-axis and triggers the IM transition with increasing pressure.

Since charge ordering has been also observed in larger $RNiO_3$ compounds (R = Y → Nd), this mechanism could be responsible for the observed pressure-induced IM transition in these compounds as well. However, further high pressure neutron studies are required to check if this mechanism holds for the $RNiO_3$ series.

On the other hand, we have investigated the effect of pressure on the magnetic state of $EuNiO_3$ ($T_N = 220$ K and $T_{MI} = 463$ K) using ^{151}Eu nuclear resonance scattering of synchrotron radiation. We show that the pressure-induced metallic state exhibits magnetic ordering, which disappears between 9.4 and 14.4 GPa. Analysis of the temperature dependence of the electrical resistance in this pressure region reveals non-Fermi-liquid behavior for $11.5 \leq p \leq 14.8$ GPa and Fermi-liquid behavior for $p > 15.9$ GPa reflecting the proximity of the system to a magnetic QCP. Finally, pressure-temperature phase diagrams for $EuNiO_3$ and $LuNiO_3$ are proposed.

It is highly desired to investigate the pressure dependence of T_N in the insulating and metallic phases of these compounds and to determine the critical pressure at the magnetic QCP in $EuNiO_3$ and other $RNiO_3$ compounds. Also information on the magnetic structure of the pressure-induced metallic state would be of great interest. Such studies are presently in progress.

The second investigated system, $(La,Sr)CoO_3$, belongs to the transition metal oxides containing Co^{3+} ions, which possess, in addition to the usual charge, orbital and spin (up/down) degrees of freedom, the possibility to change the spin-state of the Co^{3+} ion. The ground state of the undoped, insulating system $LaCoO_3$ is the low-spin configuration (LS), $S = 0$ and this can be thermally excited to either a high-spin (HS), $S = 2$ or an intermediate spin-state(IS), $S = 1$. The addition of charge carriers establishes a ferromagnetic, metallic state by $x \geq 0.18$. The conductivity and ferromagnetic coupling are suggested to be related to the double exchange of LS Co^{4+} and IS Co^{3+} ions in the doped samples. However, the correlation between the spin and charge degrees of freedom near the MI transition is far from being clear.

In order to explore whether and to what extend the spin degree of freedom affects the MI transition, we have performed high pressure experiments on a single crystal of conducting, ferromagnetic $La_{0.82}Sr_{0.18}CoO_3$ sample located near the boundary of the MI transition. High pressure electrical resistivity and x-ray diffraction measurements $p \geq 5.7$ GPa reveal a quite unusual effect: a transition from the conducting to an insulating state and a reduction of the magnetic ordering temperature (T_C) with increasing pressure, while the lattice structure remains unchanged up to $\sim$

25 GPa. This rather unique effect is opposite to that observed in other related systems ($La_{1-x}Sr_xMnO_3$, $La_{1-x}Sr_xFeO_3$ and $RNiO_3$) and is apparently connected with a different physical mechanism. To provide an explanation for the pressure-induced insulating state, we have considered the possibility of a pressure-induced spin-state transition from the magnetic IS Co^{3+} state to a nonmagnetic LS state which can be driven by an increased crystal field splitting at high pressure. To verify this explanation we first investigated the effect of pressure on the Co saturation moment (μ_{Co}) in $La_{0.82}Sr_{0.18}CoO_3$ using magnetization measurements up to 1 GPa. We find a decrease of μ_{Co} of about 6 % which corresponds to a decrease of μ_{Co} by more than 30 % at 5.7 GPa, supporting our suggestion of a pressure-induced IS to LS transition in $La_{0.82}Sr_{0.18}CoO_3$.

To obtain microscopic evidence for the pressure-induced IS $\rightarrow$ LS transition, we have directly investigated the change of the spin-state with pressure up to $\sim$ 14 GPa in $La_{0.82}Sr_{0.18}CoO_3$ using x-ray emission spectroscopy (Co K β emission spectrum). The analysis of the K β emission spectra on $La_{0.82}Sr_{0.18}CoO_3$ clearly shows a gradual change of the spin-state from IS or HS state to a LS state. Such a microscopic evidence for a spin-state transition in $La_{0.82}Sr_{0.18}CoO_3$ indicates that the observed pressure-induced MI transition is driven by a simultaneous spin-state transition.

Beyond that, it would be interesting to investigate the influence of spin-state transitions on the electrical transport in other classes of Co-based transition metal oxides such as $La_{2-x}Sr_xCoO_4$ and $RBaCo_2O_{5+\delta}$ with ($0 \leq \delta \leq 0.5$). The application of inelastic x-ray emission spectroscopy would give direct information on such spin-state transitions.

Bibliography

[1] M. Imada, A. Fujimori, Y. Tokura, Rev. Mod. Phys. **70**, 1039 (1998).

[2] H.Y. Hwang, T.T.M. Palstra, S-W. Cheong, and B. Batlogg, Phys. Rev. B **52**, 15046 (1995).

[3] Y. Moritomo, A. Asamitsu, and Y. Tokura, Phys. Rev. B **51**, 16491 (1995).

[4] C. Meneghini, D. Levy, S. Mobilio, M. Ortolani, M. Nunez-Reguero, A. Kumar, and D.D. Sarma, Phys. Rev. B **65**, 012111 (2002).

[5] T. Kawakami, S. Nasu, T. Sasaki, K. Kuzushita, S. Morimoto, S. Endo, T. Yamada, S. Kawasaki, and M. Takano, Phys. Rev. Lett. **88**, 037602 (2002).

[6] J.B. Torrance, P. Lacorre, A.I. Nazzal, E.J. Ansaldo and Ch. Niedermayer, Phys. Rev. B **45** 8209 (1992).

[7] J.L. García-Munoz, J. Rodriguez-Carvajal, P. Lacorre, and J.B. Torrance, Phys. Rev. B **46**, 4414 (1992).

[8] J.A. Alonso, M.J. Martínez-Lope, and M.T. Casais, J.L. García-Munoz, M.T. Fernández-Díaz and M. A. G. Aranda, Phys. Rev. B **64**, 094102 (2001).

[9] J.A. Alonso, J. L. García-Munoz, M.T. Fernández-Díaz, M.A. G. Aranda, M. J. Martínez-Lope, and M.T. Casais, Phys. Rev. Lett. **82**, 3871 (1999).

[10] J.-S. Zhou, J.B. Goodenough, and B. Dabrowski, Phys. Rev. Lett. **94**, 226602 (2005).

[11] C. Martin, A. Maignan, D. Pelloquin, N. Nguyen, and B. Raveau,Appl. Phys. Lett. **71**, 1421 (1997).

[12] S. Tsubouchi, T. Kyomen, M. Itoh, P. Ganguly, M. Oguni,. Y. Shimojo, Y. Morii and Y. Ishii, Phys. Rev. B **66**, 052418 (2002).

[13] S. Roy, M. Khan, Y.Q. Guo, J. Craig, and N. Ali, Phys. Rev. B **65**, 064437 (2002).

[14] M.A. Korotin, S. Yu. Ezhov, I.V. Solovyev, V.I. Anisimov, D.I. Khomskii, and G.A. Sawatzky, Phys. Rev. B **54**, 5309 (1996).

[15] T. Saitoh, T. Mizokawa, A. Fujimori, M. Abbate, Y. Takeda, and M. Takano, Phys. Rev. B **55**, 4257 (1997).

[16] C. Zobel, M. Kriener, D. Bruns, J. Baier, M. Grüninger, T. Lorenz, P. Reutler, and A. Revcolevschi, Phys. Rev. B **66**, 020402(R) (2002).

[17] M. Itoh, I. Natori, S. Kubota, and K. Motoya, J. Phys. Soc. Jpn. **63**, 1486 (1994).

[18] R. Caciuffo, D. Rinaldi, G. Barucca, J. Mira, J. Rivas, M.A. Senarís-Rodriguez, P.G. Radaelli, D. Fiorani, and J.B. Goodenough, Phys. Rev. B **59**, 1068 (1999).

[19] D. Louca, J.L. Sarrao, J.D. Thompson, H. Röder, and G.H. Kwei, Phys. Rev. B **60**, 10378 (1999).

[20] J. Wu, and C. Leighton, Phys. Rev. B **67**, 174408 (2003).

[21] M. Kriener, C. Zobel, A. Reichl, J. Baier, M. Cwik, K. Berggold, H. Kierspel, O. Zabara, A. Freimuth, and T. Lorenz, Phys. Rev. B **69**, 094417 (2004).

[22] D. Louca, and J.L. Sarrao, Phys. Rev. Lett. **91**, 155501 (2003).

[23] R.D. Shannon and C.T. Prewitt, Acta Crystallogr. B **25**, 725 (1969).

[24] M. Takano, S. Nasu, T. Abe, K. Yamamoto, S. Endo, Y. Takeda, and J. B. Goodenough, Phys. Rev. Lett. **67**, 3267 (1991).

[25] J.B. Goodenough, Magnetism and chemical bond, Interscience Publishers, New York (1963).

[26] H.A. Jahn and E. Teller, Proc. Roy. Soc. **A161**, 220 (1937).

[27] H. A. Jahn, Proc. Roy. Soc. **A164**, 117 (1938).

[28] M.D. Sturge, Phys. Rev. **140**, A880 (1965).

[29] J.H. van Vleck, J. Chem. Phys. **7**, 72 (1939).

[30] R. Gross and A. Marx, Lecturescript *Spinelektronik*, Walther-Meissner-Institut, Lehrstuhl für Technische Physik (E23), Walther-Meissner-Str.8, 85748 Garching (2004).

[31] M. Takano and Y. Takeda, Bull. Inst. Chem.Res. Kyoto Univ. **41**, 406 (1983).

[32] P.D. Battle, T.C. Gibb, and S. Nixon, J. Solid State Chem. **77**, 124 (1988).

[33] P.D. Battle, T.C. Gibb, and P. Lightfoot, J. Solid State Chem. **84**, 271 (1990).

[34] S.K. Park, S. Yamaguchi, and Y. Tokura, unpublished results (1998).

[35] D.I. Khomskii, *Electronic Structure, Exchange and Magnetism in Oxides*, LNP **569**, 89, in M.J. Thornton and M. Ziese (Eds.), Springer-Verlag, Berlin Heidelberg (2001).

[36] J. Hubbard, Proc. Roy. Soc **276**, 238 (1963).

[37] N.W. Ashcroft, N.D. Mermin, *Festkörperphysik*, Oldenbourg-Verlag, München (2001).

[38] H. Tasaki, J. Phys. Condens. Matter **10**, 4353 (1998).

[39] E. Müller-Hartmann, *19. IFF Ferienkurs: Supraleitung und verwandte Quantenphänomene*, Jülich 28.1 (1988).

[40] D.I. Khomskii and G. Sawatzky, Solid State Comm. **102**, 87 (1997).

[41] D.I. Khomskii, Lithuanian Journal of Physics **37**, 65 (1997).

[42] M.A. Korotin, V.I. Anisimov, D.I. Khomskii, and G.A. Sawatzky, Phys. Rev. Lett. **80**, 4305 (1997).

[43] J. Zaanen, G.A. Sawatzky, and J.W. Allen, Phys. Rev. Lett. **55**, 418 (1985).

[44] K.I. Kugel, D.I. Khomskii, Sov. Phys. Usp. **25(4)**, 231 (1982).

[45] C. Zener, Phys. Rev. **82**, 403 (1951).

[46] P.W. Bridgman, J. Appl. Phys. **65**, 461 (1941).

[47] W.A. Bassett, T. Takahashi and P.W. Stoock, Rev. Sci. Instrum. **38**, 37 (1967).

[48] L. Merrill und W.A. Bassett, Rev. Sci. Instrum. **45**, 290 (1974).

[49] G.J. Piermarini und S. Block, Rev. Sci. Instrum. **46**, 973 (1975).

[50] H.K. Mao, P.M.Bell, J.W. Shaner and D.J. Steinberg, J. Appl. Phys. **49**, 3276 (1978).

[51] G. Huber, K. Syassen und W.B. Holzapfel, Phys. Rev. B **15**, 5123 (1977).

[52] A. Jayaraman, Rev. Mod. Phys. **55**, 65 (1983).

[53] R. Lengsdorf, Diploma Thesis, University of Cologne (2003).

[54] P.M. Bell, J. Xu, and H.K. Mao, Proceedings of the Fourth Tropical Conference on Shock Waves in Condensed Matter, Plenum, New York (1986).

[55] M. Pasternak, University of Tel Aviv, Private communications (1996).

[56] H. Winkelmann, PhD Thesis, Universtiy of Cologne (1998).

[57] K. Drescher, PhD Thesis, University of Cologne (1997).

[58] M. Ait-Tahar, Diploma Thesis, University of Cologne (2001).

[59] B. Bireckoven and J. Wittig, J. Phys. E: Sci. Instrum., **21** 841 (1988).

[60] K. Ahilan and S.S. Saxena, University of Cambridge, (1999).

[61] W.B. Holzapfel, Z. Kristallogr. **216**, 473 (2001).

[62] F.D. Murnaghan, Am. J. Math. **59**, 235 (1937).

[63] F.D. Murnaghan, Proceedings of the National Academy of Sciences **30**, 244 (1944).

[64] K. Syassen, Ph.D. Thesis , University of Stuttgart (1974).

[65] F. Birch, Phys. Rev. **71**, 809 (1947).

[66] J. Staun Olsen, B. Buras, L. Geward and S. Steenstrup, J. Phys. E: Sci. Instrum. **14**, 1154 (1981).

[67] R. Boehler, N. von Bargen and A. Chopelas, Jour. Geophys. Res. B **95**, 21731 (1990).

[68] J.W. Otto, Hasylab Jahresbericht 1993 , 931 (1993).

[69] N. Seljakov and A. Krasnikow, Z. Phys. **33**, 601 (1925).

[70] N. Seljakov and A. Krasnikow, Nature **117**, 554 (1926).

[71] K. Hämäläinen, C.C. Kao, J.B. Hastings, D.P. Siddons, L.E. Berman, V. Stojanoff and S.P. Cramer Phys. Rev. B **46**, 14274 (1992).

[72] F.M.F. de Groot, A. Fontaine, C.C. Kao, and M. Krisch, J. Phys.: Condens. Matter **6**, 6875 (1994).

[73] J.Badro et al., Phys. Rev. Lett. **83** 4101 (1999).

[74] J.-P. Rueff et al., Unpublished results.

[75] K. Tsutsumi, H. Nakamori nd K. Ichikawa, Phys. Rev. B**13**, 929 (1976).

[76] B. Hermsmeier, C. S. Fadley, M.O. Krause, J. Jimenez-Mier, P. Gerard, and S. T. Manson, Phys. Rev. Lett. **61**, 2592 (1988).

[77] O. Leupold, J. Pollmann, E. Gerdau, H.D Rüter, G. Faigel, M. Tegze, G. Bartel, R. Rüffer, A.I. Chumakov and A.Q.R. Baron, Europhys. Lett. **35**, 671 (1996).

[78] W.G. Marshall, and D.J. Francis, J. Appl. Cryst. **35**, 122 (2002).

[79] M. Amboage, PhD Thesis, Universidad del País Vasco, (2003).

[80] Landolt-Börnstein, New Series, Group III, ed K.H. Hellwege and A.M. Hellwege, Berlin-Springer **4a**, ch 3, 126 (1970).

[81] V.M. Goldsmith, Skr. Nor. Vidensk. Akad. Mat. Naturvidensk. Kl. **2**, 1 (1926).

[82] A. Wold, B. Post and E. Banks, J. Am. Chem. Soc. **79**, 4911 (1957).

[83] S. Geller, J. Chem. Phys. **24**, 1236 (1956).

[84] P. Poix, C. R. Acad. Sci. Paris **270**, 1852 (1970).

[85] P. Lacorre, J.B. Torrance, J. Pannetier, A.I. Nazzal, P.W. Wang and T.C. Huang, J. Solid State Chem. **91**, 225 (1991).

[86] M. O'Keeffe, and B.G. Hyde, Acta Crystallogr. B **33**, 3802 (1977).

[87] M. Medarde, J. Mesot, P. Lacorre, S. Rosenkranz, P. Fischer and K. Gobrecht, Phys. Rev. B**52**, 9248 (1995).

[88] M. O'Keeffe, B.G. Hyde and Jan-Olov Bovin, Phys. Chem. Minerals **4**, 299 (1979).

[89] G. Demazeau, A. Marbeuf, M. Pouchard and P. Hagenmüller, J. Solid State Chem. **3** 582 (1971).

[90] M.L. Medarde, J. Phys. Condens. Matter **9**, 1679 (1997).

[91] J.L. García-Munoz, J. Rodriguez-Carvajal and P. Lacorre, Europhys. Lett. **20**, 241 (1992).

[92] U. Staub, G.I. Meijer, F. Fauth, R. Allenspach, J.G. Bednorz, J. Karpinski, S.M. Kazakov, L. Paolasini, and F. d'Acapito, Phys. Rev. Lett. **88**, 126402 (2002).

[93] T. Mizokawa, D. I. Khomskii, and G. A. Sawatzky, Phys. Rev. B **61**, 11263 (2000).

[94] J.B. Torrance, P. Lacorre, C. Asavaroengchai and R. Metzger, J. Solid State Chem. **90**, 168 (1991).

[95] M. Medarde, A. Fontaine, J.L. García-Munoz, J. Rodriguez-Carvajal, M. de Santis, M. Sacchi, G. Rossi, and P. Lacorre, Phys. Rev. B **46**, 14975 (1992).

[96] J. Garcia, J. Blasco and M.G. Proietti, Phys. Rev. B **52**, 15823 (1995).

[97] T. Mizokawa, A. Fujimori, T. Arima, Y. Tokura, N. Mori and J. Akimitsu, Phys. Rev. B **52**, 13865 (1995).

[98] H. Eisaki, S. Uchida, T. Mizokawa, H. Namatame, A. Fujimori, J. van Elp, P. Kuiper, G.A. Sawatzky, S. Hosoya and H. Katayama-Yoshida, Phys. Rev. B **45**, 12513 (1992).

[99] J.A. Alonso, M.J. Martínez-Lope, M.T. Casais, M.A.G. Aranda and M.T. Fernandez-Diaz, J. Am. Chem. Soc. **121**, 4754 (1999).

[100] J. Rodríguez-Carvajal, S. Rosenkranz, M. Medarde, P. Lacorre, M. T. Fernandez-Díaz, F. Fauth, and V. Trounov, Phys. Rev. B **57** 456 (1998).

[101] Fernando P. de la Cruz, Cínthia Piamonteze, Néstor E. Massa, Horacio Salva, José Antonio Alonso, María Jesús Martínez-Lope, and María Teresa Casais, Phys. Rev. B **66** 153104 (2002).

[102] M. Medarde, P. Lacorre, K. Conder, F. Fauth and A. Furrer, Phys. Rev. Lett. **80**, 2397 (1998).

[103] K.-H. Höck et al., Helv. Phys. Acta **56**, 237 (1983).

[104] J.A. Alonso, M.J. Martínez-Lope, M.T. Casais, J.L. García-Munoz and M.T. Fernández-Díaz, Phys. Rev. B **61**, 1756 (2000).

[105] C. Piamonteze, H.C.N. Tolentino, A.Y. Ramos, N.E. Massa, J.A. Alonso, M.J. Martínez-Lope, and M.T. Casais, Physica B, **320**, 71 (2002).

[106] C. Piamonteze, H.C.N. Tolentino, F.C. Vicentin, A. Ramos, N.E. Massa, J.A. Alonso, M.J. Martínez-Lope, and M.T. Casais, Surface Rev. Lett. **9**, 1121 (2002).

[107] N.E. Massa, F.P. de la Cruz, C. Piamonteze, H. Salva, J.A. Alonso, M.J. Martínez-Lope, and M.T. Casais, Bull. Am. Phys. Soc. **46**(1), 149 (2001).

[108] J.L. García-Munoz, M. Amboage, M. Hanfland, J.A. Alonso, M.J. Martínez-Lope, and R. Mortimer, Phys. Rev. B **69**, 094106 (2004).

[109] T. Mizokawa, and A. Fujimori, Phys. Rev. B **54**, 5368 (1996).

[110] T. Mizokawa, and A. Fujimori, Phys. Rev. B **51**, R12880 (1995).

[111] X. Obradors, L.M. Paulius, M. B. Maple, J.B. Torrance, A.I. Nazzal, J. Fontcuberta, and X. Granados, Phys. Rev. B **47**, 12353 (1993).

[112] P.C. Canfield, J.D. Thompson, S.W. Cheong, and L.W. Rupp, Phys. Rev. B **47**, 12357 (1993).

[113] M.Amboage, M. Hanfland, J.A. Alonso and M.J. Martínez-Lope, J. Phys.: Condens. Matter **17**, 783 (2005).

[114] X.Q. Xu, J.L. Peng, Z.Y.Li, H.L. Ju, and R.L. Greene, Phys. Rev. B **48**, 1112 (1993).

[115] S.W. Cheong, H.Y. Hwang, B. Batlogg, A.S. Cooper and P.C. Canfield, Physica B **194-196**, 1087 (1994).

[116] M. Amboage et al., unpublished results (2005).

[117] W.A. Harrision, The Electronic Structure and Properties of Solids Freeman, San Francisco (1980).

[118] Larsen and Von Dreele, "The Rietveld Method" Ed. R.A. Young, IUCr Momographs on Crstyallography, **5**, Oxford University Press (1993). (Reprinted 2002).

[119] M. Zaghrioui, A. Bulon, P. Lacorre, and P. Laffez, Phys. Rev. B **64**, 081102(R) (2001).

[120] J.-S. Zhou, J.B. Goodenough, and B. Dabrowski, Phys. Rev. B **67**, R020404 (2003).

[121] M. Mostovoy, Private communications (2005).

[122] G. Gilat and I. Nowik, Phys. Rev. **130**, 1361 (1963).

[123] W. Sturhahn, Hyperfine Interact. **125**, 149 (2000).

[124] G. Maris, Y. Ren, V. Volotchaev, C. Zobel, T. Lorenz, and T.T.M. Palstra, Phys. Rev. B **67**, 224423 (2003).

[125] G.H. Jonker, and J.H. Van Santen, Physica (Amsterdam) **19**, 120 (1953).

[126] V.G. Bhide and D.S. Rajoria, Phys. Rev. B **6**, 1021 (1972).

[127] K. Asai, O. Yokokura, and N. Nishimori, Phys. Rev. B **50**, 3025 (1994).

[128] S. Yamaguchi, Y. Okimoto, and Y. Tokura, Phys. Rev. B **54**, R11022 (1996).

[129] M.A. Senaris Rodriguez, and J.B. Goodenough, J. Solid State Chem. **116**, 224 (1995).

[130] R.H. Potze, G.A. Sawatzky, and M. Abbate, Phys. Rev. B **51**, 11501 (1995).

[131] K. Asai, Y. Yoneda, O. Yokokura, J.M. Tranquada, G. Shirane, and K. Kohn, J. Phys. Soc. Jpn. **67**, 290 (1998).

[132] S. Yamaguchi, Y. Okimoto, and Y. Tokura, Phys. Rev. B **55**, 8666 (1997).

[133] Y. Kobayashi, N. Fujiwara, S. Murata, K. Asai, and H. Yasuska, Phys. Rev. B **62**, 410 (2000).

[134] V.G. Sathe, A.V. Pimpale, V. Siruguri, and S.K. Paranjpe, J. Phys.: Condens. Matter **8**, 3889 (1996).

[135] F. Munakata, H. Takahashi, Y. Akimune, Y. Shichi, M. Tanimura, Y. Inoue, R. Itti, and Y. Koyama, Phys. Rev. B **56**, 979 (1997).

[136] A. Chainani, M. Mathew, and D.D. Sarma, Phys. Rev. B **46**, 9976 (1992).

[137] K. Tsutsui, J. Inoue, and S. Maekawa, Phys. Rev. B **59**, 4549 (1999).

[138] T. Vogt, J. A. Hriljac, N. C. Hyatt, and P. Woodward, Phys. Rev. B **67**, 140401(R) (2003).

[139] K. Asai, O. Yokokura, M. Suzuki, T. Naka, T. Matsumoto, H. Takahashi, N. Mori, and K. Kohn, J. Phys. Soc. Jpn. **66**, 967 (1997).

[140] J.-P. Rueff et al., Phys. Rev. B **63**, 132409 (2001).

[141] G. Vankó et al., in preparation (2005).

Erklärung

Ich versichere, daß ich die von mir vorgelegte Dissertation selbstständig angefertigt, die benutzten Quellen und Hilfsmittel vollständig angegeben und in den Stellen der Arbeit - einschließlich Tabellen, Karten und Abbildungen-, die anderen Werken im Wortlaut oder dem Sinn nach entnommen sind, in jedem Einzelfall als Entlehnung kenntlich gemacht habe; daß diese Dissertation noch keiner anderen Fakultät oder Universität zur Prüfung vorgelegen hat; daß sie - abgesehen von unten angegebenen Teilpublikationen - noch nicht veröffentlicht worden ist sowie, daß ich eine solche Veröffentlichung vor Abschluß des Promotionsverfahrens nicht vornehmen werde.

Die Bestimmungen dieser Promotionsordnung sind mir bekannt. Die von mir vorgelegte Dissertation ist von Herrn Professor Dr. M.M. Abd-Elmeguid betreut worden.

Köln, den 14. September 2005

Roman Lengsdorf

Teilpublikationen:

The observation of the insulator-metal transition in EuNiO₃ under high pressure
R. Lengsdorf, A. Barla, J.A. Alonso, M.J. Martinez-Lope, H. Micklitz and M.M. Abd-Elmeguid
J. Phys.: Condens. Matter **16**, 3355-3360 (2004).

Pressure-induced insulating state in (La,Sr)CoO₃
R. Lengsdorf, M. Ait-Tahar, S.S. Saxena, M. Ellerby, D.I. Khomskii, H. Micklitz, T. Lorenz, and M.M. Abd-Elmeguid
Phys. Rev. B **69**, 140403(R) (2004).

Kurzzusammenfassung

Das Ziel dieser Arbeit war es, den Einfluß äußeren Druckes auf die elektronischen, magnetischen und strukturellen Eigenschaften einiger ausgewählter Übergangsmetalloxid-Verbindungen ($RNiO_3$ und $(La,Sr)CoO_3$) zu untersuchen. Hauptaugenmerk galt hierbei dem Einfluß der Ladungsordnung, Spin-Zustandsänderung, magnetischen Ordnung und Struktur auf den elektrischen Transport und insbesondere den Mechanismus des Metall-Isolator (MI)-Übergangs zu untersuchen. Zu diesem Zweck wurden an diesen Verbindungen elektrische Widerstandsmessungen, Röntgen-Diffraktometrie, kernresonante Streuung an ^{151}Eu, Magnetisierungsmessungen, Neutronen-Diffraktometrie und K β Röntgenemissionsmessungen durchgeführt.

Der Schwerpunkt dieser Arbeit lag in der Untersuchung der $RNiO_3$ (R = Sm, Eu, Y und Lu) Serie, in welcher der temperatur-induzierte MI-Übergang (bei einer Temperatur T_{MI}) verknüpft ist mit einem strukturellen Phasenübergang (orthorhombisch-monoklin) und gleichzeitig auftretender Ladungsordnung der Ni^{3+} Ionen. Darüberhinaus zeigen alle Verbindungen unterhalb T_{MI} antiferromagnetische Ordnung.
Es zeigte sich bei den untersuchten Systemen ein druckinduzierter Isolator-Metall (IM) Übergang (5 – 7 GPa), der nicht mit einem strukturellen Phasenübergang verknüpft ist. Das Rätsel, daß ein metallischer Zustand in einer monoklinen Struktur auftritt, in der Ladungsordnung existiert, wurde mittels hochauflösender Neutronen-Diffraktometrie an $LuNiO_3$ gelöst: Die Analyse der (Ni-O) Bindungslänge der zwei NiO_6 Oktaeder ($Ni1O_6$ und $Ni2O_6$) zeigt, daß sich die Bindungslängen beider Oktaeder entlang der c-Achse unter Druck angleichen, was zu einem partiellen Schmelzen der Ladungsordnung führt und den IM-Übergang bewirkt.

Der zweite Teil dieser Arbeit beschäftigt sich mit Hochdruckuntersuchungen der Verbindungsreihe $La_{1-x}Sr_xCoO_3$, die den Freiheitsgrad der Spin-Zustandsänderung von Co^{3+} Ionen hat. Im Grundzustand liegt das undodierte System im Low-Spin (LS, $S = 0$) Zustand vor. Bei Dotierung mit Sr^{2+} Ionen (x $\geq$ 0.2) wird angenommen, daß das Einsetzen der metallischen Leitfähigkeit und ferromagnetischen Kopplung durch den Doppelaustausch zwischen Co^{4+} (LS) und Co^{3+} Intermediate-Spin (IS, $S = 1$) Ionen hervorgerufen wird.
Bei der Hochdruckuntersuchung an einem metallischen, ferromagnetischen Einkristall $La_{0.82}Sr_{0.18}CoO_3$, wurde ein Übergang von einem leitenden in einen isolierenden Zustand sowie eine Reduzierung der magnetischen Ordnungstemperatur T_C mit zunehmenden Druck festgestellt, wobei die Kristallstruktur unverändert bleibt. Die Ergebnisse stehen im Gegensatz zu Beobachtungen an verwandten Übergangsmetalloxiden. Die Beobachtung des druckinduzierten isolierenden Zustands wird durch eine graduelle Änderung des Co^{3+} Spin-Zustands von einem magnetischen IS- zu einem unmagnetischen LS-Zustand erklärt. Den mikroskopischen Beweis für einen druckinduzierten Spinübergang liefert die druckabhängige Untersuchung mittels Co K β Röntgenemission-Spektroskopie.

Abstract

The effect of external pressure on the electronic, magnetic and structural properties of two novel types of transition metal oxides ($RNiO_3$ and $(La,Sr)CoO_3$) that allows one to investigate the influence of charge ordering, spin-state transition, magnetic ordering and structure on the electrical transport and in particular the mechanism of the metal insulator (MI) transition. The applied experimental methods were electrical resistance, x-ray diffraction, ^{151}Eu nuclear resonance scattering, magnetization, neutron diffraction and K β x-ray emission spectroscopy.

The major part of this thesis was devoted to the high pressure investigation of the $RNiO_3$ series (R = Sm, Eu, Y and Lu), in which the temperature-induced MI transition (at a temperature T_{MI}) is connected with an orthorhombic-monoclinic structural phase transition and simultaneous charge ordering of the Ni^{3+} ions. At temperatures lower than T_{MI}, all these compounds undergo antiferromagnetic ordering. In all investigated compounds we find a pressure-induced insulator metal (IM) transition for $5.4 \leq p \leq 6.2$ GPa, which is in contrast to the temperature-induced MI transition, is not connected with a structural phase transition. The puzzle of the observation of the pressure-induced metallic state in a monoclinic symmetry, where a charge ordered state exists has been unraveled by performing high resolution neutron diffraction measurements on $LuNiO_3$ under high pressure. The analysis of the (Ni-O) bond length of the two Ni-sites (Ni1 and Ni2) in $LuNiO_3$ reveals that the bond lengths along the c-axis become nearly equal at 6 GPa which leads to a partial melting of the charge ordering that triggers the IM transition.

The second part of this thesis describes the high pressure study on $La_{1-x}Sr_xCoO_3$ in which the Co^{3+} ions exhibit the possibility to change their spin-state. The ground state of the undoped insulating system is the low-spin (LS, $S = 0$) configuration. For doped samples (x $\geq$ 0.2) the conductivity and ferromagnetic coupling are suggested to be related to the double exchange of LS Co^{4+} and intermediate-spin (IS, $S = 1$) Co^{3+} states. We have investigated the effect of pressure on the electronic, magnetic and structural properties on a single crystal sample of conducting, ferromagnetic $La_{0.82}Sr_{0.18}CoO_3$. Contrary to the results reported on related systems, we find a transition from the conducting to an insulating state and a reduction of the magnetic ordering temperature T_C with increasing pressure while the lattice structure remains unchanged. The investigation of the effect of pressure on the Co magnetic moment both by magnetization measurements and Co K β x-ray emission spectroscopy prove that the pressure-induced metal insulator transition is driven by a gradual change of the spin-state of Co^{3+} ions from magnetic IS to nonmagnetic LS state.

Lebenslauf

Persönliche Daten:

Name, Vorname	Lengsdorf, Roman Georg
Geburtsdatum	24.05.1972
Geburtsort	Leverkusen
Nationalität	deutsch

Studium:

Januar 2003	Beginn der Promotion am Lehrstuhl für Angewandte Physik, Universität zu Köln
Januar 2003	Diplom in Physik
März 2002 - Januar 2003	Diplomarbeit am Lehrstuhl für Angewandte Physik, Universität zu Köln; Thema: "Untersuchungen der elektrischen, magnetischen und strukturellen Eigenschaften von $La_{1-x}Sr_xCoO_3$ unter hohem Druck"
Juli 1999	Vordiplom in Physik
Oktober 1992	Beginn des Studiums der Physik an der Universität zu Köln

Schulbildung:

$1987 - 1992$	Städt. Gymnasium Genovevastr., Köln, Abschluß mit allgemeiner Hochschulreife
$1983 - 1987$	Städt. Realschule Görresstr., Leverkusen
$1982 - 1983$	Städt. Hauptschule, Dhünnberg, Leverkusen
$1978 - 1982$	Kath. Grundschule, Dhünnberg, Leverkusen

Weitere Aktivitäten:

2004	Konferenzsekretär des II. internationalen Symposiums "Physics of Solids Under High Pressure Using Nuclear Probes (HPNP'04)", 20-24 July, Köln
seit 01.2003	wissenschaftlicher Mitarbeiter am II. Physikalischen Institut der Universität zu Köln
03.2002 - 12.2002	studentische Hilfskraft am II. Physikalischen Institut der Universität zu Köln
01.1999 - 12.2002	studentische Hilfskraft, Heilpädagogische Fakultät der Universität zu Köln
08.1999 - 05.2000	IT-Systemadministrator am ISO-Institut, Köln-Nippes
1993 - 1998	Werkstudent bei der AGFA-Gevaert AG, Leverkusen, (jeweils in den Semesterferien)
1992	zweimonatiges Betriebspraktikum bei der Bayer AG, Leverkusen

Acknowledgment / Danksagung